Atom gradiometry for future Gravitational Wave Detectors

Xinhao Zou

THÈSE PRÉSENTÉE

POUR OBTENIR LE GRADE DE

DOCTEUR
DE L'UNIVERSITÉ DE BORDEAUX

ECOLE DOCTORALE SCIENCES PHYSIQUES ET DE L'INGÉNIEUR

LASERS, MATIÈRE ET NANOSCIENCES

Par **Xin-Hao ZOU**

Gradiométrie atomique pour les futurs détecteurs d'ondes gravitationnelles

Sous la direction de : **Philippe BOUYER**
Co-directeur : **Benjamin CANUEL**

May **20,** 2022

Membres du jury :

M. Mingsheng ZHAN	Wuhan Institute of Physics and Mathematics	Rapporteur
M. Patrick CHEINET	Laboratoire Aimé Cotton	Rapporteur
M. Eric CORMIER	Université de Bordeaux	Président
M. Stéphane GAFFET	Laboratoire Souterrain Bas Bruit	Examinateur
Mme Bess FANG	Laboratoire Systèmes de Référence Temps-Espace	Examinateur
M. Alexandre GAUGUET	Laboratoire Collisions Agrégats Réactivité	Examinateur
M. Philippe BOUYER	Laboratoire Photonique, Numérique et Nanosciences	Directeur
M. Benjamin CANUEL	Laboratoire Photonique, Numérique et Nanosciences	Co-directeur

Titre : Gradiométrie atomique pour les futurs détecteurs d'ondes gravitationnelles

Rssumé : Les ondes gravitationnelles nous permettent d'élargir notre connaissance de l'univers en transportant sur de très grandes distances les informations reliées aux variations de masses. La détection de ces ondes est de première importante non seulement pour la physique fondamentale mais également pour les aspects technologiques des mesures de haute précision. Différents observatoires d'ondes gravitationnelles sont en opération ou en construction à travers le monde, avec des bandes de détection allant de 10^{-9} Hz to 10^{4} Hz. L'expérience MIGA (Matter Wave Interferometer Gravitational Antenna) a pour but de construire un réseau de gradiomètres atomiques en cavité sur une longueur de base de 150 m au laboratoire Souterrain Bas Bruit (LSBB). En comparaison avec les détecteurs optiques de type Michelson en cavité, les gradiomètre atomiques ouvrent la voie vers une détection en dessous du Hz, et peuvent permettre une détection dans une gamme de fréquence 0.1 Hz - 10 Hz complémentaire par rapport aux instruments existants ou en construction. Dans ce cadre, le LP2N réalise une expérience de démonstration consistant en un gradiomètre atomique en cavité basé sur deux sources d'atomes froids de Rb. Nous discutons dans cette thèse les progrès réalisés sur cette expérience. En particulier, la réalisation et le commissioning du système à vide ainsi que la caractérisation complète d'une des sources atomiques. Dans ce manuscrit, nous rapportons également les travaux théoriques réalisés dans un second volet de cette thèse et consistant à l'étude du couplage optimal entre un interféromètre atomique et une cavité optique pour la détection des ondes gravitationnelles. Nous présentons ainsi une géométrie originale de détection permettant d'obtenir une amplification du signal d'onde gravitationnel détecté par un interféromètre atomique.

Mots clés :
vague gravitationnelle
gradiométrie atomique
cavité optique

UMR 5298 – Institut d'Optique d'Aquitaine. Université de Bordeaux. Rue François Mitterrand - 33400 TALENCE.
&
Laboratoire Photonique, Numérique et Nanosciences (LP2N)

Title : Atom gradiometry for future Gravitational Wave Detectors

Abstract : Gravitational waves expand our observation scope of the universe, carrying information through time and space undisturbed due to their inability to be scattered or absorbed. The detection of gravitational waves is of great significance to the progress of fundamental physics research and associated experimental technology. Gravitational-wave observatories are in operation or under construction worldwide, with detection frequencies ranging from 10^{-9} Hz to 10^{4} Hz. The Matter Wave Interferometer Gravitational Antenna (MIGA) experiment aims to build an atomic gradiometer consisting of one 150 m long optical cavities on the LSBB platform based on the increasingly mature atomic interference technology. Compared with optical interferometers, atom gradiometers can reduce noise in the low-frequency range, filling a gap in gravitational wave detection in the band 0.1 Hz - 10 Hz. At LP2N, as a demonstration experiment for gravitational wave antennas, an atom interferometer based on quasi-Bragg scattering and marginally-stable cavity has been built. We are currently building a 6.35 m atom gradiometer composed of two atom sources and made the first attempt to observe an interference signal. We discuss the implementation of this atom gradiometer, focusing on our achieved vacuum of $1.4 \times 10^{-}9$ mbar in an large vacuum chamber as well as the completed tuning of the first atomic source. This thesis elucidates the difference between an atom gradiometer and an optical interferometer for gravitational wave detection. We propose a nested three-cavity system through two orthogonal optical cavities - a structure that can improve the strain sensitivity of atom interferometry, allowing it to exceed the standard quantum limit of optical gravitational wave detectors.

Keywords :
gravitational wave
atom gradiometry
optical cavity

UMR 5298 – Institut d'Optique d'Aquitaine. Université de Bordeaux. Rue François Mitterrand - 33400 TALENCE.
&
Laboratoire Photonique, Numérique et Nanosciences (LP2N)

Acknowledgements

The work of this thesis is done in LP2N based on the MIGA project. CSC Scholar funds my Ph.D. project.

Special acknowledgment is given to my thesis jury. Thanks to Mingsheng Zhan and Patric Cheinet for reading and revising my thesis; thanks to Alexandre Gauguet, Bess Fang, Eric Cormier, and Stéphane Gaffet for taking their precious time to review my work.

The profound gratitude should go to my mentor, Philippe Bouyer, for leading me into the MIGA project. As a warm and friendly boss, he did his best to help us and give critical guidance on the scientific problem.

I feel so grateful to my co-director, Benjamin Canuel, for his guidance in all aspects, especially taught me to be rigorous in science. I admire him for his deep understanding of experiments and theory and his commitment and hard work as an outstanding project leader.

I would like to express my endless gratitude to Dylan O.Sabulsky, whose optimistic passion and combativeness have deeply infected me. As the person I work with the most time, he gave me countless help in experiments and daily life and corrected all my writing details in the papers and this thesis. I hope he can guide more people as a mentor in the future.

Thanks to Joseph Junca for helping me solve many problems in the experimental test and speeding up the construction of the atom gradiometer. In the MIGA team, our four people from three countries had a lot of interesting exchanges on science, politics, and food. Congratulations on his successful doctoral defense, and I wish him all the best in the United States.

Thanks to Andrea Bertoldi and Marco Prevedelli for their help with the control software. Thanks to Quentin Beaufils from the SYRTE for building the atom head and providing us with information about it that made my experiments run smoothly.

I truly appreciate my colleagues: Chenhao, Hodei, Devang, Paul, and Louisa from the BIARO team; the AUFRONS team with Simon, Vincent, Romain, Jean-Baptiste, Guillaume, and Adèle; the iXAtom team with Vincent and Quentin; Romain and Célia from ICE team. You guys are always willing to share ideas and address the shortage of our experimental equipment and make me feel the rapport in the lab.

I am genuinely grateful to the institute's technical and administrative departments, without whose help our research would not have been possible. Thanks to Arnaud, Jean-Hugues for solving problems with electronic circuits, Philippe for helping us make mechanical parts, and Jacky Robin, Fabien Lehoux, Stéphanie, and all other members of LP2N

I want to express my heartfelt thanks to my parents for their support over the years. An old Chinese saying, "While his parents are alive, the son may not go abroad to a distance. If he does go abroad, he must have a good reason." It was your encouragement that helped me accomplish all this.

My love and thanks to my gril friend Simei, I was so lucky to meet her. She gave me emotional support and accompanied me through it all, making me a better me.

Thanks to my friends in Bordeaux, Jialun Zhou, Xiaojun, and Jielin Chen, we made a happy fitness team. As well as Jing Yu, Mengjia Wang, and Xiangzhuo Liu, your company has made my life more colorful.

I am grateful to my buddy Armam in China as my guarantor, Hepeng YAO in Switzerland, and Zekai Chen in the United States. Thank you for sharing the ups and downs of work and life with me. Hope to see you soon.

Thanks to the Chinese Government for funding my Ph.D., I'm so excited about returning to my country.

Contents

List of Figures

Introduction

Background

Gravitational waves (GWs), the ripples in the curvature of time and space caused by the dynamics of stellar objects with a mass greater than 0, radiate outward from the source in the form of space-time waves. These waves transmit energy in the form of gravitational radiation.

In 1916, Albert Einstein predicted the existence of GW based on general relativity [1]. In his theory, Einstein connects space-time with the matter directly. Space-time affects the movement of matter, and matter, in turn, determines the distribution of space-time. The "curvature" of this distribution is the source of gravity, and the gravitational "ripples" produced by an object moving at a variable speed are called gravitational waves.

The observation of GWs is verification of Einstein's general theory of relativity. However, since the propagation of GWs does not require a medium and its coupling with matter is extremely weak, they are not absorbed or scattered, which allows us to learn about the early universe by observing the gravitational waves generated from very distant places.

Nowadays, various GW detectors are in operation or being built, such as the Advanced Laser Interferometer Gravitational-Wave Observatory (aLIGO), which has been in operation since September 2015. In addition, other projects are proposed or in preparation, such as ET, eLISA, AEDGE, and TianQin, whose detection range covers different GW frequency bands.

On February 11, 2016, the LIGO Scientific Cooperation Organization and the Virgo team announced that they had used advanced LIGO detectors to detect gravitational wave signals from the merger of two black holes for the first time [2].

Motivation

Gravitational waves opened a new window for observing the universe. Outside this window, different GWs frequency bands correspond to different "views" of the universe, which require different detection technologies. Currently, there are several detectors in the pipeline with different detection frequencies from LIGO/Virgo (10 Hz-10 kHz), and the MIGA is one of them.

The MIGA project aims to build a large-scale laser-based atom interferometer gravitational wave antenna. This project is a beautiful combination of cosmology and particle physics, the two ends of the "Ouroboros" in physics. It uses the differential signal of multiple atom interferometers (AI) in the same optical cavity to study the realization of a new method to detect GW signals in a frequency window ranging from one hundred millihertz to one hertz[3], which is not covered by any detection device currently in operation.

Before the official launch of MIGA Rustrel, there are two pre-projects in the Laboratoire Photonique, Numérique et Nanosciences (LP2N). The first is an experiment consisting of one atom head and a vacuum chamber about 1 meter long. In this project, some cavity tests can be done to improve the contrast of the interference signal of AI.

The second one comprises two atomic sources and a 6.35-meter-long vacuum chamber. Here we gain experience with large vacuum physics and initially observe differential signals between two AI.

When the first two projects started running in a laboratory environment, the third step, the Rustrel project, is to complete the 150 m gradiometer at LSBB, a tunnel at a depth up to 500 m below a karstic massif. The temperature and humidity underground are also a great challenge for this project.

The main work of this thesis is to complete the construction of the atom gradiometer at LP2N and accumulate experience for MIGA at Rustrel.

Thesis organization

The structure of this thesis is as follows:

Chapter 1 introduces the history of the interferometer and cold atom development, some basic knowledge of gravitational waves and the MIGA project.

In **Chapter 2**, we analyze how to convert the target signal into an observable optical signal. First, the difference between atom interferometers and optical interferometers is discussed. After, we study how the optical resonant cavity affects the signal-to-noise ratio of these two detection methods. Finally, an experimental configuration that enhances the sensitivity of the atom interferometer through the optical resonant cavity is proposed.

Chapter 3 describes the construction journey of the atom gradiometer at LP2N, including the laser system, the vacuum generation, optical system, control systems, and atom head. All of which are examples of subsystems for the Rustrel project.

Chapter 4 gives the preliminary results of the atom source test.

We conclude with **Chapter 5**, for the prospects of the MIGA project, discuss how to improve the accuracy of large-scale atom gradiometers further, and imagine more application directions.

Chapter 1

MIGA project

According to Issac Newton, "If I have seen further, it is by standing on the shoulders of giants." [4]Whether or not the original meaning of this sentence is ironic, it at least shows one thing: any scientific progress benefits from its previous technology. The realization of the MIGA project is also inseparable from the development of various theories and technologies, including the theoretical understanding of GW, the improvement of atom interferometers used to detect gravitational waves[5], and the corresponding atom cooling technology. In this chapter, we will talk about the history of these technologies and the planning of the MIGA project.

Contents

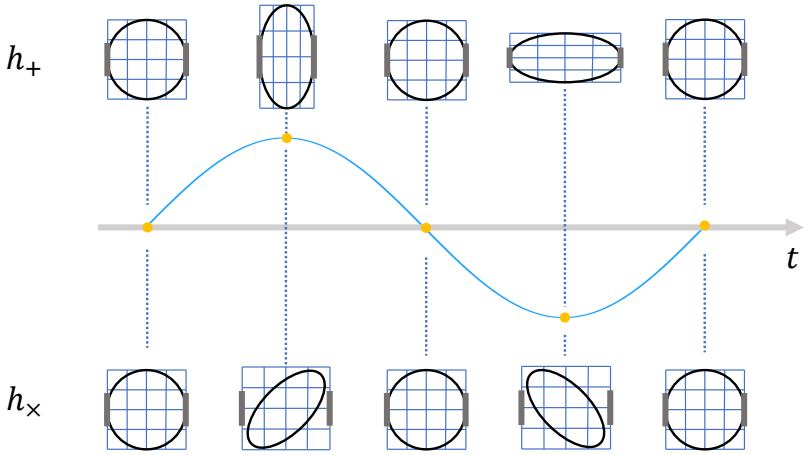

Figure 1.1: The Lorentz gauge and the TT gauge jointly determine that the gravitational wave tensor is only independent in two directions, which are denoted as h_+ and $h_\times$

1.1 Gravitational Wave

In 1916, Einstein published his famous paper about General Relativity, and in that paper, the gravitational field equation is established [1, 6]:

$$R_{\mu\nu} - \frac{1}{2}g_{\mu\nu}R = \frac{8\pi G}{c^4}T_{\mu\nu} \tag{1.1}$$

where $T_{\mu\nu}$ is the energy momentum tensor of matter, describing the energy and mass distribution of the gravitational field source; $R_{\mu\nu}$ is the Ricci curvature tensor, R is scalar curvature and $g_{\mu\nu}$ represent the space-time metric tensor and the unknown of the gravitational field equation. The left side of the gravitational field equation is Einstein's gravitational tensor, which describes the curved space-time structure; on the right is the energy tensor, which describes the distribution of matter.

Einstein's equation associate the curvature of space-time and the energy-momentum tensor of matter. It shows that the existence of matter induces space-time to curve. In general relativity, the distance between two 4-dimensional points $ds = (g_{\mu\nu}dx^\mu dx^\nu)^{\frac{1}{2}}$ is an important scalar, $ds^2 > 0$ is called the Space-like interval, $ds^2 < 0$ is called the Time-like interval, for light, $ds^2 = 0$, therefore $ds^2 = 0$ is called the light-like interval.

Under the weak field approximation, the space-time metric tensor $g_{\mu\nu}$ can be written as the Minkowski metric $\eta_{\mu\nu}$ plus a small perturbation term $h_{\mu\nu}$,

$$g_{\mu\nu} = \eta_{\mu\nu} + h_{\mu\nu} \quad \text{with} \quad \left|\frac{h_{\mu\nu}}{\eta_{\mu\nu}}\right| \ll 1, \tag{1.2}$$

within the Lorenz gauge condition and the TT gauge. Taking the propagation direction of the gravitational wave as z, the four-dimensional Einstein wave equation is transformed into the three-dimensional wave equation

$$\left(\nabla^2 - \frac{1}{c^2}\frac{\partial}{\partial t^2}\right) h_{\mu\nu} = 0, \tag{1.3}$$

where a solution of this equation is:

$$h_{\mu\nu} = \begin{pmatrix} 0 & 0 & 0 & 0 \\ 0 & h_+ & h_\times & 0 \\ 0 & h_\times & -h_+ & 0 \\ 0 & 0 & 0 & 0 \end{pmatrix} e^{-i\omega(t-\frac{z}{c})}. \tag{1.4}$$

These two gauges limit the variation of h such that it can only be composed of two components $h_\times$ and h_+, as shown in 1.1.

For light, $ds^2 = 0$, we have [7]

$$c^2dt^2 - dx^2 - dy^2 - dz^2 + 2h_\times dxdy + h_+(dx^2 - dy^2) = 0, \tag{1.5}$$

and we assume a light path along x direction,

$$c^2dt^2 - dx^2 + h_+dx^2 = 0. \tag{1.6}$$

Expand h_+ to first order:

$$dx = \pm c\,dt\left(1 + \frac{h_+(t)}{2}\right) \tag{1.7}$$

This formula is the influence of gravitational waves on light propagation. Therefore, by measuring the change of light propagation, we can measure gravitational waves. Generally speaking, only the accelerated motion of supermassive objects can generate GW signal that are strong enough to be detected by existing technology. Therefore, current gravitational wave observation is mainly aimed at the motion of celestial bodies, like the GW150914 binary black hole system detected by LIGO [9] and Virgo [10]. As shown in Fig. 1.2(a), two celestial bodies orbit each other, and as the system loses energy, the orbiting speed increases, they gradually approach and become a single object. The second derivative of the mass quadrupole moment is very large. Therefore, gravitational waves radiate with high power. A binary system that is several kilometers away from each other will lose all of their potential energy within minutes or even seconds. As time increases, the amplitude and frequency of

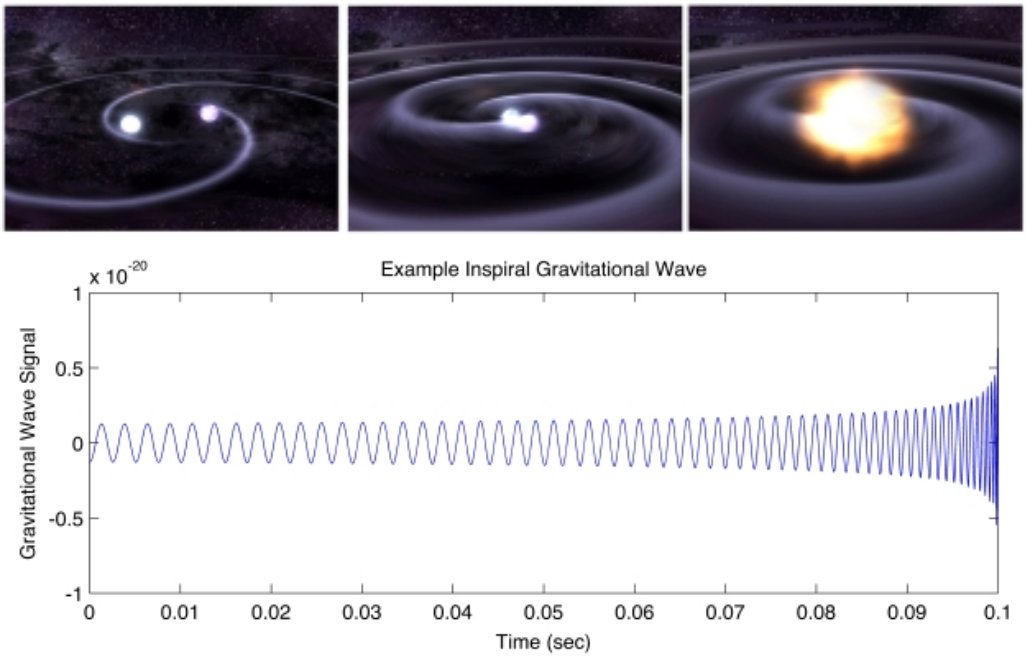

Figure 1.2: (a) A simulation diagram of two celestial bodies orbiting each other and progressing (from left to right) to merger with resulting gravitational waves.(b) An example signal from an inspiral gravitational wave source [8], GW signal's amplitude and frequency increases as two celestial bodies approach each other and orbit speed increases

gravitational waves will increase until the two celestial bodies are close enough to merge (Fig.1.2(b)).

1.2 Interference

When two waves of the same frequency are superimposed, the amplitude increases when the phase is the same, and decreases when the phase is opposite. According to this property, Thomas Young verified the wave nature of light through the double-slit experiments.

Many physical quantities can change the phase of the wave. Through the phenomenon of interference, we can observe the changes of phase to measure these physical quantities, which is the principle of the interferometer. After Albert A. Michelson developed the first interferometer in 1880, many interferometers have been developed and are widely used as precision measurement tools. After the invention of the laser, the accuracy of optical interferometers has been greatly improved, occupying the dominant position of interferometry.

The interferomety is also applied to the measurement of gravitational waves. The Michelson interferometer with an optical resonator used by LIGO/Virgo has successfully detected the GW signal; meanwhile, the atom interferometer, as another measuring tool, also demonstrated its potential with the development of cold atom technology. In the following chapters, We'll detail how gravitational waves are measured by these two interferometers.

1.3 Laser Cooling and Cold Atoms

In 1873, Maxwell concluded that "the electromagnetic field has radiation pressure" from his famous formula. This conclusion was confirmed by the experiment of Russian scientist Pyotr Nikolaevich Lebedev in 1900 [11], but this light pressure effect was too weak to be applied in practice; that was the case until 1960, when Theodore Harold Maiman built the first laser based on the theoretical work of Charles Hard Townes and Arthur Leonard Schawlow [12]. Humankind obtained the first monochromatic high-brightness light source and the feasibility of using light to manipulate and cool down the atoms.

Only 25 years later in 1985, Steven Chu's group [13] used six beams of mutually perpendicular light to irradiate sodium atom vapor to obtain "optical molasses" with a temperature as low as $240\ \mu$k. In 1995, JILA's Carl Edwin Wieman and Eric Allin Cornell [14], and MIT's Wolfgang Ketterle [15] respectively realized Bose-Einstein condensation (BEC), winning the 2001 Nobel Prize in Physics.

Cold atoms are now a powerful technique for scientific research on atoms and molecules but also provide a platform for precision measurement. In 1924, the De Broglie formula made people realize that matter has wave-particle duality, and objects with greater momentum have smaller wavelengths. Therefore, when we use atoms as detection tools, the precision that can be obtained is much higher than that of light waves. However, the motion of atoms, or from a macro perspective, the temperature, is accompanied by the Doppler effect. This effect causes a widening of the frequency and dramatically reduces the accuracy of the measurement. A atomic cooling technology is precisely the antidote to this problem.

1.4 The MIGA project

At present, LIGO and Virgo have successfully detected gravitational waves; there are also other gravitational wave detection projects (Fig.1.3) under construction or proposed.

Among them, KAGRA [16], INDIGO [17], ET [18], cosmic explorer [19] are all trying to obtain higher sensitivity in a frequency range similar to that of LIGO/Virgo, the corresponding astronomical phenomenon is compact binary inspirals(white dwarfs, neutron stars, and black holes); Both eLISA [20], TianQin [21] and Taiji [22] are space projects, aiming at low frequencies of less than 0.1 Hz. Gravitational wave signals in this range are mainly generated by massive binaries and extreme mass ratio inspirals. The plan of AEDGE [23], and DECIGO [24] consist in filling the gap between 0.1 Hz-10 Hz. Gravitational waves in this frequency range can begenerated by Type IA supernovae, two intermediate-mass black holes system, etc.

The MIGA project aims to explore a new field, namely large-scale atomic interferometry, which will bring groundbreaking applications to the detection of gravity and basic research. Using a new method that utilizes a set of atom interferometers simultaneously manipulated

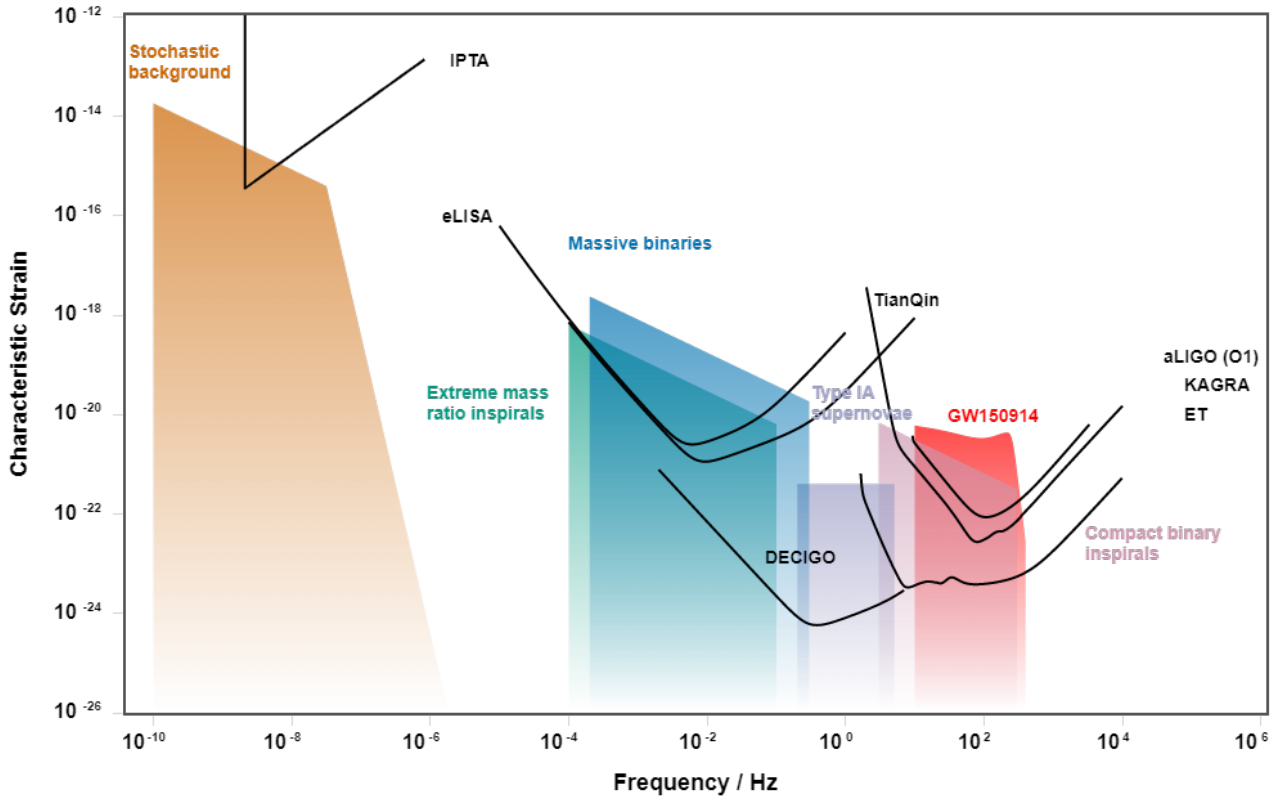

Figure 1.3: Gravitational wave detectors in operation or planned, along with warious astronomical phenomena corresponding to different frequency ranges[25, 26].

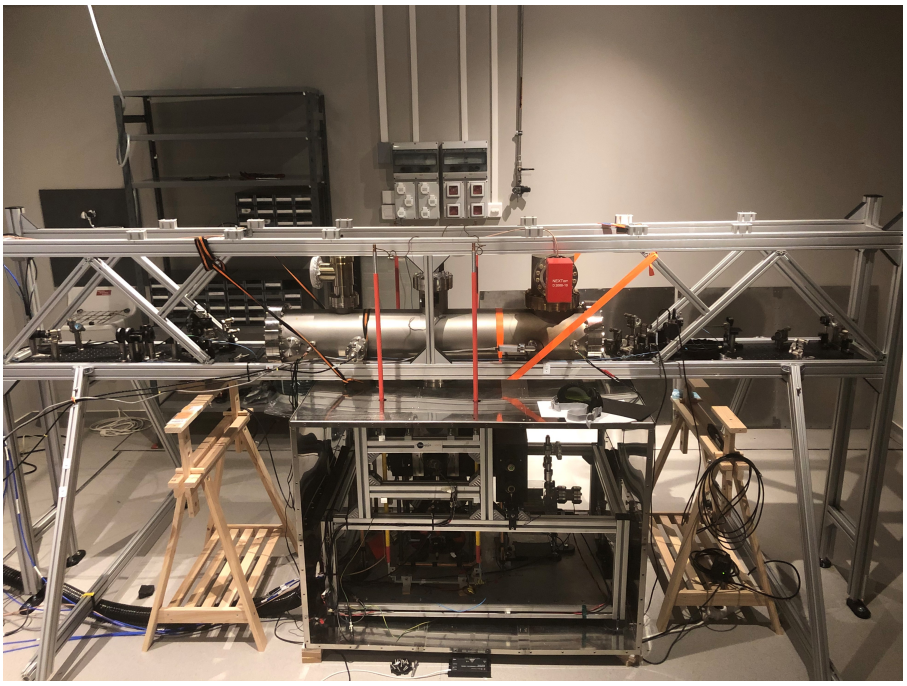

Figure 1.4: A photo of accelerometer with one atom source and a one-meter cavity

by the resonant light field of a 150 m cavity, MIGA will allow a better understanding of the evolution of gravitational fields and new tools for gravitational wave detection.

On the basis of MIGA, we propose the establishment of the European Laboratory for Gravitational and Atomic Interference Research (ELGAR) [27], an underground infrastructure based on the latest advances in atomic physics for the study of space-time and gravity, with the main goal of detecting GW. ELGAR will measure GW in the infrasonic band with peak strain sensitivity of $3.3 \times 1022/\sqrt{\text{Hz}}$ at 1.7 Hz. It will be used in various fields of fundamental and applied research beyond GW astronomy, including gravity, general relativity, and geology.

1.4.1 Stages of preparation

For the project to proceed reasonably and orderly, MIGA applied a three-step strategy. First, build an atom accelerometer, which consists of one atom interferometer and an optical resonator about 1 meter long, and based on this, tests can be perfomed to improve the contrast of the interference signal of AI, as well as studying the influence of different modes of the resonant cavity on an atom interferometer [28].

The second stage is to build an atom gradiometer composed of two atom sources and a

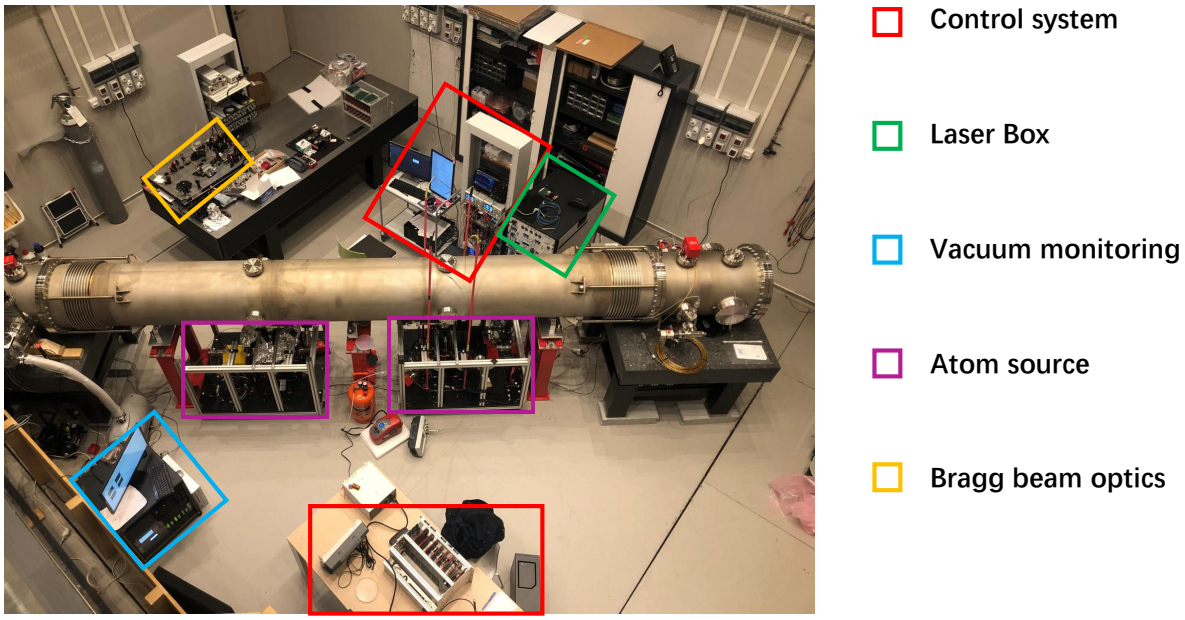

Figure 1.5: A top view of the atom gradiometer experiment

6.35-meter-long vacuum chamber. In this project we test how to obtain a vacuum of 10^{-10} mbar in a relatively large chamber, study the synchronization of signals between different atom interferometers, and initially observe the gradiometeric signal.

While the first two steps were carried out in the laboratory as preparation projects, we also started construction [29] of the 150-meter-long atom gradiometer (see Fig. 1.7) on the LSBB experiment platform [30]. The LSBB platform is a dismissed military facility located 500 m underground, this effectively isolates environmental noise, but this kind of humid underground environment also presents new and different challenges to atomic physics.

1.4.2 Design

The working principle of MIGA [3] is utilize two ultra-long resonant cavities and place multiple $\pi - \frac{\pi}{2} - \pi$ pulsed atom interferometers in this cavity along the direction of the laser. The output of the atom interferometer depends on the phase difference accumulated by the light fields in the two directions. This phase difference depends on the laser frequency, strain changes caused by gravitational waves, inertial effect, and the position of the mirrors that

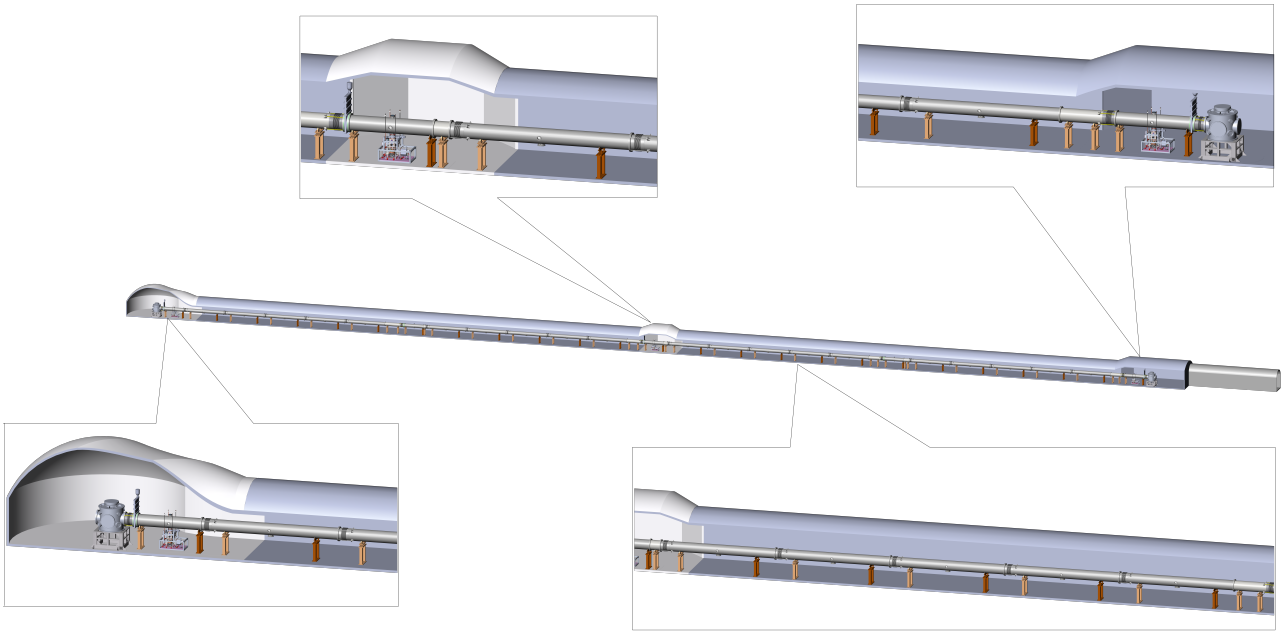

Figure 1.6: Schematic diagram of the MIGA Ruetrel experiment setup. Enlarged in the bubble is the location where we installed the atom head, control equipment, and vacuum equipment.

form the resonant cavity. In the next chapter, all these factors are explained and calculated in detail.

In short, MIGA is a hybrid atom-laser interferometer that uses an array of atom sensors to simultaneously measure inertial effects and strain variation inside the optical cavity. In the case of preliminary completion, we will use a vacuum chambers with length of 150 m. When the pulse interval is set to $T = 250$ ms, the corresponding measurement sensitivity has a peak value of $2.2 \times 10^{-13}/\sqrt{\text{Hz}}$ at $\Omega_{\text{GW}} = \frac{1}{2(T+t_r)} = 2$ Hz, this sensitivity allows us to study local gravitational field fluctuations [31]. Higher sensitivity can be obtained by upgrading the instrument's performance, like applying large-momentum transfer atom optics (LMT), and other technologies.

1.4.3 Location

MIGA is installed at the low-noise underground laboratory of Rustrel - Pays d'Apt (LSBB)(see Fig.1.7(a) for MIGA position), a research laboratory founded in 1997 at Rustrel in Vaucluse. It reuses the old decommissioned underground facilities of the land component

of the Albion Plateau Nuclear Strike Force, taking advantage of an exceptional environment in terms of noise, sheltered from any electromagnetic exposure [32]. Furthermore, LSBB has characteristics similar to oil and water reservoirs found in the Middle East as a carbonate platform. The site is above the Fontaine de Vaucluse aquifer and can be accessed from the surface or underground. The length of the site is about 3.7 km, and the area is about 14,000 m^2. Considering the topography of the surface, the thickness of the rock cover varies from 30 m to 519 m.

As an underground scientific platform, it takes advantage of an exceptional environment in terms of seismic noise [31], sheltered from any electromagnetic exposure, as a result of the distance of the site from heavy industrial and human activities. All this makes it an ideal on-site research facility for next-generation GW detectors.

At present, there are more than 30 European and international research teams conducting interdisciplinary research collaborations at LSBB. Research topics include but are not limited to, environmental deformation at different time and space scales, reflection of nanostructures, and analysis of changes in magnetic fields facing seismic frequencies.

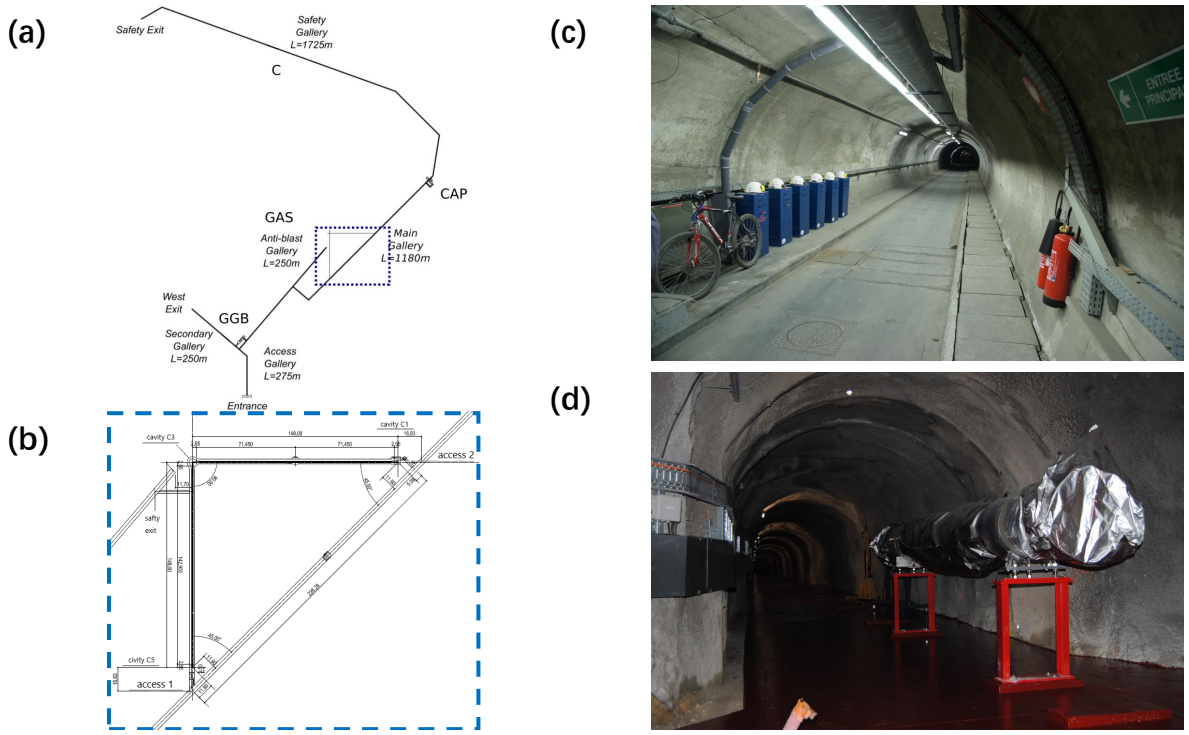

Figure 1.7: (a) The map of the LSBB underground facility. The installation location of MIGA is highlighted with a blue dotted rectangle. (B) MIGA galleries, two perpendicular tunnels of about 150 meters are connected to the main tunnel through access 1 and access 2, and there is also a safety exit. The main laser equipment and control equipment are placed in the cavity C1, C3 and C5. (C) The first vacuum tube installed in MIGA tunnel [29].

Chapter 2

Atom interferometry enhanced by optical resonant cavity

To talk about GW observation, one must bow to the inevitable in that one need discuss the virtues of LIGO/Virgo. This chapter will discuss the difference between MIGA and LIGO/Virgo from a principle point-of-view, explain why atom gradiomety has higher sensitivity in the low-frequency range, and propose a method to further improve this sensitivity

An interferometer is a general type of technology, and its idea is to use the interference of waves to obtain its phase information. It is widely used in many fields that require precise measurement.

Considering the need to observe interference fringes to obtain information, early interferometers used light waves as interference sources. Later, with people's understanding of matter waves, atomic interferometers were gradually experimented and applied. This section will introduce these two types of interferometry and compare their differences in GW measurement.

Contents

2.1 Optical Interferomety

People's understanding of interference originates from light, and the phenomenon of light interference can be seen everywhere in life, such as the color of the oil slick on soup [33]. Compared with most waves in our daily lives, the wavelength of light is very short, and a small phase difference can bring about noticeable interference fringe changes, which is one of the reasons why optical interference is chosen as a precision measurement tool. With the continuous development of technology, especially the invention of the laser, hundreds of

optical interferometers have been developed for different measurement purposes, and the accuracy of these interferometers have also been greatly improved.

The design of the interferometer used by LIGO/Virgo comes from the earliest interferometer - the Michelson interferometer, the principle of which is to detect the phase difference of two perpendicular optical paths caused by GW. [34, 35, 36, 37]. To better understand the difference between atom interferometers and optical interferometers, let us first introduce the principle of the Michelson interferometer.

2.1.1 Transfer function of Michelson Interferometer

From 1881 to 1884, Albert Michelson and Edward Morley conducted the famous Michelson-Morley experiment to measure the relative velocities of the earth and the ether. Although neither experimenter admitted it, this experiment objectively verified that ether does not exist [38, 39, 40]. Since then, this ingenious experimental design has been widely applied in precision measurement.

The structure of the Michelson interferometer is shown in the Fig. 2.1. Before the beam splitter, the light field is E_0; then the light is split and passes through two perpendicular light paths; the two reflected light fields are respectively:

$$E_1 = E_0(S + \delta S_1)e^{i\theta_1}\, e^{-i\omega t - 2ikL_1} \quad \text{and}$$

$$E_2 = E_0(S + \delta S_2)e^{i\theta_2}\, e^{-i\omega t - 2ikL_2}$$

where S represents the carrier amplitude, δS and θ are the amplitude and phase change caused by the signal (in our case, a GW), and L_n are the optical paths of two arms. The resulting transmitted field of the splitter is the sum of these two fields:

$$E_{trans} = E_0 e^{-i\omega t - 2ikL_1}\left((S + \delta S_1)e^{i\theta_1} + (S + \delta S_2)e^{i\theta_2 - 2ik\Delta L}\right), \tag{2.1}$$

with $\Delta L = L_2 - L_1$. The detected power is

$$\begin{aligned} P_{trans} &= |E_{trans}|^2 \\ &= 2|E_0|^2\Big[S(S + \delta S_1 + \delta S_2)\big(1 + \cos(\Delta\theta + 2k\Delta L)\big)\Big] \\ &= 2|E_0|^2\big(S^2(1 + \cos 2k\Delta L) + S(\delta S_1 + \delta S_2)(1 + \cos 2k\Delta L) - S^2\Delta\theta \sin 2k\Delta L\big), \end{aligned} \tag{2.2}$$

here $\Delta\theta = \theta_1 - \theta_2$, and in the equation only the first order of ΔS and θ is kept, considering

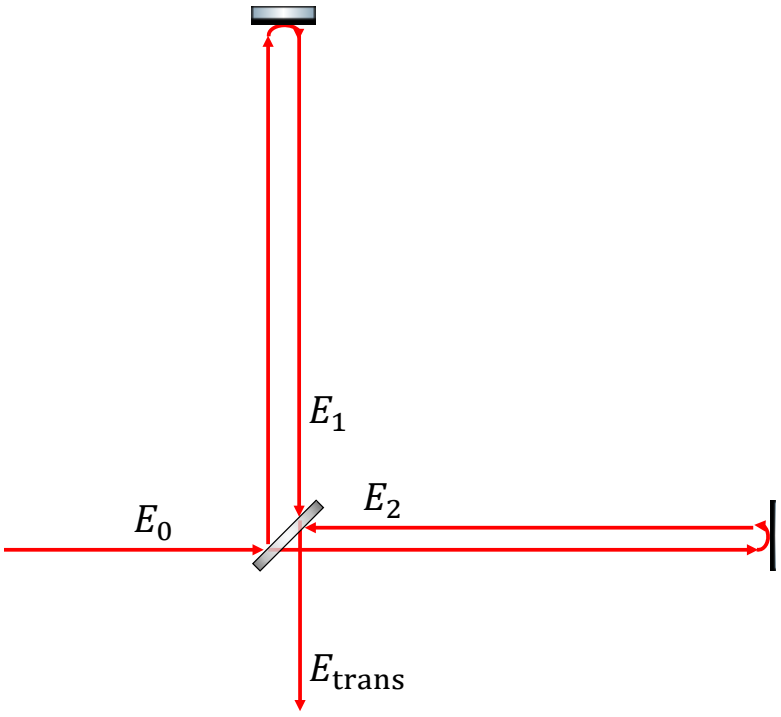

Figure 2.1: Schematic diagram of a Michelson interferometer. The interferometer's arms can be free space or optical resonators, which does not change the operating principle.

that the amplitude and phase changes caused by the signal are quite small. In this result, the DC component is $2|E_0|^2S^2\big(1+\cos 2k\Delta L\big)$, and the signal part is

$$2|E_0|^2\big(S(\delta S_1+\delta S_2)(1+\cos 2k\Delta L)\big)-S^2\Delta\theta\sin 2k\Delta L\big). \tag{2.3}$$

2.1.2 Standard Quantum Limit

The detection sensitivity of optical interferometers has a fundamental limitation - the standard quantum limit (SQL), which is composed of quantum shot noise (QSN) and quantum radiation pressure noise (QRPN). Both of these two noises are related to light intensity.

Quantum shot noise in optical detection is related to photon counting statistics, the discrete nature of electrons, and the inherent noise generation in electronics [41, 42]. The quantum mechanical uncertainty principle sets a lower limit for measurements. When detecting with an optical interferometer, this noise is mainly affected by statistical fluctuations in the number of photons. According to the quantum statistical picture, assuming that the number of photons detected per unit time is N, the fluctuation is proportional to $\sqrt{N}$.

Therefore the signal to shot noise ratio of the Michelson interferometer is proportional to

$$\text{SNR}\propto|E_0|\frac{(\delta S_1+\delta S_2)(1+\cos 2k\Delta L)-S\Delta\theta\sin 2k\Delta L}{\cos(k\Delta L)} \tag{2.4}$$

When $k\Delta L=2n\pi+\frac{\pi}{2}$, there is no DC component, and SNR $\propto 2S\Delta\theta$, which is the dark fringe.

Quantum radiation pressure noise is the noise caused by the laser's radiation pressure on the test mass [43]; although our light intensity is stabilized via closed feedback, due to the same quantum fluctuations as shot noise, the radiation force felt by the test mass will still vary with time. The fluctuation of radiation force is

$$F_{QRPN}=\frac{2\delta P}{c}, \tag{2.5}$$

where δP are the power fluctuations of P_{inside} impinging upon the test mass. P_{inside} and the input light intensity P_0 are not necessarily equal. For the convenience of discussion, we choose a Michelson interferometer without optical cavity, and detect the reflected light field at the dark fringe, then we have $P_{inside}=P_0$,

$$F_{QRPN}=\frac{2\delta P}{c}=\frac{2}{c}\sqrt{P_0\hbar\omega}. \tag{2.6}$$

The phase noise generated by this force is

$$\delta\theta_{QRPN}(\Omega) = \frac{2\sqrt{P_0\hbar\omega}}{cM\Omega^2\lambda}, \tag{2.7}$$

where M is the test mass and λ is the light wavelength. The strain sensitivity refers to the change in measurement value caused by noise or signal, where the combined strain sensitivity of the two kinds of noise here is:

$$S_h = S^h_{shot} + S^h_{QRPN}, \tag{2.8}$$

where $S^h_{shot} = \frac{4\hbar c^2}{\omega L^2 P_0 \hbar}$ according to Eq. 2.4, and $S^h_{QRPN} = \frac{4P_0\hbar\omega}{L^2c^2M^2\Omega^4}$, here we define $\mathbf{K} = \frac{P_0\omega}{c^2\Omega^2 M}$ and $h_{sql} = \sqrt{\frac{8\hbar}{M\Omega^2L^2}}$, and substitute into Eq. 2.8

$$S_h = \left(\mathbf{K} + \frac{1}{\mathbf{K}}\right)\frac{h^2_{sql}}{2}. \tag{2.9}$$

When $\mathbf{K} = 1/\mathbf{K}$, S_h reaches the minimum value h^2_{sql}, this value is called the standard quantum limit. So far, we have calculated the case of a Michelson interferometer without a cavity.. In the presence of a resonant cavity, the SQL will be the same, while[44, 45]

$$\mathbf{K} = \frac{2I_0\,\gamma^2}{I_{SQL}\Omega^2\left(1+\frac{\Omega^2}{\gamma^2}\right)} \tag{2.10}$$

where $\gamma = \frac{Tc}{4FL}$ is the half bandwidth of the cavity, and $I_{SQL} = \frac{mL^2\gamma^4}{4\omega_0}$ is the required intensity to reach the standard quantum limit.

2.2 Atom interferomety

An atom interferometer is an interferometer that utilizes the properties of atomic waves. Coherent atomic waves pass through different paths and interfere, and one can obtain information of atoms by observing the interference pattern [46]. In addition, compared to photons, atomic waves have shorter wavelengths and, therefore, higher theoretical precision.

Experiments of atom interference can be traced back to 1930 when Estermann and stern [47] obtained diffraction patterns from LiF crystals reflecting helium atoms. In 1991, O. Carnal and J. Mlynek [48] used the metastable helium atom to carry out the atom Young's double-slit experiment, which is the first interference pattern formed by atomic waves traveling through two different paths. Since then, more different types of atomic interferome-

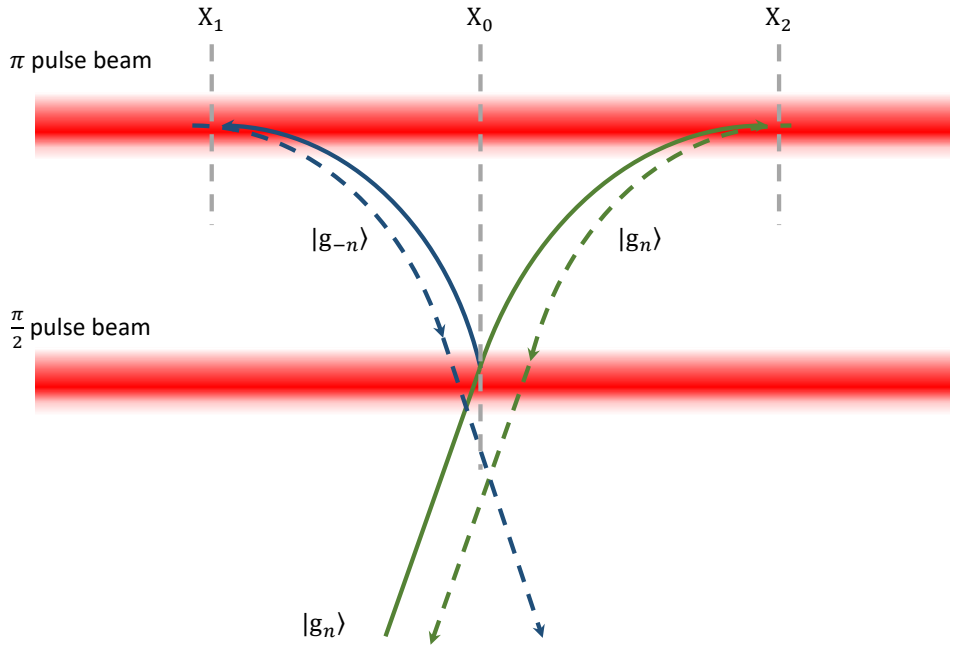

Figure 2.2: The process in which an atom undergoes $\frac{\pi}{2} - \pi - \frac{\pi}{2}$ pulses to produce interference of different momentum states. Different colors represent different momentum states, the solid line represents the ascending route, and the dashed line represents the falling route

ters have been developed[49], among which, we use a matter-wave analog of the 3-grating Mach-Zehnder interferometer in our experiment to measure the phase change of the light field. First, the atoms are thrown upwards pass through an optical lattice formed by standing wave light, with $\pi/2$ and π Bragg scattering pulse (Fig. 2.2) act as the splitter and reverse of the atomic wave; then the atoms pass through the $\pi/2$ Bragg pulse mixing again. The output of such an interferometer is a measurement of atomic population in different momentum states.

Next, we analyze in detail how to measure the phase change of the light field during this process.

2.2.1 The interaction between atoms and light

To explain the principle of the our light-pulse atom interferometer, let us start with a two-state atom interacting with a standing wave formed by light [50]; the Hamiltonian can be described as

$$H = \frac{p^2}{2M} + \hbar\omega_e|e\rangle\langle e| + \hbar\omega_g|g\rangle\langle g| + \hat{V} \tag{2.11}$$

where p is the momentum of the atom, M is the mass of the atom, ω_e and ω_g are the energy difference between the two energy states to the intermediate state, respectively,

$$\hat{V} = -\vec{d}\cdot\left(\vec{E_1}e^{i(k\hat{z}-\omega t+\theta_1)} + \vec{E_2}e^{i(-k\hat{z}+\omega t+\theta_2)}\right) \tag{2.12}$$

is the potential energy of the standing wave field, $|\vec{E_2}| \approx |\vec{E_1}|$ are the field strengths of the light fields in the two directions that form the standing wave, $\vec{d}$ is the atomic dipole moment and $\omega + \delta_0 = \omega_e - \omega_g$, where δ_0 is the detuning between the frequency of the light field ω and the two energy level differences $\omega_e - \omega_g$.

We assume that the atom is initially in its ground state $|g\rangle$, and the detuning δ is large enough that the upper state $|e\rangle$ can be adiabatically eliminated. The atom's state vector can be written as: $|\Psi\rangle = e(z,t)|e\rangle + g(z,t)|g\rangle$. Substituting Eq. 2.12 and state vector into the Schrödinger equation $i\hbar\frac{\partial\Psi}{\partial t} = \hat{H}\Psi$, we lead ourselves to:

$$i\hbar\dot{g}(z,t) = \frac{\hbar^2}{2M}\frac{\partial^2 g(z,t)}{\partial z^2} + \frac{\hbar\Omega_{\text{Rabi}}^2}{2\delta_0}\left(e^{i(2kz+\theta_1-\theta_2)} + e^{i(-2kz-\theta_1+\theta_2)}\right)g(z,t), \tag{2.13}$$

M is the mass of the atom and the Rabi frequency

$$\Omega_{\text{Rabi}} = \frac{1}{\hbar}\langle e|\vec{d}\cdot\vec{E}|g\rangle. \tag{2.14}$$

Fourier expand $g(z,t)$ based on the vector kz:

$$g(z,t) = \sum_n g_n(t)e^{inkz} \quad \text{and} \tag{2.15}$$

$$i\hbar\sum_n \dot{g}_n e^{inkz} = \hbar\sum_n\left[(n^2\omega_r + \Omega_{\text{two}})g_n + \frac{\Omega_{\text{two}}}{2}(g_{n+2}e^{i(\theta_1-\theta_2)} + g_{n-2}e^{i(\theta_2-\theta_1)})\right]e^{inkz} \tag{2.16}$$

where $\Omega_{\text{two}} = \frac{\Omega_{\text{Rabi}}^2}{2\delta}$ is two-photon Rabi frequency, g_n is the parameter of momentum states$|g, n\hbar k\rangle$, this can only hold if for all n

$$i\hbar\dot{g}_n = \hbar n^2\omega_r g_n + \Omega_{\text{two}}(g_n + \frac{1}{2}g_{n+2}e^{-i\Delta\theta} + \frac{1}{2}g_{n-2}e^{i\Delta\theta}), \tag{2.17}$$

with $\Delta\theta = \theta_2 - \theta_1$ is the phase difference of light in the two directions forming the standing

wave field, and $\omega_r = \frac{\hbar k^2}{2M}$ is recoil frequency.

2.2.2 Raman-Nath and Bragg Regime

For Eq.2.17, different action times and light intensities will result in different momentum state distributions. Long-interaction and different light intensities correspond to the Bragg regime and channeling regime, and the short-interaction time correspond to Raman-Nath regime [51, 52]. The initial study of these two different scattering figures came from the scattering of light by the acousto-optic modulation crystal. The Raman-Nath diffraction condition is that the incident light is approximately perpendicular to the phonon direction, the interaction time between the two is relatively short, and the phonon frequency is relatively low. The diffraction pattern contains many diffraction orders of the symmetrically distributed light intensity given by Bessel functions. When Light interacts with phonons long enough, the light incident at a certain angle will only be scattered in the first order. The other diffracted orders are compressed.

The optical grating has the similar principle for the scattering of atoms, as shown in Fig. 2.3. The width of grating is determined by the interaction time t_{int} between the atoms and the optical lattice [53]. The expression potential energy is given in Eq. 2.12, which can be simplified to

$$V = V_{\text{max}} \cos^2(kz), \tag{2.18}$$

here V_{max} is called the "lattice depth" of the optical lattice, according to Eq. 2.14, $V_{\text{max}} = \frac{\hbar\Omega_0^2}{\delta}$, in order to facilitate the following discussion, we write both V_{max} and t_{int} in dimensionless form:

$$q = \frac{V_{\text{max}}}{4\hbar\,\omega_r} \quad \text{and} \quad \tau_{int} = \omega_r t_{int}. \tag{2.19}$$

2.2.2.1 Raman-Nath Regime

When the interaction time between atoms and light is short enough to satisfy the Raman-Nath approximation $\tau_{int} < \frac{1}{2\sqrt{2q}}$, the term ω_r in Eq. 2.17 can be ignored, assuming that all the initial atoms are distributed in the g_0 state, the distributions of different momentum states

after scattering will be

$$g_{2m} = (-i)^m J_m(2q\ \tau_{int}) \tag{2.20}$$

After scattering, the atoms are mainly distributed in the g_0 state, since $|J_m(2q\ \tau_{int})|^2 = |J_{-m}(2q\ \tau_{int})|^2$, the population of the diffraction orders is symmetric with respect to the g_0.

2.2.2.2 Bragg Regime

When $q < 1$,$\tau_{int} > \frac{1}{2\sqrt{2q}}$, the scattering satisfies the Bragg condition, the atoms will distributed in $\vec{p}_{in}$ and $\vec{p}_{in} - 2\vec{p}_k$ momentum states after scattering [54]. Assuming that the initial state atoms are all at $p_{in} = n\hbar k$. Due to the conservation of energy, except for $\pm n\hbar k$, the atomic numbers of other states are essentially unchanged, $\dot{g_k} \approx 0(k \neq \pm n)$. Hence $g_k \approx 0(k \neq \pm n)$,

$$i\dot{g}_n = \frac{1}{2}\Omega_{\text{eff}} e^{-in\Delta\theta} g_{-n} \tag{2.21}$$

$$i\dot{g}_{-n} = \frac{1}{2}\Omega_{\text{eff}} e^{in\Delta\theta} g_n \tag{2.22}$$

A rough estimate of the effective Rabi frequency for nth diffraction is given by the first nonzero term of the perturbation expansion [55]

$$\Omega_{\text{eff}} \approx \frac{\Omega_{\text{two}}^n}{(8\omega_r)^{n-1}} \frac{1}{[(n-1)!]^2}. \tag{2.23}$$

As $\frac{\Omega}{\omega_r}$ increases, this approximation is no longer accurate, and the distribution of atoms on higher-order momentum states cannot be ignored. We use Ω_R to denote a time-invariant Ω_{eff} so the transfer matrix [56] from the initial state $g_{-n}(t_0), g_n(t_0)$ to $g_{-n}(t), g_n(t)$ is

$$M(t,t_0) = \begin{pmatrix} e^{-i\omega(t-t_0)}\cos(\Omega_R(t-t_0)) & -ie^{-i\omega(t-t_0)}e^{in\Delta\theta}\sin(\Omega_R(t-t_0)) \\ -ie^{-i\omega(t-t_0)}e^{-in\Delta\theta}\sin(\Omega_R(t-t_0)) & e^{-i\omega(t-t_0)}\cos(\Omega_R(t-t_0)) \end{pmatrix}, \tag{2.24}$$

here we define a light pulse with $t - t_0 = \frac{\pi}{2\Omega_R}$ as $\frac{\pi}{2}$ pulse, and $t - t_0 = \frac{\pi}{\Omega_R}$ as π pulse. The light-pulse atom interferometer consists of a $\frac{\pi}{2} - \pi - \frac{\pi}{2}$ pulse sequence.

In actual experiments, the infinite 3D-lattice conditions of Bragg scattering cannot be satisfied. The regime is in the transition range between Raman-Nath (short-interaction), Bragg (weak potential) and channeling (strong potential), and there will be distribution of

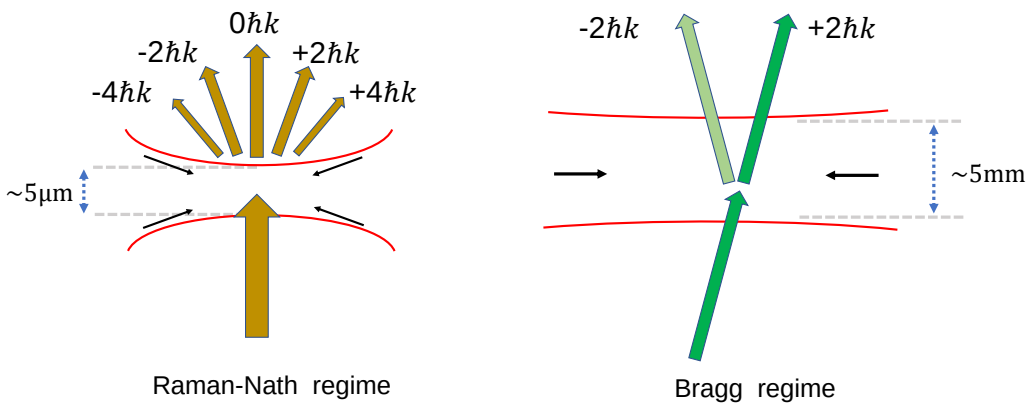

Figure 2.3: Kapitza-Dirac scattering versus Bragg scattering[57],The beam waist of Kapitza-Dirac scattering is smaller, thus allowing energy conservation of more momentum states.Bragg scattering requires a larger waist for light with photons that are highly collimated, in this case, There are only two scattering states that satisfy the conservation of energy and momentum.

atoms in other momentum states, which is called quasi-Bragg diffraction [55].

2.2.3 Transfer function of atom interferometer

Now that we have a theoretical foundation of how atoms and light interact, we can discuss the principles of atomic interferometers.

Atom interferometers are designed differently depending on the physical quantity being measured, but the principle is the same - measuring the phase change during the process through the interaction between light and atoms. The structure of the interferometer used in our experiment is shown in Fig. 2.2. Two laser beams are reflected to form two standing wave optical lattices, the cooled atoms are thrown up and then fall, during which three Bragg scatterings are generated with two light pulses; here, we call it a $\frac{\pi}{2} - \pi - \frac{\pi}{2}$ process according to the duration of the pulse and the Rabi frequency. In addition to the light's own phase, it will pick up a measurable phase $\Delta\theta(t)$ from a passing gravitational wave characterized by $h(t) = h\cos(\Omega_{\text{GW}}t + \Theta_{\text{GW}})$, here Ω_{GW} is the frequency of gravitational waves, and Θ_{GW} is the phase of gravitational waves. This optical phase can be imprinted onto the atomic wave function, implying an atomic phase $\Delta\Phi_{AT}$ measurable via atom interferometry.

In the previous section, the transfer matrix of the interaction between the atom and the light field was obtained, then we can get the transfer matrix of $\frac{\pi}{2}$ pulse, π pulse and a free evolution[58] respectively:

$$M(\tau_R,\phi)=\begin{pmatrix} 0 & e^{-i\omega\tau_R+\phi} \\ e^{-i\omega\tau_R+\phi} & 0 \end{pmatrix} \tag{2.25}$$

$$M(2\tau_R,\phi)=\frac{1}{\sqrt{2}}\begin{pmatrix} e^{-i\omega\tau_R} & e^{-i\omega\tau_R+\phi} \\ e^{-i\omega\tau_R+\phi} & e^{-i\omega\tau_R} \end{pmatrix} \tag{2.26}$$

$$M^{'}(\Delta t)=\begin{pmatrix} e^{-i\omega\Delta t} & 0 \\ 0 & e^{-i\omega\Delta t} \end{pmatrix} \tag{2.27}$$

where $\tau_R=\frac{\pi}{2}/\Omega_R$ is the duration of the $\frac{\pi}{2}$ pulse. ϕ is the phase of light field, which remains constant within a pulse.

Assuming that all atoms are initially prepared at $|g,+n\hbar k\rangle$, we obtain the matrix equation of a $\frac{\pi}{2}-\pi-\frac{\pi}{2}$ pulse process [58]:

$$\begin{pmatrix} g_{-n}(t_0+2T+4\tau_R) \\ g_n(t_0+2T+4\tau_R) \end{pmatrix}=M(\tau_R,\phi_1)M^{'}(T)M(2\tau_R,\phi_2)M^{'}(T)M(\tau_R,\phi_3)\begin{pmatrix} 0 \\ 1 \end{pmatrix}. \tag{2.28}$$

The resulting transition possibility to state $|g,-n\hbar k\rangle$ is

$$g_{-n}=\frac{1}{2}(e^{-i\Delta\Phi_{AT}}+1). \tag{2.29}$$

Note that the atomic wave function is split at position X_0 at the first diffraction, then interact with second optical lattice at X_1,X_2 respectively and go back to X_0, the final phase of atoms is [50]:

$$\Delta\Phi_{AT}=\phi_1(X_0)-\phi_2(X_1)-\phi_2(X_2)+\phi_3(X_0), \tag{2.30}$$

Considering $X_0=(X_1+X_2)/2$ and assuming that the phase ϕ changes linearly with position, we have

$$\Delta\Phi_{AT}=\phi_1-2\phi_2+\phi_3. \tag{2.31}$$

According to Eq. 2.30, the transfer function from $\Delta\theta$ to $\Delta\Phi_{AT}$ is defined as [56]

$$g(t)=\lim_{\Delta\theta\to 0}\frac{\Delta\Phi_{AT}}{\Delta\theta}. \tag{2.32}$$

For the sake of conciseness, we set $t_0=-T-2\tau_R$. To obtain the relationship between

$\Delta\Phi_{AT}$ and $\Delta\theta$, we only need to make a small change to the matrix in Eq.2.28, here we assume that the phase change $\Delta\theta$ occurs within the π pulses at t_θ, then the original matrix $M(\tau_R,\phi_1)M^{'}(T)M(2\tau_R,\phi_2)M^{'}(T)M(\tau_R,\phi_3)$ becomes:

$$M(\tau_R,\phi_1)\,M^{'}(T)\,M(\tau_R+t_\theta,\phi_2)\,M(\tau_R-t_\theta,\phi_2+\Delta\theta)\,M^{'}(T)\,M(\tau_R,\phi_3+\Delta\theta) \tag{2.33}$$

Then the change of $\Delta\Phi_{AT}$ can be obtained, so that $g(t)$ becomes:

$$g(t)=\begin{cases}\sin(\Omega_R t), & 0<t<\tau_R\\ 1, & \tau_R<t<T+\tau_R\\ -\sin(\Omega_R(T-t)). & T+\tau_R<t<T+2\tau_R\end{cases} \tag{2.34}$$

Assuming the phase change of the light field $\Delta\theta=\frac{h}{2}|\beta|\cos(\Omega_{\mathrm{GW}}t+\Theta_{\mathrm{GW}})$ with β the conversion parameter from GW to light field phase. The corresponding atomic phase is:

$$\begin{aligned}\Delta\Phi&=\int_{-\infty}^{+\infty}g(t)d\Delta\theta=\int_{-\infty}^{+\infty}g(t)\frac{d\Delta\theta}{dt}dt\\&=\frac{h|\beta|}{2}\int_{-\infty}^{+\infty}g(t)\sin(\Omega_{\mathrm{GW}}t+\Theta_{\mathrm{GW}})dt\\&=\frac{h\Omega|\beta|}{2}\cos(\Theta_{\mathrm{GW}})\int_{-\infty}^{+\infty}g(t)\sin(\Omega_{\mathrm{GW}}t)dt\\&=\frac{h|\beta|}{2}\cos(\Theta_{\mathrm{GW}})\Omega\mathrm{Im}(G(\Omega))\end{aligned} \tag{2.35}$$

where $G(\Omega)$ is the Fourier transform of $g(t)$. Therefore the transfer function is given by

$$H(\Omega)=\Omega G(\Omega). \tag{2.36}$$

This atom phase is then converted into the population of the atom by interference

$$\begin{aligned}P_A&=\frac{N}{2}\left(1-\Delta\Phi_{\mathrm{AT}}\right)\\&=\frac{N}{2}\left(1-\frac{h|\beta|}{2}\cos(\Theta_{\mathrm{GW}})\mathrm{Im}(H(\Omega))\right),\end{aligned} \tag{2.37}$$

where N represents the total number of atoms in the interference process. Averaging over a random distribution of the GW phase Θ_h, the rms value of signal is

$$P_A^{\mathrm{rms}}(\Omega)=\frac{N}{2}\frac{h|\beta||H(\Omega)|}{2\sqrt{2}}, \tag{2.38}$$

leading to a signal-to-shot-noise ratio:

$$\mathrm{SNR}(\Omega)=h\sqrt{\frac{N}{2}}\frac{|H(\Omega)|}{2}|\beta|. \tag{2.39}$$

2.2.4 Effect of Light Intensity Fluctuation

When discussing the use of an atom interferometer to measure the phase of light field, the change of the light field intensity caused by a passing GW is not considered. We explain why this term is negligible here.

Take the situation inside resonator as an example. If the interferometer is formed by light field A_{f} and A_{b}, a GW with an amplitude of $h\cos(\Omega_{\mathrm{GW}}t_0)$ is detected. Assume that the gravitational wave amplitude remains unchanged during one interference time of the interferometer and the reflectivity of the second mirror $r = 1$. Then the Rabi frequencies of the interaction between atoms and light in both directions are $\Omega_{\mathrm{b}} = \Omega_{\mathrm{f}} = \Omega_R\left(1 + \frac{h\alpha}{2}\cos(\Omega_{\mathrm{GW}}t_0)\right)$, where α is the coefficient of the amplitude change of the light field caused by a GW. Changes caused by other effects can be calculated similarly. For computational convenience, we assume that it is a Bragg transition ($p_A = p_B$), and the two beams' frequencies are the same. The time evolution of the atomic wave function [59] is simply $|\Phi(t)\rangle = g_n(t)|g, n\hbar k\rangle + g_{-n}(t)|g, -n\hbar k\rangle$, its changes over time satisfing the equations:

$$\frac{dg_n}{dt} = i\frac{|\Omega_{\mathrm{b}}|^2}{\Delta}g_n + i\frac{\Omega_{\mathrm{b}}\Omega_{\mathrm{f}}^*}{\Delta}g_{-n}e^{i\phi} \tag{2.40}$$

$$\frac{dg_{-n}}{dt} = i\frac{|\Omega_{\mathrm{f}}|^2}{\Delta}g_{-n} + i\frac{\Omega_{\mathrm{b}}^*\Omega_{\mathrm{f}}}{\Delta}g_n e^{-i\phi} \tag{2.41}$$

and the solution to these equations are

$$g_n(t_0+t) = e^{i\omega\frac{t}{2}}\left[\left(\cos\frac{\omega t}{2} + \frac{i}{\omega}\left(\frac{|\Omega_{\mathrm{b}}|^2 - |\Omega_{\mathrm{f}}|^2}{\Delta}\right)\sin\frac{\omega t}{2}\right)g_n(t_0) + \frac{i}{\omega}\Omega_E\sin\frac{\omega t}{2}g_{-n}(t_0)e^{i\phi}\right], \tag{2.42}$$

and

$$g_{-n}(t_0+t) = e^{i\omega\frac{t}{2}}\left[\left(\cos\frac{\omega t}{2} - \frac{i}{\omega}\left(\frac{|\Omega_{\mathrm{b}}|^2 - |\Omega_{\mathrm{f}}|^2}{\Delta}\right)\sin\frac{\omega t}{2}\right)g_{-n}(t_0) + \frac{i}{\omega}\Omega_E^*\sin\frac{\omega t}{2}g_n(t_0)e^{-i\phi}\right] \tag{2.43}$$

where Δ is the detuning of laser frequency from transition $|g\rangle \to |e\rangle$, and $|e\rangle$ is the intermediate excited state, $\omega = \frac{|\Omega_{\mathrm{b}}|^2+|\Omega_{\mathrm{f}}|^2}{\Delta}$, $\Omega_E = \frac{2\Omega_{\mathrm{b}}\Omega_{\mathrm{f}}^*}{\Delta}$. After a $\frac{\pi}{2} - \pi - \frac{\pi}{2}$ pulses, we obtain the sensitivity function

$$g(t) = \begin{cases} \sin(\Omega_R t_1) + 2\alpha\, h\cos(\Omega_R t_1)(\pi + \Omega_R t_1), \\ 1, \\ \cos(\Omega_R t_2) + 2\alpha\, h\sin(\Omega_R t_2)(\pi + \Omega_R t_2), \end{cases} \tag{2.44}$$

where $t_1 = t, t_2 = t - T - t_r$ and $0 < t_1 < t_r, 0 < t_2 < t_r$. According to the Eq. 2.35, $\Delta\Phi_{\text{AT}} = \int_{-\infty}^{+\infty} g(t)d\theta(t)$ and $d\theta(t) \propto h$ is the phase change caused by the signal, and the amplitude change contained in $g(t)$ will become the quadratic term of h in $\Delta\Phi_{\text{AT}}$ and will be omitted. Therefore, when using the interferometer to detect the phase change caused by the gravitational wave, it is unnecessary to consider its influence on the laser amplitude.

2.3 Optical Resonator

According to Eq. 1.7, the phase difference caused by GWs between the optical fields is proportional to the length of the light path in one arm of the interferometer. So let us take gravitational waves in the frequency range of 1 Hz to 100 Hz as an example. In order to obtain sufficient detection sensitivity to measure gravitational waves, the arm length of the interferometer is required to reach tens or even hundreds of kilometers. It is impossible to build such a device on the Earth's surface.

To solve this problem, we need the help of optical resonators. Using an optical resonator with a fineness of F, we can amplify the optical path by a factor of $\frac{F}{\pi}$, which of course, does not mean that our signal will also increase accordingly. It is necessary to understand how the optical field in the optical resonator responds to GWs, so in the following content we will use matrix calculations to explain the influence of optical resonators on gravitational wave measurements.

2.3.1 Transmission matrices

In an optical resonator, both the intensity and phase of the optical field vary with the optical path length. There have been in-depth studies about this process [3, 50, 54, 56]; here, we provide a brief introduction to allow for a more complete description.

Assume an optical resonator and an input light field $E_{in} = E_0 e^{-i\omega t}$ such that a passing gravitational wave $h(t) = h\cos(\Omega t + \Theta_h)$ will produce two sidebands on the carrier frequency circulating in the resonator, after a round trip [37]. The light fields circulating inside the

cavity are E_f and E_b, forward and backward going, respectively,

$$E_f(t) = (S_{f0} + \frac{h}{2} S_{f-} e^{-i\Omega t} + \frac{h}{2} S_{f+} e^{i\Omega t}) e^{-i\omega t} \text{ and} \tag{2.45}$$

$$E_b(t) = (S_{b0} + \frac{h}{2} S_{b-} e^{-i\Omega t} + \frac{h}{2} S_{b+} e^{i\Omega t}) e^{-i\omega t} \tag{2.46}$$

Here Ω is the frequency of a incident gravitational wave, and $S_0,\ S_+,$ and S_- represent the coefficients of the carrier and the sidebands. We define two rank three vectors composed of these amplitude coefficients

$$\mathcal{A}_f = (S_{f0}, S_{f-}, S_{f+}) \text{ and} \tag{2.47}$$

$$\mathcal{A}_b = (S_{b0}, S_{b-}, S_{b+})\,. \tag{2.48}$$

The evolution of the light field in the cavity can then be expressed as a matrix transformation.

$$\mathcal{A}_b = i\, r \mathbf{T} \mathcal{A}_f \tag{2.49}$$

where $\mathbf{T}$ is the linear round trip operator

$$\mathbf{T} = e^{2iu} \begin{pmatrix} 1, & 0, & 0 \\ -i\, u\, \text{sinc}(\nu) e^{i\nu}, & e^{2i\nu}, & 0 \\ -i\, u\, \text{sinc}(\nu) e^{-i\nu}, & 0, & e^{-2i\nu} \end{pmatrix} \tag{2.50}$$

with $u \equiv \frac{\omega L}{c}$ and $\nu \equiv \frac{\Omega L}{c}$. As shown in Fig. 2.4, we define a set of vectors representing the light field at each position of the resonant cavity,

$$\mathcal{A}_\text{b} = ir \mathbf{T} \mathcal{A}_\text{f}, \tag{2.51}$$

$$\mathcal{A}_\text{f} = t\mathcal{A}_0 + ir\mathcal{A}_\text{b}, \tag{2.52}$$

$$\mathcal{A}_\text{ref} = ir\mathcal{A}_0 + t\mathcal{A}_\text{b}, \text{ and} \tag{2.53}$$

$$\mathcal{A}_\text{trans} = t\mathcal{A}_\text{f}\sqrt{\mathbf{T}}; \tag{2.54}$$

where r and t are the resonator mirrors' reflection coefficient and transmission coefficient.

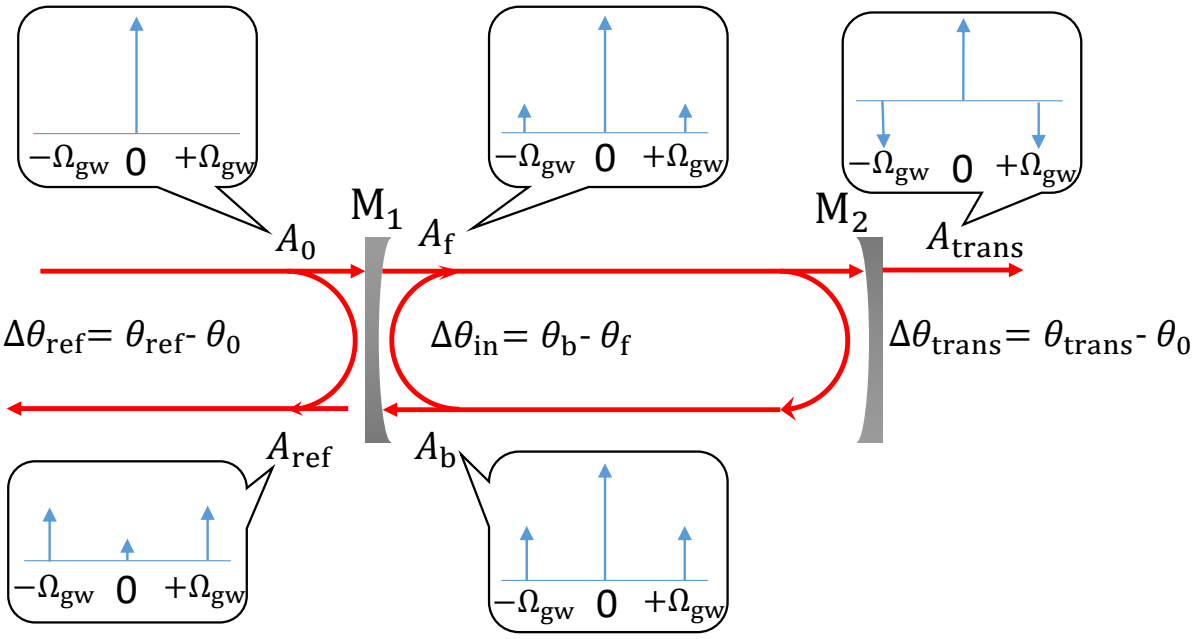

Figure 2.4: The light field and phase at each position in a resonator. The input, transmitted, and reflected light, as well as the light in two directions inside of the resonator are defined as $A_0, A_{\text{trans}}, A_{\text{ref}}, A_{\text{f}}, A_{\text{b}}$ respectively. We show the qualitative relationship between the side-bands and carriers in the bubbles.

Rearrange these conditions such that

$$\begin{aligned}
\mathcal{A}_f &= \frac{t_1\mathcal{A}_0}{1+r^2\mathbf{T}},\\
\frac{\mathcal{A}_b}{\mathcal{A}} &= ir\mathbf{T},\\
\frac{\mathcal{A}_{\text{ref}}}{\mathcal{A}_0} &= \frac{i(r+r\mathbf{T})}{1+r^2\mathbf{T}}, \text{ and}\\
\frac{\mathcal{A}_{\text{trans}}}{\mathcal{A}_0} &= \frac{(1-r^2)\sqrt{\mathbf{T}}}{1+r^2\mathbf{T}}.
\end{aligned} \tag{2.55}$$

We can use these matrices, thus rearranged, to calculate the field's expression at any point in the resonator. All fields calculated will be of the form

$$E_X = E_0\left[S_0 + \frac{h}{2}S_-e^{-i\Omega t} + \frac{h}{2}S_+e^{i\Omega t}\right], \tag{2.56}$$

Considering $h \ll 1$, we have $e^x \approx 1+x$, when $x \ll 1$. In calculations here and later, this approximation will be used multiple times to simplify the form of the fields,

$$\begin{aligned}
E_X &= E_0S_0\exp\big(\frac{h}{2}\frac{|S_-|}{|S_0|}e^{-i(\Omega t-\Delta\vartheta_-)} + \frac{h}{2}\frac{|S_+|}{|S_0|}e^{i(\Omega t+\Delta\vartheta_+)}\big)\\
&= E_0S_0\exp\left(\frac{h}{2}\frac{|S_-|}{|S_0|}\cos(\Omega t-\Delta\vartheta_-) + \frac{h}{2}\frac{|S_+|}{|S_0|}\cos(\Omega t+\Delta\vartheta_+)\right)\\
&\times\exp\left(i\big(-\frac{h}{2}\frac{|S_-|}{|S_0|}\sin(\Omega t-\Delta\vartheta_-) + \frac{h}{2}\frac{|S_+|}{|S_0|}\sin(\Omega t+\Delta\vartheta_+)\big)\right),
\end{aligned} \tag{2.57}$$

where ϑ_0, ϑ_+, and ϑ_- are the complex angles of S_0, S_+, and S_- respectively; note, $\Delta\vartheta_+ = \vartheta_+ - \vartheta_0$ and $\Delta\vartheta_- = \vartheta_- - \vartheta_0$. See Fig. 2.5 for their change near the resonance. In this equation, the first exponential function represents the change in amplitude, and its index is

$$\begin{aligned}
&|S_0| + \frac{h}{2}\big(|S_-|\cos(\Omega t-\Delta\vartheta_-) + |S_+|\cos(\Omega t+\Delta\vartheta_+)\big)\\
=&|S_0| + \frac{h|\alpha|}{2}\cos(\Omega t+\Theta_\alpha)
\end{aligned} \tag{2.58}$$

where $\alpha = |\alpha|e^{i\Theta_\alpha} = |S_-|e^{i\Delta\vartheta_-} + |S_+|e^{-i\Delta\vartheta_+}$. The second exponential function is the phase change, and the index number is

$$\begin{aligned}
&i\left(-\frac{h}{2}\frac{|S_-|}{|S_0|}\sin(\Omega t-\Delta\vartheta_-) + \frac{h}{2}\frac{|S_+|}{|S_0|}\sin(\Omega t+\Delta\vartheta_+)\right)\\
=&i\frac{h|\beta|}{2}\sin(\Omega t)
\end{aligned} \tag{2.59}$$

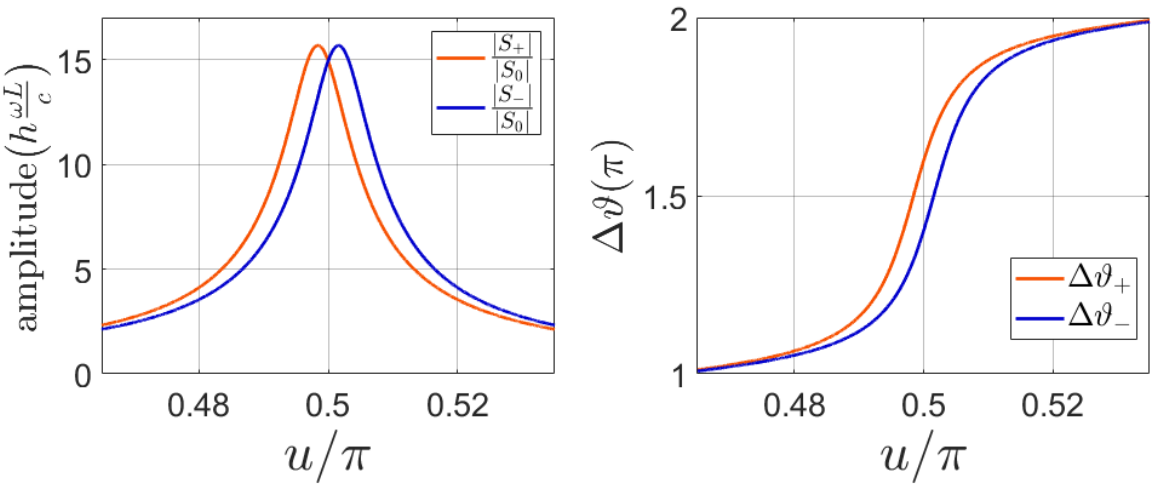

Figure 2.5: The amplitudes and phases of the sidebands near to resonance inside the resonator. The orange line and the blue line respectively represent two sidebands. At the resonance point, the amplitudes of the two are equal, the phase to the carrier is symmetrical with $\frac{\pi}{2}$ at the center, which means $\cos(\Delta\vartheta_+) = -\cos(\Delta\vartheta_-)$ and $\sin(\Delta\vartheta_+) = \sin(\Delta\vartheta_-)$. This explains why $|\alpha| = 0$ at the resonant point in Fig. 2.6

where $\beta = |\beta|e^{i\Theta_\beta} = \frac{|S_+|}{|S_0|}e^{i\Delta\vartheta_+} - \frac{|S_-|}{|S_0|}e^{-i\Delta\vartheta_-}$. The total field is expressed as,

$$\begin{aligned} E_X &= E_0\left(|S_0| + \frac{h}{2}|\alpha|\cos(\Omega t + \Theta_\alpha)\right)e^{-i\omega_0 t} \times \exp\left(i\frac{h}{2}|\beta|\sin(\Omega t + \Theta_\beta)\right) \\ &= E_0 e^{-i\omega_0 t}(|S_0| + \Delta S) \times e^{i\Delta\theta} \end{aligned} \tag{2.60}$$

where $\Delta S = \frac{h}{2}|\alpha|\cos(\Omega t + \Theta_\alpha)$ is the change of the amplitude caused by GW, $\Delta\theta = \frac{h}{2}|\beta|\sin(\Omega t + \Theta_\beta)$ is the phase fluctuation caused by GW. Here we use the GW signal as the example; other signals and noises are calculated similarly.

2.3.2 Optical field in and out of the resonator

According to Eq. 2.39, The SNR using atom detection is proportional to the coefficients $|\beta|$. Likewise, if we detect the light field with a photodetector, its SNR should be proportional to $|\alpha|$[1]. Combining Eq. 2.45 and Eq. 2.55, one can calculate the sideband of the light field at different positions, thus $|\alpha|$ and $|\beta|$.

[1]Here is to directly detect a beam of light with a photodetector, and its SNR is not the same as the SNR of the interference of the two beams in Eq. **??**.

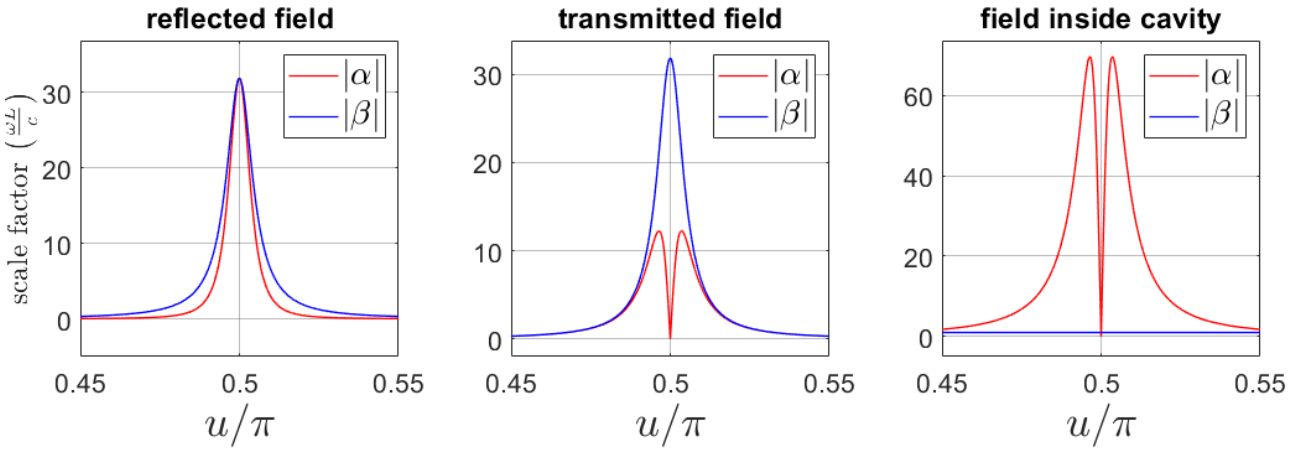

Figure 2.6: The change of the scale factors $|\alpha|$ and $|\beta|$ for $\Omega = 1$ Hz near the resonant point with parameters for MIGA [60]: a length of 150 m, a finesse of 100, and $\omega_p = \pi \cdot 10^4$.

2.3.2.1 Field inside the resonator

Inside the resonator, the expressions of the two light fields propagating forward and backward are:

$$E_f(t) = E_0\sqrt{1-r^2}\left(\frac{1}{1+e^{2iu}r^2} + \frac{iu\,hr^2\,e^{2iu}e^{i(\Omega t-\nu)}}{2(1+e^{2iu}r^2)(1+r^2e^{2i(u-\nu)})} + \frac{iu\,hr^2\,e^{2iu}e^{i(-\Omega t+\nu)}}{2(1+e^{2iu}r^2)(1+r^2e^{2i(u+\nu)})}\right)e^{i\omega t} \quad \text{and} \tag{2.61}$$

$$E_b(t) = ir\sqrt{1-r^2}E_0\left(\frac{1}{1+e^{2iu}r^2} - \frac{iu\,h\,e^{2iu}e^{i(\Omega t-\nu)}}{2(1+e^{2iu}r^2)(1+r^2e^{2i(u-\nu)})} - \frac{iu\,h\,e^{2iu}e^{i(-\Omega t+\nu)}}{2(1+e^{2iu}r^2)(1+r^2e^{2i(u+\nu)})}\right)e^{i\omega t}. \tag{2.62}$$

When the cavity is at the resonance point, $|\alpha|$ of the fields are

$$|\alpha|_f = |\alpha|_b = 0. \tag{2.63}$$

The $|\beta|$ of these two fields are

$$|\beta|_f = \frac{u\,r^2}{\sqrt{1+r^4-2r^2\cos(2\nu)}} \quad \text{and} \tag{2.64}$$

$$|\beta|_b = \frac{u}{\sqrt{1+r^4-2r^2\cos(2\nu)}}. \tag{2.65}$$

For an atom interferometer, the phase changes of the two light fields in the resonator are $\Delta\theta_b = \frac{h}{2}|\beta|_b\sin(\Omega t + \Theta_{\beta b})$ and $\Delta\theta_f = \frac{h}{2}|\beta|_f\sin(\Omega t + \Theta_{\beta f})$, while what is detected by the atom

is the phase difference $\Delta\theta_{in} = \Delta\theta_b - \Delta\theta_f$. The factor of this $\Delta\theta_{in}$ is

$$\begin{aligned} |\beta|_{in} &= \sqrt{|\beta|_b^2 + |\beta|_f^2 - 2|\beta|_b|\beta|_f \cos\left(\Theta_{\beta_f} - \Theta_{\beta_b}\right)} \\ &= \frac{u(1-r^2)}{\sqrt{1 + r^4 - 2r^2\cos(2\nu)}}. \end{aligned} \tag{2.66}$$

Since $\nu = \frac{\Omega L}{c} \ll 1$, expand the equation to second order of ν, we have

$$|\beta|_{in} = 2u\cos(\theta_p). \tag{2.67}$$

where $\cos(\theta_p) = \sqrt{\frac{1}{1+\frac{\Omega^2}{2\omega_p^2}}}$, $\omega_p = \frac{\pi c}{2LF}$ is the frequency of the cavity pole, and $\frac{r^2+1}{r^2-1} \approx \frac{2F}{\pi}$ with F being the finesse of the cavity.

We can also extend the result to a position $x \neq 0$ in the resonator by modification of previously established formulae,

$$\mathcal{A}_f = t\mathcal{A}_0\mathbf{T}(x) + ir\mathbf{A}_b\mathbf{T}(2x) \text{ and} \tag{2.68}$$

$$\mathcal{A}_b = ir\mathcal{A}_f\mathbf{T}(2L - 2x), \tag{2.69}$$

with

$$\mathbf{T}(x) = e^{2iu(x)} \begin{pmatrix} 1 & 0 & 0 \\ -iu(x)e^{i\nu(x)} & e^{2i\nu(x)} & 0 \\ -iu(x)e^{-i\nu(x)} & 0 & e^{-2i\nu(x)} \end{pmatrix} \tag{2.70}$$

where $u(x) = \frac{\omega x}{2c}$ and $\nu(x) = \frac{\Omega x}{2c}$. At the resonance, we still have $|\alpha| = 0$. The phase difference is

$$\Delta\theta_{AB}(x) = u\,h\cos(\theta_p)(1 - \frac{x}{L})\cos(\Omega t + \theta_p), \tag{2.71}$$

leading to

$$|\beta|_{in} = 2u\cos(\theta_p)(1 - \frac{x}{L}). \tag{2.72}$$

2.3.2.2 Reflected field

With the same steps, we get the reflection field

$$\begin{aligned} E_{ref}(t) &= irE_0\frac{1+\kappa}{1+r^2\kappa}\times \\ &\left(1 - \frac{k\,h\,t^2\kappa(\kappa r^2\cos(\Omega t + \nu) + \cos(\Omega t - \nu))}{(1+\kappa)(\kappa^2 r^4 + 2\kappa r^2\cos(2\nu) + 1)}\right) \end{aligned} \tag{2.73}$$

with $\kappa = e^{2iu}$. At resonance,

$$E_{ref}(t) = -rE_0 h\, u \left(0 + \frac{r^2\cos(\Omega t+\nu) - \cos(\Omega t-\nu)}{r^4 - 2r^2\cos(2\nu)+1}\right). \tag{2.74}$$

Note that there is no imaginary part in this result, that is to say, $|S_0| = 0$. So $\beta = |\beta|e^{i\Theta_\beta} = \frac{|S_+|}{|S_0|}e^{i\Delta\vartheta_+} - \frac{|S_-|}{|S_0|}e^{-i\Delta\vartheta_-}$ is divergent, and

$$|\alpha|_{ref} = \mathrm{Re}(S_+) + \mathrm{Re}(S_-) = \frac{F}{\pi} 2u\cos(\theta_p). \tag{2.75}$$

Although the value of $|\beta|$ at the resonance point cannot be obtained, it is possible to study the changes of it near the resonant point, with $u = 2n\pi + \frac{\pi}{2} + \delta$ and $\kappa = -1 - 2i\delta$, taking the fist order of δ, we have

$$|\beta|_{ref} = 2u\frac{F}{\pi}\cos(\theta_p). \tag{2.76}$$

In order to make the $|\beta|$ curve complete in Fig. 2.6(a), we also use the value of this expression at the resonance point.

2.3.2.3 Transmitted field

The expression of the transmitted field is

$$\begin{aligned} E_{trans}(t) = {} & irE_0\frac{1+\kappa}{1+r^2\kappa} \\ & \times\left(1 - \frac{iu\,h\,\kappa\, e^{-i\nu+i\Omega t}rt^2}{2(1+r^2\kappa)(1+e^{-2i\nu}r^2\kappa)} - \frac{iu\,h\,\kappa\, e^{i\nu-i\Omega t}rt^2}{2(1+r^2\kappa)(1+e^{2i\nu}r^2\kappa)}\right). \end{aligned} \tag{2.77}$$

According to the same method as the previous two subsections, at the resonant point $\kappa = -1$, we still have

$$|\alpha|_{trans} = 0, \quad \text{and} \tag{2.78}$$

$$|\beta|_{trans} = -2u\frac{F}{\pi}\cos(\theta_p). \tag{2.79}$$

The variation of these quantities near the resonant point are shown in Fig. 2.6(a), where $|\alpha|$ has a maximum near $\frac{1}{2}\arccos\left(\frac{\sqrt{1+14r^2+r^8}-r^4-1}{2r^2}\right)$.

With all these results above, we can draw the curve of $|\alpha|$ and $|\beta|$ near the resonance point at different positions (Fig. 2.6).

2.3.3 Noise Analysis

Rolf Landauer once said "The noise is the signal" [61, 62]. This idea points out the essence of measurement is raising the "noise" you want to measure while suppressing other noises. For our experiment, this is the case that there are several effects that affect the final result. In order to improve the SNR, we must first clarify the response of the experimental results to different noises. The main noise sources in the experiment include: the position noise $\delta x_{1,2}$ of the two mirrors forming the resonator, the laser frequency noise δf, and the atomic position noise ΔX caused by the local acceleration.

In the previous section, we pointed out that gravitational waves change the travel time of the light field and thus cause phase differences; similarly, these noises can also cause time differences:

$$\Delta t_r^{GW} = \frac{2(L-X)}{c} - h\frac{L-X}{c}\mathrm{sinc}\left(\Omega_{\mathrm{GW}}\frac{L-X}{c}\right)\cos\left(\Omega_{\mathrm{GW}}\left(t-\frac{L-X}{c}\right)\right) \tag{2.80}$$

$$\Delta t_r^{\mathrm{mirror}} = \frac{2(L-X)}{c} + \frac{2\delta x}{c}\cos\left(\Omega_{\delta x}\left(t-\frac{L-X}{c}\right)\right) \tag{2.81}$$

$$\Delta t_r^{f} = \frac{2(L-X)}{c}, \tag{2.82}$$

and the motion of atom can be seen as the the simultaneous movement of two mirrors. The corresponding field changes $A' = TA$ are

$$\begin{aligned} T_{GW} &= e^{i\omega_0\frac{2(L-X)}{c}}e^{ih\frac{\omega_0(L-X)}{c}\mathrm{sinc}\left(\Omega_{\mathrm{GW}}\frac{L-X}{c}\right)\cos\left(\Omega_{\mathrm{GW}}\left(t-\frac{L-X}{c}\right)\right)} \\ &= e^{2iu_X}\left(1 - h\,i\,u_X\mathrm{sinc}(\nu_{GW})\left(e^{i\Omega_{\mathrm{GW}}t}e^{-i\nu_{GW}} + e^{-i\Omega_{\mathrm{GW}}t}e^{i\nu_{GW}}\right)\right) \end{aligned} \tag{2.83}$$

$$\begin{aligned} T_{\delta x} &= e^{i\omega_0\frac{2(L-X)}{c}}e^{i\omega_0\frac{2\delta x}{c}\cos\left(\Omega_{\delta x}(t-\frac{L-X}{c})\right)} \\ &= e^{2iu_X}\left(1 + \frac{\delta x}{L}\,i\,u_L(e^{i\Omega_{\delta x}t}e^{-i\nu_{\delta x}} + e^{-i\Omega_{\delta x}t}e^{i\nu_{\delta x}})\right) \end{aligned} \tag{2.84}$$

$$\begin{aligned} T_{\Delta X} &= e^{i\omega_0\frac{2(L-X)}{c}}e^{-i\omega_0\frac{2\Delta X}{c}\cos(\Omega_{\Delta X}X)} \\ &= e^{2iu_X}\left(1 + \frac{\Delta X}{L}\,i\,u_L(e^{i\Omega_{\delta x}t} + e^{-i\Omega_{\delta x}t})\right) \end{aligned} \tag{2.85}$$

where $u_X = \frac{\omega_0(L-X)}{c}$, $u_L = \frac{\omega_0(L)}{c}$, and $\nu = \frac{\Omega L}{c}$.

The noise from the laser is composed of both frequency noise and phase noise. Phase noise, in our case, is the variation in the offset of the phase of our applied laser field compared to the system reference. This offset depends only on the distance between the light fields but

will not increase with the light propagation, while the frequency noise will accumulate as the light field propagates.

$$\begin{aligned} T_\theta &= e^{i\left(\omega_0+\delta\omega_\theta\cos\left(\Omega_\phi(t-\frac{2(L-X)}{c})\right)\right)\frac{2(L-X)}{c}} \\ &= e^{2iu_X}\left(1+\frac{\delta\omega_\theta}{\omega_0}i\,u_X\left(e^{i\Omega_\theta t}e^{-2i\nu_\theta}+e^{-i\Omega_\theta t}e^{2i\nu_\theta}\right)\right) \end{aligned} \tag{2.86}$$

and the phase difference comes from the frequency is

$$\begin{aligned} \Delta\theta &= \omega_0\big(1+\frac{\delta f}{f_0}\cos(\Omega_{\delta f}t)\big)t-\omega_0\left(1+\frac{\delta f}{f_0}\cos\left(\Omega_{\delta f}(t-\frac{2(L-X)}{c})\right)\right)(t-\frac{2(L-X)}{c}) \\ &= \omega_0\frac{\delta f}{f_0}\big(\cos(\Omega_{\delta f}t)-\cos(\Omega_{\delta f}t-2\nu_{\delta f})\big)t+2u_X\left(1+\frac{\delta f}{f_0}\cos\left(\Omega_{\delta f}t-2\nu_{\delta f}\right)\right). \end{aligned} \tag{2.87}$$

By keeping only the zero and first order of $\nu_{\delta f}$ we have:

$$\Delta\theta = 2u_X+2u_X\frac{\delta f}{f_0}\cos\left(\Omega_{\delta f}t-2\nu_{\delta f}\right)-2\frac{\delta f}{f_0}\sin(\Omega_{\delta f}t)\nu_{\delta f}\omega_0 t. \tag{2.88}$$

Here t is the propagation time of the light field from the light source. We have three phase difference terms here. The first term is the phase difference between two light fields $2L-2X$ apart without noise, the second term is caused by phase noise at $2L-2X$ distance, and the third term is determined by the propagation time of the field; this item is very troublesome for our calculation. However, the maximum value of this term can be estimated. For the case of no resonant cavity, $t<\frac{2L}{c}$, and for a resonant cavity, according to the definition of resonant cavity fineness, $t<\frac{2LF}{\pi c}$, here we consider the case of a resonant cavity,

$$\nu_{\delta f}\omega_0 t<\frac{\Omega_{\delta f}(L-X)}{c}\omega_0\frac{2LF}{\pi c}=u_X\frac{\Omega_{\delta f}}{\omega_p}, \tag{2.89}$$

the target frequency range is $\frac{\Omega_{\delta f}}{\omega_p}\ll 1$, so this item can be ignored

$$\begin{aligned} \Delta\theta &\approx 2u_X+2u_X\frac{\delta f}{f_0}\cos\left(\Omega_{\delta f}t-2\nu_{\delta f}\right) \\ &= 2u_X+2u_X\frac{\delta f}{f_0}\big(e^{i\Omega_{\delta f}t}e^{-2\nu_{\delta f}}+e^{-i\Omega_{\delta f}t}e^{2\nu_{\delta f}}\big). \end{aligned} \tag{2.90}$$

So the transfor matrices of the optical cavity to different noises are

$$\mathbf{T}_{GW}=e^{2iu_X}\begin{pmatrix} 1 & 0 & 0 \\ -iu_X\mathrm{sinc}(\nu_{GW})e^{i\nu_{GW}} & e^{2i\nu_{GW}} & 0 \\ -iu_X\mathrm{sinc}(\nu_{GW})e^{-i\nu_{GW}} & 0 & e^{-2i\nu_{GW}}, \end{pmatrix}, \tag{2.91}$$

$$\mathbf{T}_{\delta x} = e^{2iu_X} \begin{pmatrix} 1 & 0 & 0 \\ iu_L e^{i\nu_{\delta x}} & e^{2i\nu_{\delta x}} & 0 \\ iu_L e^{-i\nu_{\delta x}} & 0 & e^{-2i\nu_{\delta x}}, \end{pmatrix}, \tag{2.92}$$

$$\mathbf{T}_{\Delta X} = e^{2iu_X} \begin{pmatrix} 1 & 0 & 0 \\ iu_L & e^{2i\nu_{\Delta X}} & 0 \\ iu_L & 0 & e^{-2i\nu_{\Delta X}}, \end{pmatrix}, \tag{2.93}$$

$$\mathbf{T}_{\theta} = e^{2iu_X} \begin{pmatrix} 1 & 0 & 0 \\ iu_X e^{2i\nu_\theta} & e^{2i\nu_\theta} & 0 \\ iu_X e^{-2i\nu_\theta} & 0 & e^{-2i\nu_\theta}, \quad \text{and} \end{pmatrix}, \quad \text{and} \tag{2.94}$$

$$\mathbf{T}_{\delta f} = e^{2iu_X} \begin{pmatrix} 1 & 0 & 0 \\ iu_X e^{2i\nu_{\delta f}} & e^{2i\nu_{\delta f}} & 0 \\ iu_X e^{-2i\nu_{\delta f}} & 0 & e^{-2i\nu_{\delta f}} \end{pmatrix}. \tag{2.95}$$

After the transmission matrices are obtained, the phase response of each noise can be obtained in the same way as the calculation of the phase change caused by gravitational waves.

2.4 Atom Gradiometry

When measuring gravitational waves through the phase change of the laser, the use of mirrors cannot be avoided. The mirror will bring a series of noises, including its position noise and direction noise, especially in the low-frequency range. An effective way to suppress the mirror noise is to use the mirror suspension system[63], compared to fixing the mirror on the optical table throughly, using the suspension system can effectively reduce noise. Assuming that the distance between the mirror and the suspension point is l, and the additional damping coefficient is k when it deviates from the lowest point distance x, the force it receives is:

$$F = \left(k - \frac{Mg}{l}\right) x \tag{2.96}$$

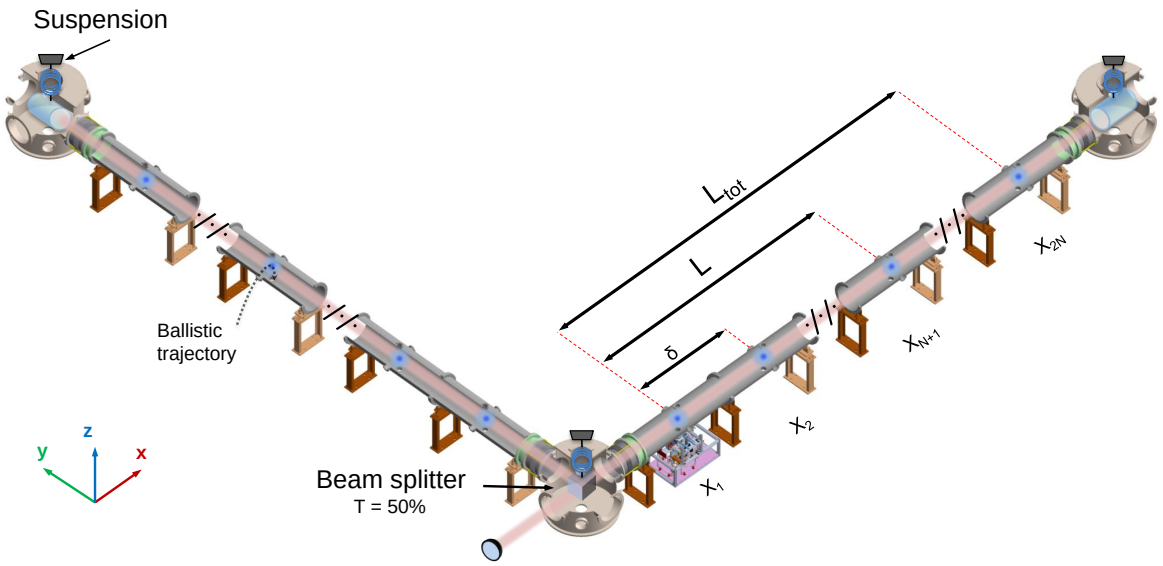

Figure 2.7: The diagram of the structure of the atom gradiometer [27], the length of two mutually perpendicular arms is L_{tot}, 2N+1 atom interferometers are plased in each arm, and the distance between the AI is δ.

The resonance frequency is

$$f_0 = \frac{1}{2\pi}\sqrt{\frac{k}{M} - \frac{g}{l}}. \tag{2.97}$$

By adjusting the suspension length and the spring coefficient k, the resonance frequency can appear outside the target frequency range.

According to the calculation, the phase of the GW signal is proportional to the position $L - X$ of the AI, while the mirror position noise is not. Based on this, an atom gradiometer [64] scheme was proposed as Fig. 2.7. In a single cavity, the phase response of the AI to the GW signal and other noises is:

$$\begin{aligned}\Delta\Phi_{AT}(X,t) = \frac{2\omega L}{c}\Bigg(&\frac{L-X}{L}\frac{h(t)}{2} + \frac{\Delta X(t)}{L} + \frac{L-X}{L}\frac{\delta f(t)}{f_0} + \frac{\delta x_2(t)}{L} \\ &+ \frac{1}{\omega_p}\left[\frac{L-X}{L}\frac{h'(t)}{2} + \frac{\Delta X'(t)}{L} + \frac{L-X}{L}\frac{\delta f'(t)}{f_0} + \frac{L-X}{L}\frac{\delta x_2'(t)}{L} - \frac{L-X}{L}\frac{\delta x_1'(t)}{L}\right] \\ &+ \frac{1}{\omega_p^2}\left[\frac{L-X}{L}\frac{h''(t)}{2} + \frac{\Delta X''(t)}{L} + \frac{L-X}{L}\frac{\delta f''(t)}{f_0} + \frac{(L-X)^2}{L^2}\frac{\delta x_2''(t)}{L} - \frac{(L-X)^2}{L^2}\frac{\delta x_1''(t)}{L}\right]\Bigg) \\ &\otimes g(t) + \epsilon(X,t).\end{aligned} \tag{2.98}$$

Where $h(t)$ represents gravitational waves, $\Delta X(t)$ is the displacement noise of atoms along

the detection direction, $\delta f(t)$ is the frequency noise of the laser, δx_1, and δx_2 is the noise of the two mirrors of the resonator, $\epsilon(X,t)$ is the detection error, $\otimes$ represents convolution, prime ($'$) and double-prime ($''$) represent the first and second order derivatives of time respectively, and higher-order noise is ignored here.

The differential signal between two atom interferometers placed inside the cavity at positions X1 and X2 is, therefore:

$$\begin{aligned}\Delta\Phi_{AT}(X_1,t)-\Delta\Phi_{AT}(X_2,t)=\frac{2\omega L}{c}\Bigg(&\frac{X_1-X_2}{L}\frac{h(t)}{2}+\frac{X_1-X_2}{L}\frac{\delta f(t)}{f_0}+\frac{\Delta X_1(t)-\Delta X_2(t)}{L}\\&+\frac{1}{\omega_p}\left[\frac{X_1-X_2}{L}\frac{h^{'}(t)}{2}+\frac{X_1-X_2}{L}\frac{\delta f^{'}(t)}{f_0}+\frac{X_1-X_2}{L}\frac{\delta x_2^{'}(t)-\delta x_1^{'}(t)}{L}+\frac{\Delta X_1^{'}(t)-\Delta X_2^{'}(t)}{L}\right]\\&+\frac{1}{\omega_p^2}\left[\frac{X_1-X_2}{L}\frac{h^{''}(t)}{2}+\frac{X_1-X_2}{L}\frac{\delta f^{''}(t)}{f_0}+\frac{X_1^2-X_2^2-2X_1+2X_2}{L^2}\left(\frac{\delta x_2^{''}(t)}{L}-\frac{\delta x_1^{''}(t)}{L}\right)\right.\\&\left.+\frac{\Delta X_1^{''}(t)-\Delta X_2^{''}(t)}{L}\right]\Bigg)\otimes g(t)+\epsilon(X_1,t)+\epsilon(X_2,t).\end{aligned}\tag{2.99}$$

Compared with the optical interferometer, the gradiometer has the advantage of removing the first-order term of the mirror position noise, making it an effective method for measuring gravitational waves in the low-frequency range. *The disadvantage is that the existence of an optical resonator can only provide power amplification, but cannot amplify the phase signal like an optical interferometer.*

2.5 Three-cavity system

Compared with the intra-cavity phase, both the reflected and transmitted phase have an amplification factor $\frac{F}{\pi}$ (see the $|\beta|$ curve in Fig. 2.6). This difference presents an opportunity to use the transmitted light fields to form an AI outside the cavity, which would take advantage of this amplification effect. A schematic of our idea is shown in Fig. 2.8(a). The light passes through the beam splitter and is divided into two perpendicular beams of the same intensity. The two beams were injected into two optical cavities with the same parameters. A standing wave field interacting with atoms is formed by the transmitted light of these two optical cavities. In addition to the two optical cavities, the output mirror of one optical cavity will reflect the transmitted light of the other cavity, thus forming a third optical resonant

cavity (Fig. **??**).

To analyze the response of such a system to a signal, we take a GW with a h_+ polarization as an example, the transfer matrix equations for this system are:

$$E_1^+ = ir\mathbf{X}_{1l}E_1^- + t\sqrt{\mathbf{X}_{1l}}E_{in} \tag{2.100}$$

$$E_1^- = ir\mathbf{X}_{1r}E_1^+ + t\sqrt{\mathbf{X}_{1r}}\sqrt{\mathbf{X}_{2l}}E_2^- \tag{2.101}$$

$$E_2^+ = ir\mathbf{X}_{2l}E_2^- + t\sqrt{\mathbf{X}_{2l}}\sqrt{\mathbf{X}_{1r}}E_1^+ \tag{2.102}$$

$$E_2^- = ir\mathbf{X}_{2r}E_2^+ + t\sqrt{\mathbf{X}_{2r}}\sqrt{\mathbf{X}_{3l}}E_3^- \tag{2.103}$$

$$E_3^+ = ir\mathbf{X}_{3l}E_3^- + t\sqrt{\mathbf{X}_{3l}}\sqrt{\mathbf{X}_{2r}}E_2^+ \tag{2.104}$$

$$E_3^- = ir\mathbf{X}_{3r}E_3^+ + t\sqrt{\mathbf{X}_{3r}}E_{in}^{'}. \tag{2.105}$$

The light field represented by each E is shown in Fig. 2.8(b), and

$$\mathbf{X}_n = e^{2iu_n}\begin{pmatrix} 1, & 0, & 0 \\ -i\,k_n\,u_n e^{i\nu_n}, & e^{2i\nu_n}, & 0 \\ -i\,k_n\,u_n e^{-i\nu_n}, & 0, & e^{-2i\nu_n} \end{pmatrix}, \tag{2.106}$$

The k_n and ν_n in the formula can be adjusted according to the length of the three cavities and the position of the atom source to obtain the results at different positions. From these formulas it can be deduced

$$\begin{aligned} E_3^+ &= ir\mathbf{X}_{3l}(ir\mathbf{X}_{3r}E_3^+ + t\sqrt{\mathbf{X}_{3r}}E_{in}^{'}) + t\sqrt{\mathbf{X}_{3l}}\sqrt{\mathbf{X}_{2r}}E_2^+ \\ \Rightarrow (1 + r^2\mathbf{X}_{3l}\mathbf{X}_{3r})E_3^+ &= t(ir\mathbf{X}_{3l}\sqrt{\mathbf{X}_{3r}}E_{in}^{'} + \sqrt{\mathbf{X}_{3l}}\sqrt{\mathbf{X}_{2r}}E_2^+) \\ \Rightarrow E_3^+ &= \frac{t(ir\mathbf{X}_{3l}\sqrt{\mathbf{X}_{3r}}E_{in}^{'} + \sqrt{\mathbf{X}_{3l}}\sqrt{\mathbf{X}_{2r}}E_2^+)}{1 + r^2\mathbf{X}_{3l}\mathbf{X}_{3r}}, \quad \text{and} \end{aligned} \tag{2.107}$$

$$\begin{aligned} E_3^- &= ir\mathbf{X}_{3r}\frac{t(ir\mathbf{X}_{3l}\sqrt{\mathbf{X}_{3r}}E_{in}^{'} + \sqrt{\mathbf{X}_{3l}}\sqrt{\mathbf{X}_{2r}}E_2^+)}{1 + r^2\mathbf{X}_{3l}\mathbf{X}_{3r}} + t\sqrt{\mathbf{X}_{3r}}E_{in}^{'} \\ &= \frac{irt\mathbf{X}_{3r}\sqrt{\mathbf{X}_{3l}}\sqrt{\mathbf{X}_{2r}}E_2^+ + t\sqrt{\mathbf{X}_{3r}}E_{in}^{'}}{1 + r^2\mathbf{X}_{3l}\mathbf{X}_{3r}}. \end{aligned} \tag{2.108}$$

Here we take an approximation $\mathbf{X}_{3l}\mathbf{X}_{3r} - \mathbf{X}_{3r}\mathbf{X}_{3l} = 0$ as $\nu \ll 1$.

Similarly,

$$\begin{aligned} E_1^- &= \frac{t(ir\mathbf{X}_{1r}\sqrt{\mathbf{X}_{1l}}E_{in} + \sqrt{\mathbf{X}_{1r}}\sqrt{\mathbf{X}_{2l}}E_2^-)}{1 + r^2\mathbf{X}_{1r}\mathbf{X}_{1l}}, \\ E_1^+ &= \frac{irt\mathbf{X}_{1l}\sqrt{\mathbf{X}_{1r}}\sqrt{\mathbf{X}_{2l}}E_2^- + t\sqrt{\mathbf{X}_{1l}}E_{in}}{1 + r^2\mathbf{X}_{1r}\mathbf{X}_{1l}}, \end{aligned} \tag{2.109}$$

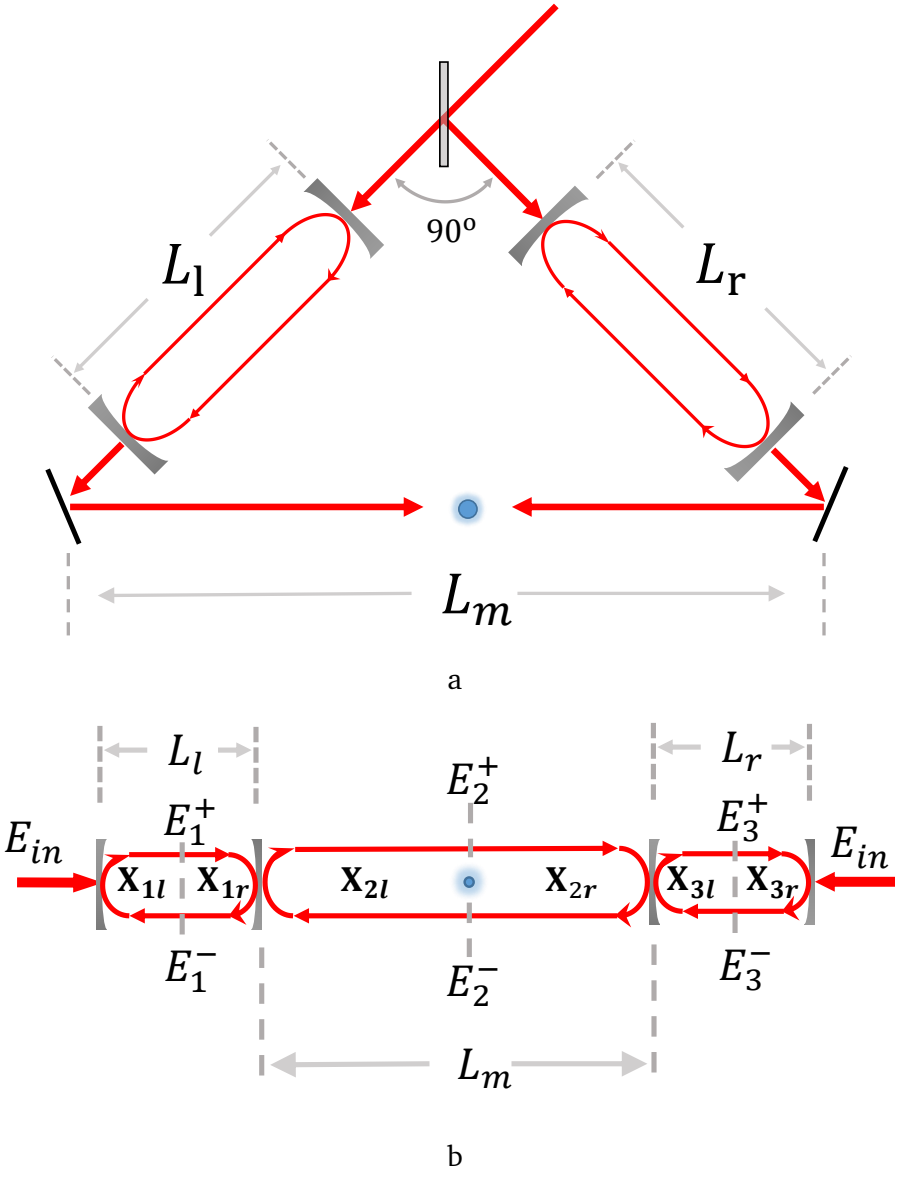

Figure 2.8: (a) Interferometry using two resonant cavities. L_l and L_r are the lengths of the two cavities respectively, and L_m is the equivalent length of the third cavity, $L_m = 2L_m = 2L_l = 2L$. This structure is equivalent to a three-cavity system shown in the bottom figure. (b) X_1,X_2 and X_3 respectively represent the propagation matrix of light in the resonator left, from the resonant cavity to the atom and in resonator right.

$$
\begin{aligned}
E_2^+ &= ir\mathbf{X}_{2l}E_2^- + t\sqrt{\mathbf{X}_{2l}}\sqrt{\mathbf{X}_{1r}}\frac{irt\mathbf{X}_{1l}\sqrt{\mathbf{X}_{1r}}\sqrt{\mathbf{X}_{2l}}E_2^- + t\sqrt{\mathbf{X}_{1l}}E_{in}}{1+r^2\mathbf{X}_{1r}\mathbf{X}_{1l}} \\
&= \frac{ir\mathbf{X}_{2l} + ir\mathbf{X}_{1l}\mathbf{X}_{1r}\mathbf{X}_{2l}}{1+r^2\mathbf{X}_{1r}\mathbf{X}_{1l}}E_2^- + \frac{t^2\sqrt{\mathbf{X}_{2l}}\sqrt{\mathbf{X}_{1r}}\sqrt{\mathbf{X}_{1l}}}{1+r^2\mathbf{X}_{1r}\mathbf{X}_{1l}}E_{in}.
\end{aligned}
\tag{2.110}
$$

Therefore, the light fields at atom position are

$$
\begin{aligned}
E_2^+ &= \frac{\mathbf{X}_{t1}+\mathbf{X}_{r1}\mathbf{X}_{t2}}{1-\mathbf{X}_{r1}\mathbf{X}_{r2}}E_{in} \quad \text{and} \\
E_2^- &= \frac{\mathbf{X}_{t2}+\mathbf{X}_{r2}\mathbf{X}_{t1}}{1-\mathbf{X}_{r1}\mathbf{X}_{r2}}E_{in},
\end{aligned}
\tag{2.111}
$$

with

$$
\begin{aligned}
\mathbf{X}_{t1} &= \frac{t^2\sqrt{\mathbf{X}_1\mathbf{X}_l}}{1+r^2\mathbf{X}_l}, \\
\mathbf{X}_{t2} &= \frac{t^2\sqrt{\mathbf{X}_2\mathbf{X}_r}}{1+r^2\mathbf{X}_r}, \\
\mathbf{X}_{r1} &= \frac{ir\mathbf{X}_1(1+\mathbf{X}_l)}{1+r^2\mathbf{X}_l}, \text{ and} \\
\mathbf{X}_{r1} &= \frac{ir\mathbf{X}_2(1+\mathbf{X}_r)}{1+r^2\mathbf{X}_r}.
\end{aligned}
\tag{2.112}
$$

The phase response parameters of the three-cavity system to gravitational waves can be obtained by substituting Eq. 2.111 into Eq. 2.60,

$$
|\beta| = 2u\frac{F}{\pi}\left(4+\frac{\Omega_h^2}{\omega_p^2}\right). \tag{2.113}
$$

Still according to the same calculation process, the phase response of the AI in L_l arm of the three-cavity system to the signal and noise can be obtained by substituting different transmission matrices into Eq. 2.109

$$
\begin{aligned}
\Delta\theta_{\text{armleft}}(X,t) = \frac{2\omega}{c}\Bigg(& X\frac{h(t)}{2} + \Delta X(t) + (L-X)\frac{\delta f(t)}{f_0} \\
& + \frac{1}{2}\big(\delta x_{2l}(t) + \delta x_{1l}(t) + \delta x_{2r}(t) - \delta x_{1r}(t)\big) \\
& + \frac{1}{\omega_p}\big(\Delta X^{'}(t) + 2(L-X)\frac{\delta f^{'}(t)}{f_0} + \delta x_{2l}^{'}(t) + \delta x_{2r}^{'}(t)\big) \\
& + \frac{1}{\omega_p^2}\big(\Delta X^{''}(t) - 3(L-X)\frac{\delta f^{''}(t)}{f_0}\big)\Bigg),
\end{aligned}
\tag{2.114}
$$

where $\delta x_r = \delta x_{r2} - \delta x_{r1}$, $\delta x_l = \delta x_{l2} - \delta x_{l1}$ are the position noise of right and left resonator mirrors, and δx_m is the mid-cavity mirror position noise. The results for the right arm are

symmetric. The phase response of the AI in L_m is

$$\begin{aligned}\Delta\theta_{\text{mid}}(X,t) = \frac{2\omega L}{c}\Bigg(&\frac{4F}{\pi}\frac{h(t)}{2} + \frac{\Delta X(t)}{L} + \frac{X}{L}\frac{\delta f(t)}{f_0}\\ &+ \frac{2F}{\pi L}\big(\delta x_r(t) - \delta x_l(t)\big)\\ &+ \frac{1}{\omega_p}\big(\frac{2\Delta X^{'}(t)}{L} + \frac{2X}{L}\frac{\delta f^{'}(t)}{f_0} + \frac{2}{L}\delta x_l^{'}(t) - \frac{2}{L}\delta x_r^{'}(t)\big)\\ &+ \frac{1}{\omega_p^2}\big(-2h^{''}(t) + \frac{4X}{L}\frac{\delta f^{''}(t)}{f_0}\big)\Bigg).\end{aligned} \tag{2.115}$$

The corresponding atom phase changes are

$$\begin{aligned}\Delta\Phi_{\text{mid}}(X,t) = \epsilon(X,t) + \frac{2\omega L}{c}\Bigg(&\frac{4F}{\pi}\frac{h(t)}{2} + \frac{\Delta X(t)}{L}\\ &+ \frac{X}{L}\frac{\delta f(t)}{f_0} + \frac{2F}{\pi L}\big(\delta x_r(t) - \delta x_l(t)\big)\\ &+ \frac{1}{\omega_p}\big(\frac{2\Delta X^{'}(t)}{L} + \frac{2X}{L}\frac{\delta f^{'}(t)}{f_0} + \frac{2}{L}\delta x_l^{'}(t) - \frac{2}{L}\delta x_r^{'}(t)\big)\\ &+ \frac{1}{\omega_p^2}\big(-2h^{''}(t) + \frac{4X}{L}\frac{\delta f^{''}(t)}{f_0}\big)\Bigg) \otimes g(t).\end{aligned} \tag{2.116}$$

Compared with a single cavity, the three-cavity system simultaneously amplifies the mirror position noise and signal but does not amplify the atom position noise and frequency noise. Because the phase caused by the GW signal does not change with position, we cannot use a gradiometer to eliminate the position noise of the mirrors. This makes this result closer to an optical interferometer.

So what is the difference between our structure and the OI? In fact, from the calculation of SNR in the first section and the analysis of light intensity, *note that the atom interferometer only measures the phase of light, and its signal to shot noise ratio is not determined by light intensity*. The SNR of the OI is proportional to $\sqrt{P_{\text{in}}}$. Meanwhile the signal to radiation pressure noise ratio of both interferometer are proportional to $\frac{1}{\sqrt{P_{\text{in}}}}$.

For optical interferometers, these two signal-to-noise ratios are simultaneously affected by light intensity. They have opposite effects, resulting in an optimal P_{in} to maximize the sensitivity, this optimal sensitivity $S_h(\omega) = \frac{8\hbar}{M\omega^2L^2}$ is called the standard quantum limit of an optical interferometer.

As for atom interferometers, although shot noise is affected by many factors, such as the atom number and the intensity of the probe light, the intensity of the laser beam in the

cavity is not one of them. So one can decrease the radiation pressure noise by reducing the light intensity in the cavity while keeping the signal to shot noise ratio. This opens a modest window to break through the standard quantum noise limit. As shown in Fig. 2.9, the sensitivities of both AIs and OIs are limited by the QRPN in the low-frequency range. In contrast, in the high-frequency range, they are mainly determined by atom and optical shot noise, respectively. For optical interferometers, shot noise and quantum Radiation noise are both affected by light intensity, which leads to the QSL. Therefore, it can be found that the strain sensitivity of AIs outside the resonator is higher than AIs without a resonator or OI with the resonator.

2.6 Conclusion

We have calculated the optical phase difference inside and outside of an optical resonator; due to a factor $\frac{F}{\pi}$, the phase difference outside the resonator nets a higher strain sensitivity to GW signals. To this end, we propose an atom interferometry experiment utilizing the output light of a resonant cavity as the interrogation frequency. Compared with the atom interferometer in free space or inside the resonant cavity, this structure improves the signal to shot noise ratio, lower the atom position noise, but increases the trouble of mirror position noise.

With atom interferometer, we can lower the radiation pressure noise by reducing the light intensity in the low-frequency range while maintaining the signal to shot noise ratio to break through the standard shot noise limit compared to an optical interferometer with the same parameters. This new design philosophy could function as an addition to existing atom/optical interferometrys [27, 65].

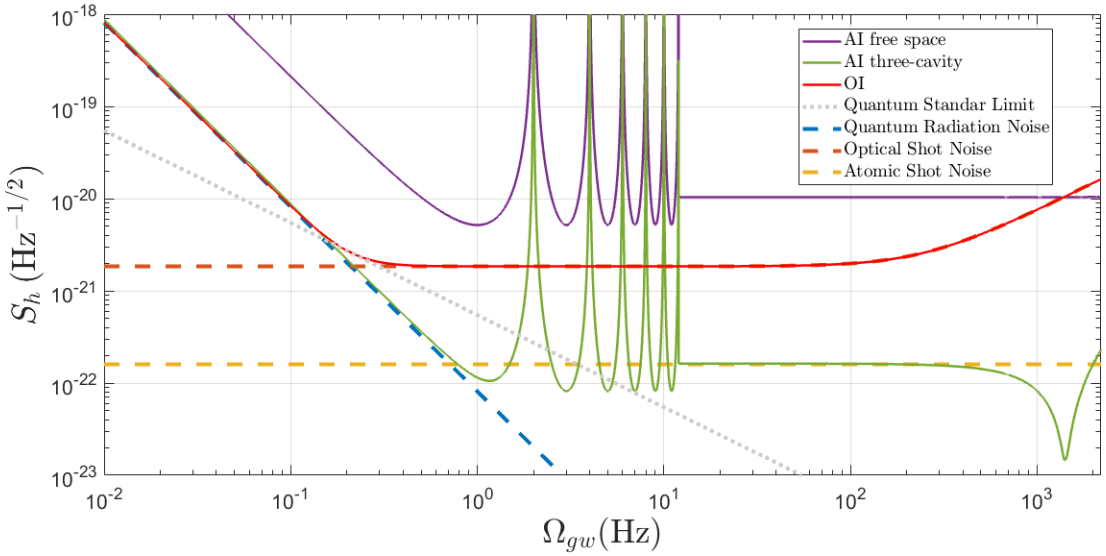

Figure 2.9: The sensitivity functions of optical interferometer and atom interferometer, equivalent strain to the quantum shot noise and quantum radiation noise, with parameters $L = 3000$ m, $F = 100$, and $P_{in} = 100$ mW, atomic flow $n = 1 \times 10^{12}$/s, and $N = 1000$ LMT beam splitters. Due to the inclusion of Eq. 2.36 in the atom interferometer's strain sensitivity, there will be periodic peaks, so the average value over the period for AI stain is shown above 12 Hz.

Chapter 3

Experimental apparatus

One of the main tasks of my thesis was to construct of the 6.35 m atomic gradiometer. In this chapter, we will describe the composition of the entire experiment in terms of different subsystems.

First, in Sec. 3.1, we show the design of the experiment and vibration isolation platform where all the experimental equipment is located. Precision measurement experiments require an equally precise control system, and how to achieve synchronization between systems is the question we answer from both software and hardware aspect in Sec. 3.2. Ultra high vacuum (UHV) is critical for this experiment, due to long flight time. In Sec. 3.3, we introduce how we obtained 10^{-10} mbar vacuum. Sec. 3.4 describes the integrated laser system provided by μQuan, which is used to provide all of the cooling, repump, and Raman optical sources required by the atom source. In addition to the laser system, we use a separate Bragg laser that forms the standing wave optical lattice for diffraction inside the vacuum chamber. Sec. 3.5 introduces the optical path of the Bragg light and how to obtain a wider light diameter through a stable cavity.

Contents

3.1 Design

3.1.1 Experiment design

The experimental design of the prototype atom gradiometer is shown in Figure 3.1. There are two optical chambers on both sides of the main vacuum chamber. We label the optical chamber closer to the north as "right" and the other one closer to south as "left", and each optical chamber has two CF 200 flanges and four CF100 flanges (See appendix for design drawing). Both ends of the entire vacuum chamber are sealed by two CF500 blank flanges with spring energized metal seal (Technetics HELICOFLEX HNV200 aluminum A5).

The "right" optical chamber is connected to a residual gas analyzer, vacuum gauges, venting valve, ion/getter pump, and a RS232 feed-through port for controlling a UHV mirror mount with piezoelectric adjusters. The left one is connected to the turbopump, ion/getter pump, an optical window for injection of the Bragg beam, and a similar RS232 port.

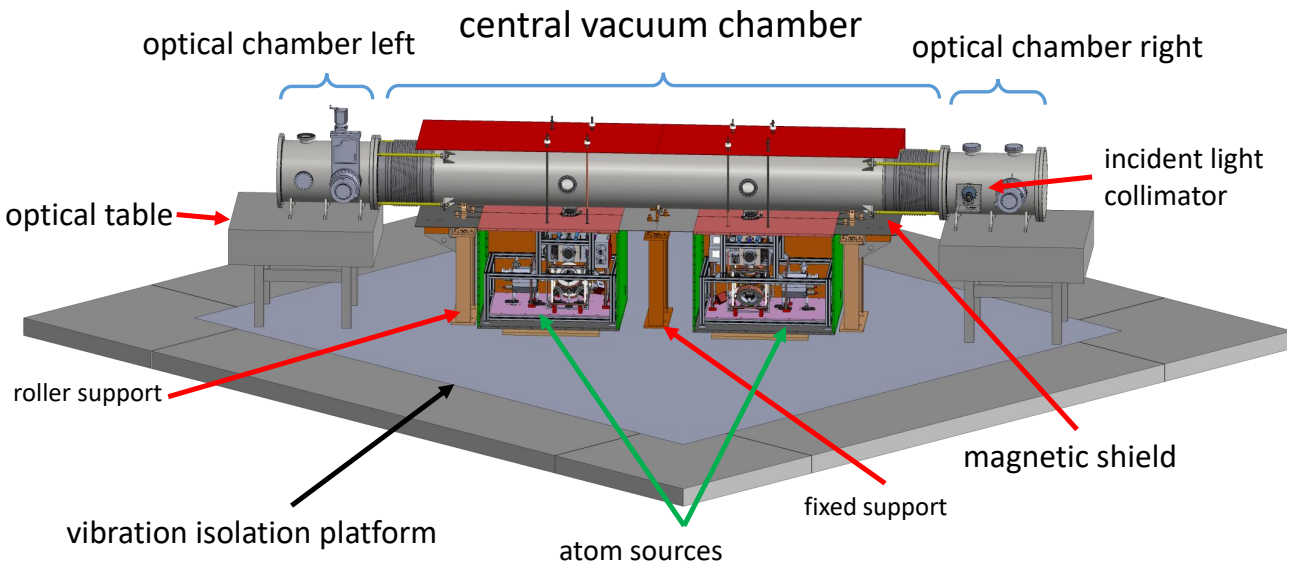

Figure 3.1: Design of atom gradiometer experiment

Inside the optical chamber, there is a UHV compatible optical breadboard for placing the mirrors that form the optical lattice. Each mirror mount has two piezoelectric adjusters and connects to a controller (New Focus, Motion Controller, Open-Loop, 4 Channel) outside the vacuum through the vacuum safe RS232 connection, allowing the optical path's alignment. The controller is controlled via PC software or a handheld joystick.

In the center is the central vacuum chamber supported by three supporting structures; the middle one is fixed support. Such a long vacuum chamber will thermally expand during baking, so there are bellows at both ends of the vacuum chamber, and the supports on both sides are connected to the vacuum chamber by rollers instead of screws. These designs ensure a specific space along the axial direction to prevent the deformation from damaging the vacuum chamber or the connected components. The two atom sources are provided by our collaborative research unit, Systèmes de Référence Temps-Espace, Observatoire de Paris (SYRTE), and they have carried out some tests to ensure the performance of the atomic source[66], the Laser systems for these two atom sources are provided by Muquans[67]. The distance between atom sources is 1.5m. They are both connect to the central vacuum chamber via

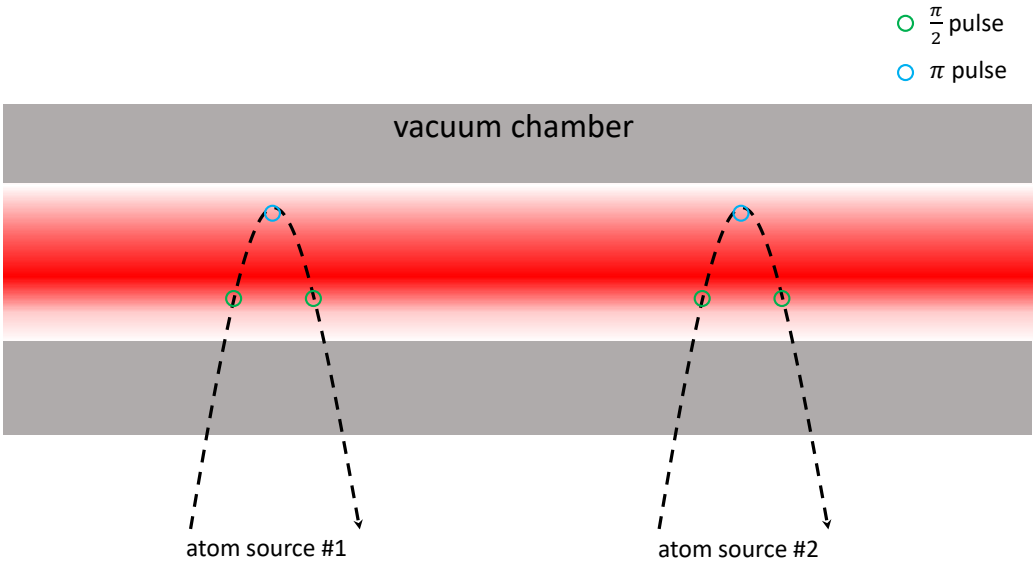

Figure 3.2: First step protocol for atom gradiometer, the three Bragg scattering pulses are realized by a single light beam

a gate valve (PFEIFFER GVMP-S11542), which allows the atom head to be transported and attached while maintaining an internal vacuum.

The main vacuum chamber and the atom head will both be wrapped in a magnetic shield to avoid the influence of the surrounding magnetic field. In the MIGA project introduced earlier, two beams of lattice light are used to diffract atoms. While in this prototype, we use one beam with a larger diameter instead of two beams to form the three light pulses. Doing so will limit our pulse interval T, but reduce the optical components, we do not need to use two mirrors to get two Bragg beams as [3]. According to the analysis of Sec. 2.3.3, although the gradiometer can remove the effects of first-order mirror position noise, using two mirrors will lead to a more significant second-order position and angle noise than one mirror.

Due to the limitation of the mirror size, the maximum available beam width is $w = 50$ mm, and the corresponding interval between pulses is

$$T < \sqrt{\frac{2w}{g}} = 0.1 \text{ s}. \tag{3.1}$$

This interval may be smaller considering the radial intensity distribution of the laser beam, so we have a peak sensitivity at $f = 20$ Hz.

3.1.2 Vibration isolation platform

There is a complicated and multifaceted source of noise in our experimental environment: seismic noise, which arises from the vibration of the ground by various factors, such as geological activity or nearby traffic. According to the analysis of noise in Sec. 2.4, seismic noise will affect the position noise of the mirror and gravitational gradient along the laser beam direction, which in turn affects the measurement results. Therefore, the whole gradiometer experiment is placed on a multi-ton concrete vibration isolation platform supported by multiple active vibration isolation supports (filled with air at a pressure of 7 bar). We hope to use this platform to reduce vibration noise in the detection frequency range. However, the vibration isolation platform does not just "erase" the vibration power but transfers the noise power in one frequency range to other frequencies. Therefore, only by confirming that the noise in the frequency range measured by the experiment is compressed can the vibration isolation platform be proved effective.

A test of the vibration was taken (Fig. 3.3) by TMC Corporation when no experimental equipment was placed on the platform. The test tool is Wilcoxon Research 731A accelerometers with external Amplifiers P31, FFT Spectrum analysis performed with Data Physics Quattro DP240 with SignalCalc 240V, 2-Channel 32 bit floating-point DSPs with up to 204.8 kHz sample rate. Inputs are coupled to dedicated 24 bit sigma-delta ADCs while both outputs have 24 bit DACs. Integral anti-aliasing filters protect the inputs and outputs. 120 dB dynamic range with up to 94 kHz real-time. the result shows a large 10-times resonance amplification of the air system at 2.5 Hz. For frequencies of around 10 Hz and higher the air isolation performs as expected.

After installing the experimental equipment, we carried out the second test. The measurement locations were: the center of the vibration isolation platform without inflation, the center of the inflated vibration isolation platform, and the optical table after the vibration isolation platform was inflated. The acceleration is measured along the axial direction of the vacuum chamber. The test tool is Wilcoxon Research 731A accelerometers with external Amplifiers P31, Signal acquisition with redpitaya, 16bit DAC, sampling frequency 500 Hz. The total weight of the vacuum chamber, optical table, atom head and other instruments is about

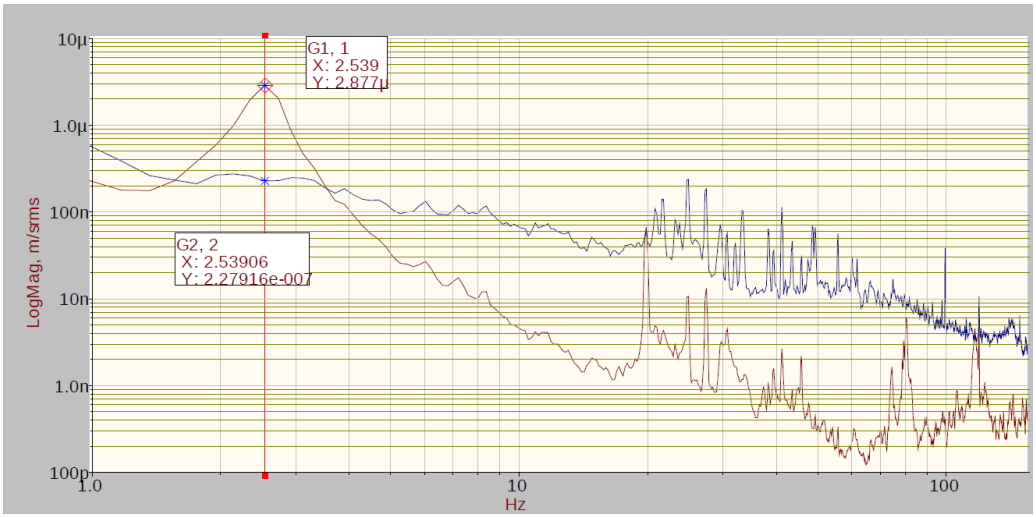

Figure 3.3: The vibration frequency test report provided by TMC.

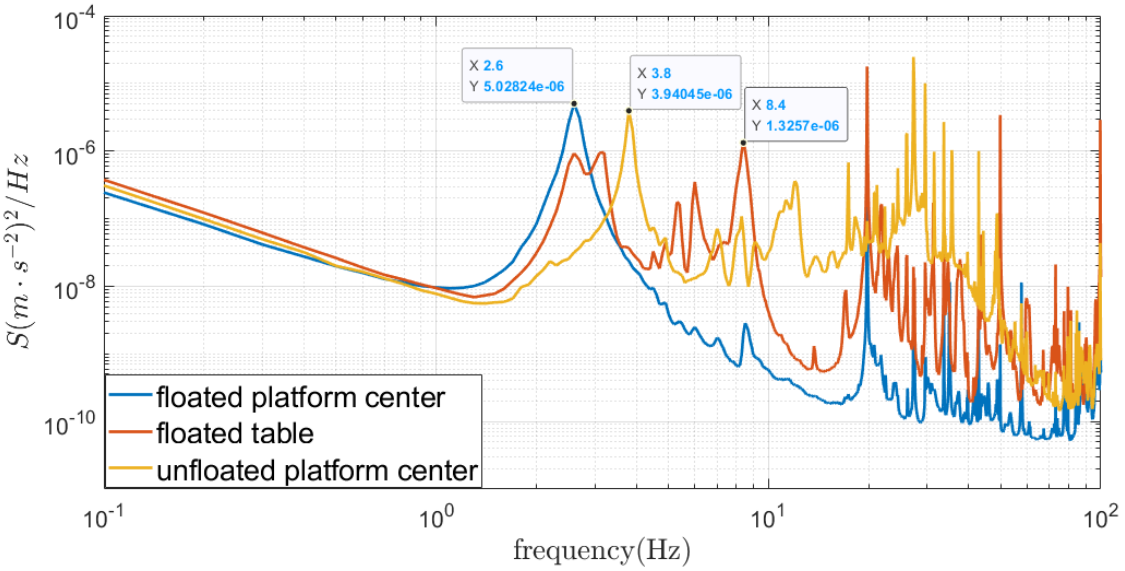

Figure 3.4: The vibration test with all equipments settled on the vibration isolation platform. The narrow peaks in the frequency range above 20 Hz mainly come from electronic noise of the measurement circuit.

5000 kg. This test is consistent with the first test. The vibration isolation platform effectively reduces the vibration acceleration noise above 4 Hz, and resonance occurs at 2.6 Hz; the inflated vibration isolation platform has a resonance peak at 3.8 Hz; For the marble optical platform, it resonant frequency appears at 8.4 Hz, due to the passive legs, hard surface and the vacuum tube.

According to Eq. 2.35, the sensitivity function of the atomic interferometer with $T = 0.1s$ can be calculated, combined with this test result $S_v(\omega)$, the phase noise in both cases is:

$$\begin{aligned} \Delta\Phi &= n\Delta\phi(t) \otimes s^{'}(t) \\ \Rightarrow S_{\Delta\Phi}(\omega) &= |\beta|_v^2 \, |H(\omega)|^2 S_v(\omega) \end{aligned} \tag{3.2}$$

The power density of inflated and non-inflated vibration isolation platforms ratio at 20 Hz is

$$\frac{S_{\Delta\Phi}^{inflated}(20 \times 2\pi)}{S_{\Delta\Phi}^{non}(20 \times 2\pi)} = 0.0045 = -23.4679 \text{ dB} \tag{3.3}$$

The total power ratio from 0.1 Hz to 20 Hz is

$$\frac{\int_{0.2\pi}^{40\pi} S_{\Delta\Phi}^{inflated}(\omega) d\omega}{\int_{0.2\pi}^{40\pi} S_{\Delta\Phi}^{non}(\omega) d\omega} = 0.2626 = -5.80705 \text{ dB} \tag{3.4}$$

3.2 Control system

Fig. 3.5 is the diagram of our experimental control process. A PC generates control sequences [68] for instruments (laser system [69], magnetic coils circuits, power supplies) and collects detection data through the control box. All hardware and software code described in this section can be found in the linked file at [68].

3.2.1 Software

The software flow of the control program is shown in the Fig. 3.6 We call each control command "instruction" and a series of instructions a "program." We write each program as a control sequence file in the format of "$.mot$", which is loaded and executed by the program "$gmot$."

$gmot$ is the experimental control main program written in C, including the test mode of sending an instruction separately and the running mode of executing the program. Con-

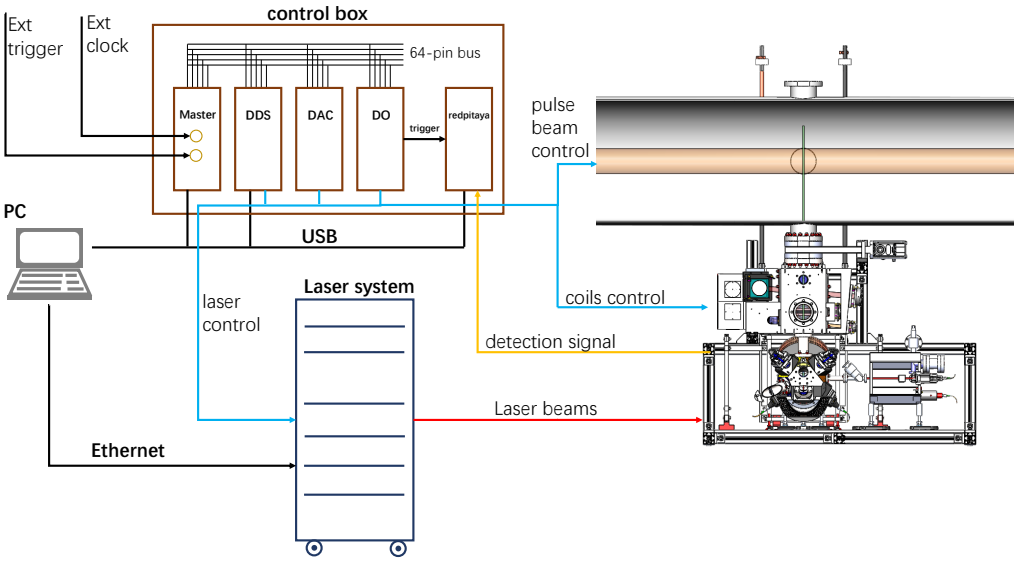

Figure 3.5: Schematic diagram of experimental control flow. The blue line in the figure is the control signal output, the yellow line represent the collected detection signal, and the red line is the laser output.

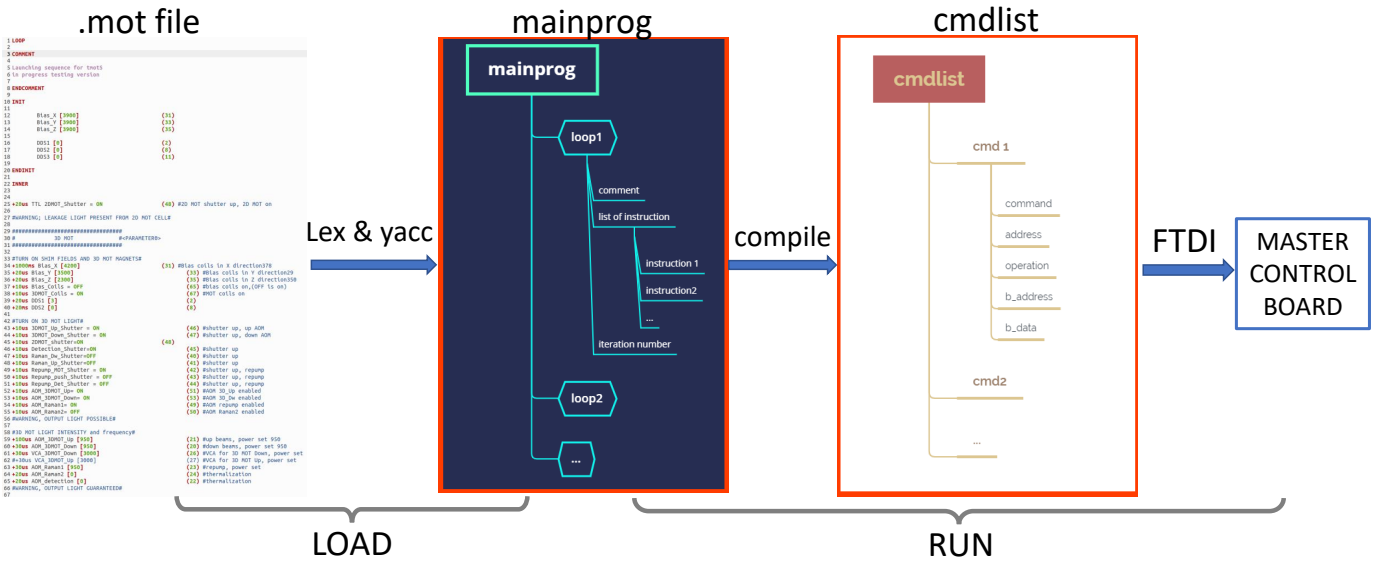

Figure 3.6: The *gmot* program converts the *.mot* file into a control sequence and writes it to the master control module for running.

trol addresses and command parameter reads for each port are placed in $Function.c$ and $Function.h$.

In order to make the sequence file concise and easy to understand, we use the combination of lex+yacc [70, 71]. First, the control program will be written to the .mot file in the form of "time + control command + control port," and indicate the number of loop execution times of the program. Lex generates a "lexer," a function that takes a character stream as an input parameter and matches a keyword (key) when it sees a set of characters. The lexical analyzer function will translate the $.mot$ file into a keyword stream according to the pre-specified rules and input it to YACC. YACC can parse the identifier (token) in the input stream, convert all commands into the structure prog we defined (the conversion rule is in the $parser.y$ file, and the structure is defined in $TYPE.h$), and store it in the mainprog, during the running process Then convert it into $cmdlist$, and write it into RAM through $ftdi\_write$ and execute it.

3.2.2 Hardware

As the core of the control system, the control box consists of a power supply, a bus back panel and various boards.

The boards include:

1. Master Control Module (MCM);
2. Digital Output boards (DO);
3. Digital to Analog Converter boards (DAC);
4. Direct Digital Synthesizer boards (DDS);
5. Signal acquisition boards (redpitaya).

3.2.2.1 Master board

The master control board (MC) is for receiving instructions from PC (EZ-USB to FPGA) and sent out through the write-only parallel bus in the control rack. The bus line has 64 pins, of which 4 pins are $\pm$ 15 V power supply, 2 pins are +5 V for conversion +3.3 V TTL reference power supply 14 pins are grounded; currently, we use 8-pin as the address bit and 16-pin as the data bit.

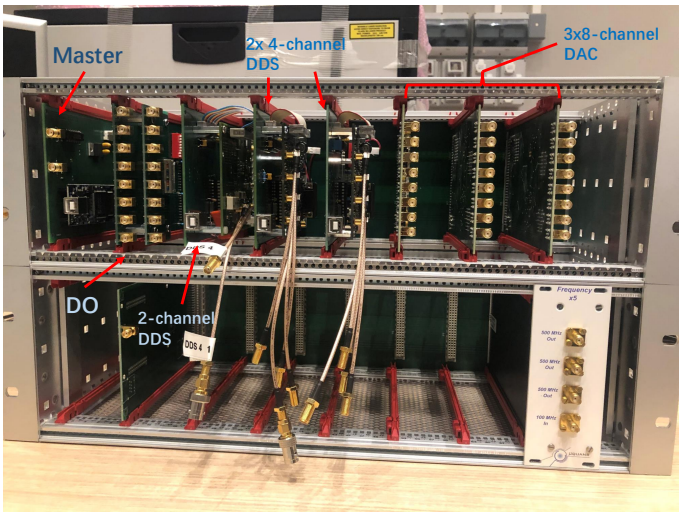

Figure 3.7: A picture of the control rack, the power supply module in the back converts 240VAC into the ± 15 V power required by the boards and +7 V used to generate the reference level [68]. Each slot can be inserted into a board, and the upper board is in turn: master board, 16-channel digital output board, 2-channel DDS board, 2× 4-channel DDS board, 3× 8-channel boards, the lower empty slot is for the data acquisition board redpitaya. The 100 MHz-500 MHz multiplier at the bottom left is used to generate the synchronization clock for the master board

The master board consists of FPGA, 64M DDR RAM, and EEPROM. The EEPROM contains the FPGA structure code, and RAM stores the instruction sequence of the experiment, the maximum capacity of which is 8M.

Each board is identified by a GFIB address, which can be set by an 8-digit DIP switch. The GFIB address corresponds to the 8-pin address bit on the bus. The board will accept the instruction only when the address of the command issued on the bus matches its GFIB address. The master control can use the onboard 24 MHz quartz or external clock signal. It will obtain the operating frequency of 10 MHz after frequency division, so the equivalent step length is 100 ns.

There are also two trigger modes for MC, internal or external. For the test of a single atom interferometer, internal clock and internal trigger are sufficient. When multiple atomic sources are used to obtain the gradiometer signal, an external trigger is required to synchronize the signals of each atomic interferometer. Using two different PCs to connect the two control systems with the same sequence, we find a time difference of 700 ns/ms at the control output signal. This time difference comes from the the internal clock frequencies of the two

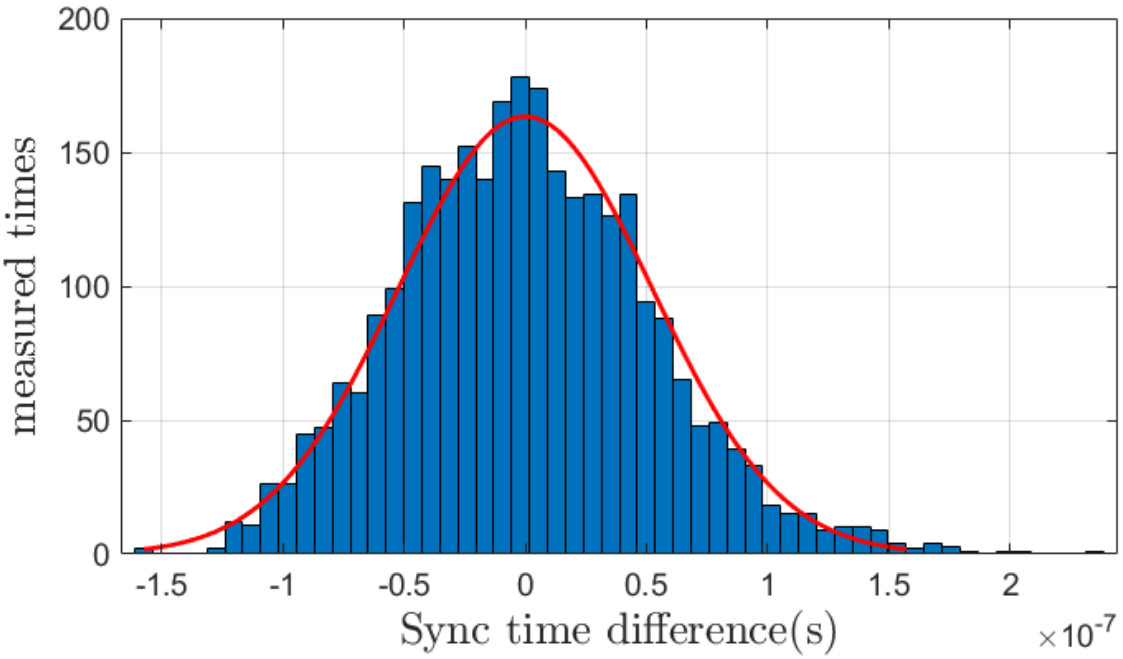

Figure 3.8: Histogram of signal synchronization of two control systems over 3000 measurements. The measurement tool is an oscilloscope with a resolution of 5ns, and the two control boxes use the same trigger signal and sequence.

MCMs. After calibrating the time difference of 700 ns/ms in the program, we measured the synchronization of the two control systems. The measurement results are shown in Fig. 3.8, the number of measurements is 3000 times and $\delta = 65.7$ ns for Gaussian distribution fitting

3.2.2.2 DO and DAC

The digital-analog board (DAC) has eight 16-bit analog output channels, providing an output range of $3 \times V_r$, where V_r is the external reference voltage. We take $V_r = 5$ V in our experiment, and the corresponding output range is ± 15 V. When inputting the control command, it use hexadecimal complement to represent the voltage value, that is to say, 0x0000-0x8000 represents $0 - +3V_r$, 0x8001-0xffff represents $-3V_r - 0$, and its resolution is $30/(2^{16}) \approx 0.0005$ V.

Each output of the 8-channel DAC board occupies a GFIB address, and the 8-digit DIP switch on the board indicates the address of its channel-0, and the other port addresses increase by one. Because of the need for calculation time, each A minimum of 100ns interval

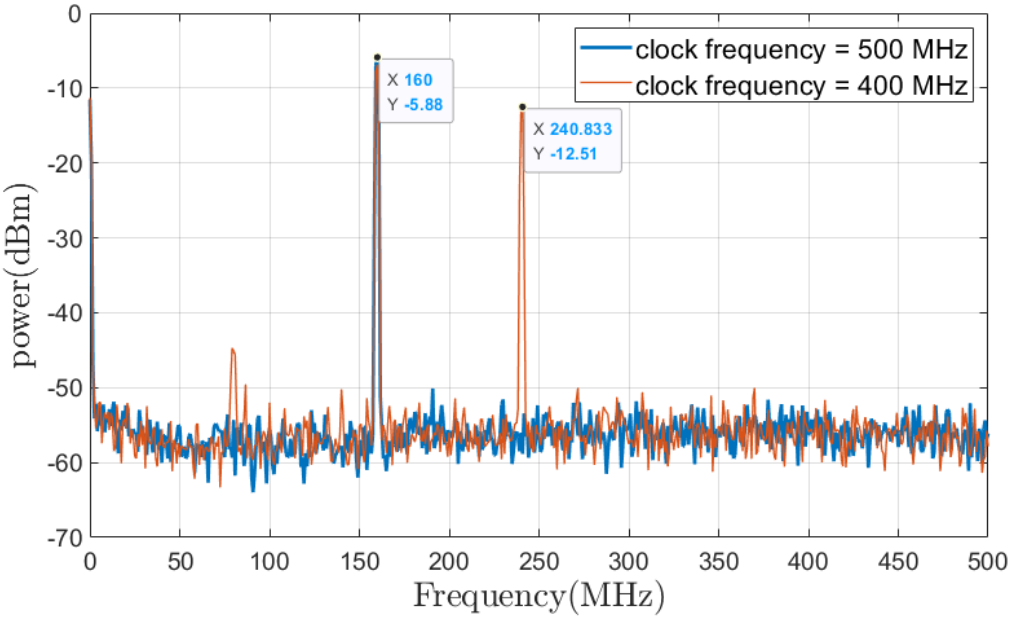

Figure 3.9: The frequency spectrum of the DDS board's 160 MHz signal output with different clock frequencies. There is an sideband at 240 MHz for output with 400 MHz clock.

is required between DAC control commands.

3.2.2.3 DDS

The DDS module is used to output frequency signals for laser frequency locking and AOM control. There are two types of DDS modules, the 2-channel one based on the AD9958 evaluation board and the 4-channel one based on the AD9959 evaluation board. Both modules have multiple functions, including signal amplitude, frequency, phase control and ramp. At present, we have only developed the corresponding hardware and ramp control function for AD9958, while the AD9959 uses commercial supporting hardware and cannot use the ramp function.

The output state of the DDS module is written through USB and stored in RAM. This process is too slow during the experiment considering the transmission speed of the USB connection, so it is necessary to use "$writetable$" to write the DDS table containing all output states into the RAM before the experiment. The DDS table contains up to 512 output states. The information of each output state is composed of frequency, amplitude, phase, ramp sta-

tus. Then control commands can be sent through the bus to specify which state the DDS board should output. When there is a problem with the module, such as no output or the output state cannot be changed, one can use "$resettable$" to reset the USB connection to the board.

It is worth noting that there is a set clock frequency both for the CPLD firmware and microcontroller firmware of the DDS board, which can be set to multiples of 50 MHz, but it must be consistent; otherwise, the output frequency and specified frequency will mismatch. Also, different clock frequencies may have different output effects (see Fig. 3.9).

3.2.2.4 Redpitaya

For data collection, a commercial version of the open-source platform called "redpitaya" is used as a data acquisition board [72].

The module photo and structure diagram of redpitaya in the control system are shown in Fig. 3.10; As a commercial module, redpitaya can be used alone, but in order to integrate it into our control box, we designed the base-board as in Fig. 3.10(a), using the 64-pin bus line to power redpitaya. In addition, there is an SMA input on the base-board which is connected to the 16 single-ended digital I/O (E1 in Fig. 3.10(b)), providing triggers for signal acquisition.

There are four SMA interfaces on the redpitaya board, two of which are for analog signal input, and the other two are for analog signal output. Both are equipped with a 50 Mhz low-pass filter. There are two ranges for input channels: $\pm$ 1 V and $\pm$ 20 V, the sample rate of which is 125 Mbps.The board converts the input analog signal into a 14 bit digital signal, meaning that different input ranges correspond to different resolutions ($1.22 \times 10^{-}4$ V for $\pm$ 1 V and $24.4 \times 10^{-}4$ V for $\pm$ 20 V). In order to get a better resolution, we designed a circuit that can adjust the bias and amplification factor of the signal so that the peak-to-peak value of the signal is close to the input range of the redpitaya (see AppendixB for the circuit diagram).

Communication with the redpitaya is performed over Ethernet connection. The Linux system is embedded in redpitaya, which can be accessed using ssh to upload programs. During experimental data acquisition, the waveforms of the two input channels will be recorded for each trigger and transmitted to the PC through HTTP server for data analysis. In addition

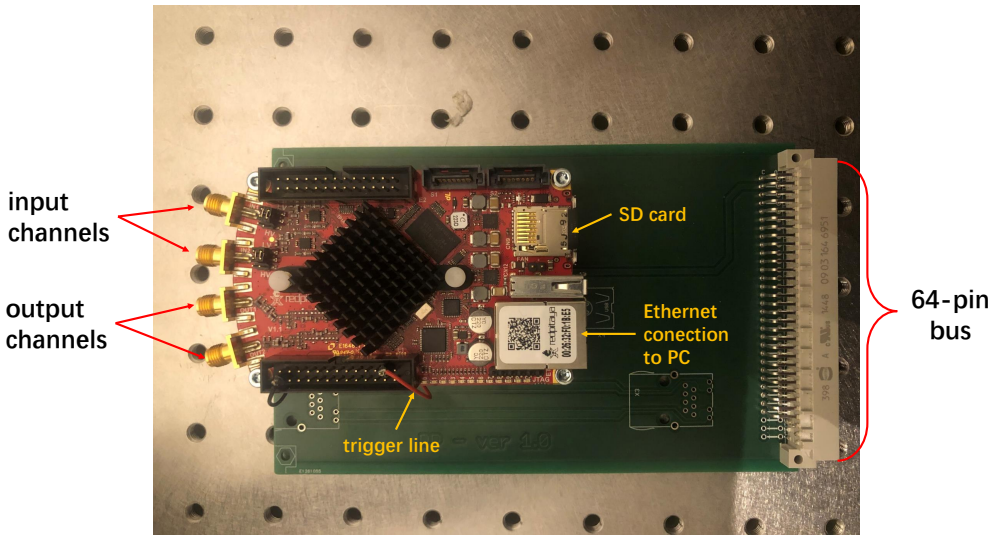

Figure 3.10: The redpitaya with baseboard to fit in the control rack, the upper layer is the commercial redpitaya, the lower layer is the baseboard which provides the power supply and trigger interface of the redpitaya.

to SSH, it can also be accessed through LAN, and a web program is provided in redpitaya, which allows us to use redpitaya for multiple purposes.

3.3 Vacuum

In the definition of physics, a vacuum is a state of space without any matter. However, in practice, this state cannot be obtained in absolute. So in engineering, we define a vacuum as the pressure of a gas in a given space. In precision measurement experiments, because the movement of gas molecules in the air will affect the measurement result, so in the following part will the vacuum level required to achieve the sensitivity we need.

3.3.1 Calculation

Obtaining a vacuum in an experiment starts with knowing what degree of vacuum is required and how to generate it. This section is about the computation of these problems. The effects of residual gas [73] on the AI experiment are:

(1) It directly interacts with the laser to affect the phase of the laser [74]; the PSD of the

optical length change caused by the residual gas is

$$S_{\Delta L}(f) = \frac{4\rho(2\pi\alpha)^2}{v_0}\int_0^{L_0}\frac{e^{-2\pi f\omega(z)/v_0}}{\omega(z)}dz \tag{3.5}$$

where L_0 is the arm length, ρ is the gas density, α polarizability, $\omega(z)$ the beam's Gaussian radius parameter, v_0 is the most probable speed of the gas. On the basis of kinetic theory of gases, the most probable speed of the gas is

$$v_0 = \sqrt{\frac{3k_BT}{m}}, \tag{3.6}$$

where m is the average mass of residual gas.

(2) It collides with the atoms, which will reduce the number of atoms and hence the SNR;

(3) Molecules attached to the mirror surface reduce the local reflectivity of the mirror surface, causing the mirror surface to absorb more laser energy, thereby damaging the mirror surface;

(4) Impact of gas molecules on mirror surface will generate mirror position noise [75]:

$$S_F = S_F^{\infty} + \Delta S_F(f), \tag{3.7}$$

S_F^{∞} is the noise spectrum of mirror in a infinite volume, and $\Delta S_F(f)$ comes from the collision of residual gas between the mirror and the surrounding environment.

$$S_F^{\infty} = p\sqrt{128\pi m k_B T}R^2\left(1+\frac{h}{2R}+\frac{\pi}{4}\right) \tag{3.8}$$

where p is the pressure, k_B is the Boltzmann constant, h,R are the thickness and radius of the mirror. According to the equation of ideal gas state

$$p\cdot V = Nk_BT \tag{3.9}$$

with N the atom number. In the frequency range we detect, $\Delta S_F(f)$ basically does not change with frequency, so

$$\Delta S_F \approx \frac{4}{\pi}p\sqrt{8\pi m k_B T}\pi R\frac{R}{d^2\ln\left[1+(\frac{R}{d})^2\right]} \tag{3.10}$$

where d is the distance between mirror and the surrounding objects.

According to the above conditions, in order to get a strain sensitivity of 10^{-22}, the pressure in the vacuum chamber should reach 10^{-9} mbar, which is generally called ultra-high vacuum (UHV). The next step is to consider how to obtain such a vacuum [76].

Obtaining vacuum at any qualify requires the vacuum pump, which is mainly divided into

two types according to the principle: gas tranfer pump and gas adsorption/capture pump, and each of them has many subdivisions according to the mode of action and material. Generally, the pumped target is air, composed of various gas molecules. The main components of air are [77] hydrogen, nitrogen, water vapor, and carbon dioxide. Different pumps have different pumping efficiency of different gases, so in the experiment, We use both pumps (turbopump and ion/getter pump) to pump the vacuum chamber and atomic head. Meanwhile, the residual gas analyzers are applied to monitor the partial pressures of different components.

The pumping capacity of a gas transfer pump is manifested in several parameters, including base pressure, pumping speed, and compression ratio. Pumping speed is defined as

$$S_0 = \frac{dV}{dt}, \tag{3.11}$$

the gas flow q on both sides of the pump meets the condition:

$$q_{pV} = S \cdot p. \tag{3.12}$$

The compression ratio is defined as

$$K_0 = \frac{p_v}{p_a} \tag{3.13}$$

where p_v is the backing pump pressure and p_a is the inlet pressure. The pumping process conforms to the formula

$$t = \frac{V}{S} ln \frac{p_{in}}{p_{out}}, \tag{3.14}$$

where p_{in} and p_{out} are the pressure inside and outside the vacuum chamber, and S is the equivalent pumping speed. The equivalent pumping speed is determined by the pumping speed of the pump group, the backflow, and the conductance. Among them, conductance is proportional to the length of the connecting tube. Since our turbopump is directly connected to the vacuum chamber, the pressure loss caused by conductance is negligible.

The base pressure refers to the lowest pressure achievable within a specified time when the vacuum pump is sealed with a blank flange. During this process, only the backflow airflow is drawn out. Therefore, combined with the pumping speed and the compression rate, the backflow airflow conductance of the pump can be inferred. Of course, it is difficult to achieve the base pressure in the actual experiment, but the vacuum pump needs to be

selected according to the required pumping time and target pressure. Generally speaking, the base pressure of the vacuum pump should be an order of magnitude lower than the target pressure. Besides backflow losses, other causes affecting vacuum gas flow are desorption from the inner wall, permeation, and leakage.

3.3.1.1 Desorption

Gas molecules, mainly water molecules, will be adsorbed on the inner wall of the cavity under ambient pressure and will be gradually released as the pressure in the vacuum chamber decreases, and the rate of release will gradually decrease over time. We assume that the release rate will show a linear decrease after one hour. After one hour, its leak rate can be expressed as:

$$Q_{des} = q_{des} A_d \frac{t_0}{t} \tag{3.15}$$

where q_{des} is the Permeation constant, A_d is the interior surfaces area, t is desorption time.

3.3.1.2 Permeation

There will be a gas penetration effect no matter what seals and materials are used. This process is not affected by time but only depends on the material itself and the pressure it bears. The corresponding diffusion rate is

$$Q_{perm} = k_{perm}\, A \frac{p_a}{d} \tag{3.16}$$

where k_{perm} is the area-specific flow density, A is the surface of chamber, p_a is pressure outside the chamber, and d is the wall thickness.

3.3.1.3 Leakage

Many reasons can cause leakages, such as welding or glue pores, cracks caused by material stress, thermal stress, and flange connections. The leak rate is defined as:

$$Q_L = \frac{\Delta p\, V}{\Delta t} \tag{3.17}$$

the pressure p_l of the vacuum chamber is the balance between effective pumping speed S and permeation Q_{perm}, leak rate Q_L, as well as gases released from the metal surface $Q_{des,M}$,

$$p_l = \frac{Q_{perm} + Q_{des,M} + Q_L}{S}. \tag{3.18}$$

Combined with the above analysis, the methods that can increase the minimum pressure that the vacuum chamber can obtain are as follows:

(1) Use a vacuum pump with a higher pumping speed and compression ratio,

(2) Optimize component design to reduce internal surface area and increase the wall thickness,

(3) Use gasket and flange connections with better sealing to avoid leakage at the interface,

(4) Bake the vacuum chamber and the devices inside to reduce water vapor.

3.3.1.4 Conductance

When the container and the pump are connected by piping, the friction between the gas and the pipe wall and the internal friction of the gas will cause the loss of pressure/pumping speed, which is called flow resistance W, but it is generally expressed by its reciprocal conductance C,

$$C = \frac{l}{W} = \frac{q_{pV}}{\Delta p}. \tag{3.19}$$

When the pressure range is 1000-1 mbar, the gas mainly behaves as laminar or turbulent flow. At this time, the conductance of piping at 20 °C is

$$C_{lam} = 1.35 \cdot \frac{d^4}{l} \cdot p. \tag{3.20}$$

As the pressure goes below 10^{-3} mbar, the gas's behavior transfers to molecular flow, so the conductance of piping is constantly based on the geometry, and is no longer a function of pressure:

$$C_{mol} = 12.1 \cdot \frac{d^3}{l} \quad \text{at} \quad 20°\text{C}. \tag{3.21}$$

3.3.2 Vacuum generation

The vacuum chamber for our gradiometer experiment is co-designed and manufactured by SAES, see appendix for its drawings. Some data of it: the length of the vacuum chamber

is $L = 6.35$ m and the inside radius is $r = 0.25$ m, the wall thickness is $d = 5$ mm, the volume of chamber is

$$V = \pi r^2 L = 1.25\ m^3 \tag{3.22}$$

and the inner surface is

$$A = 2\pi r\ L + 2\pi r^2 = 10.36\ m^2 \tag{3.23}$$

3.3.2.1 Measurement

The prerequisite for obtaining a vacuum is measuring the pressure in the vacuum chamber. There are different measurement tools for different pressures. The more common ones are active gauges, which integrate different transducers and power supply circuits, with a wide measurement range and simple control, but we chose the combination of the ConvecTorr gauge and IMG-300 UHV Inverted Magnetron Gauge for pressure measurement instead of active gauges. The reason is that we need to bake the entire vacuum chamber, even if the gauge will not be directly backed; when the main chamber reaches 100°C, the surrounding transducers will also reach 50-80 °C due to the heat conduction of the vacuum chamber wall. Therefore, the transducers and circuit parts should be kept separate.

The ConvecTorr gauge is a thermocouple gauge, usually used to measure low vacuum. Inside the thermocouple gauge, the filament is heated by a constant current. Gas molecules take away heat when they impact the filament. Therefore the temperature directly depends on the pressure in the chamber. The higher the pressure, the more molecules will interact with the filament and absorb more heat. The pressure data is obtained by measuring temperature changes of the filament with thermocouples or the filament's resistance.

The inverted magnetron gauge (IMG) uses an electromagnetic field to generate plasma in a hollow stainless steel cylinder [78]. The electromagnetic field accelerates the collision of electrons with neutral gases, causing the molecules to produce positive ions. The cathode absorbs positive ions, and the current generated is proportional to the gas density and pressure. Compared with other UHV measure methods, an IMG is more robust and has a longer lifespan.

The pressure measurement range of the ConverTorr gauge is from the atmosphere to 10^{-4}

mbar, while the IMG is $10^{-3} - 10^{-11}$ mbar; the two transducers can cover the pressure from atmospheric pressure to the experimental target pressure range. We placed a set of gauges in each optical chamber; the XGS-600 gauge controller is used to power all four gauges and get the data. Unfortunately, XGS-600 only has a simple graphical interface for displaying the current pressure value. In order to make this up, we write a LabVIEW program to draw the pressure curve and store the data.

We also used the residual gas analyzer (RGA) as a measurement tool for ultra-high vacuum (Fig. 3.19). RGA is a mass spectrometer with a small physical size that can be directly connected to the vacuum system, and its function is to analyze the gas in the vacuum chamber [79]. All RGA instruments work on the same principle: gas molecules are ionized, and the resulting ions are separated, detected, and measured based on their molecular mass. Using RGA, we can see the composition of the residual gas, and based on this, we can take different steps to increase the vacuum further, and RGA can also be used for leak detection.

3.3.2.2 Pumping group

The root pump of our pump group is Turbo-V 1001 Navigator Pump [80], with pumping speed 920 l/s (H_2), compression ratio 1×10^6 and base pressure 10^{-10} mbar; the backing pump is Agilent IDP-15 Dry Scroll Vacuum Pump with pumping speed 4.3 l/s.

The pump group is connected to the vacuum chamber through the gate valve (PFEIFFER GVMP-S11542). After using the pump group to pump down the pressure in the vacuum chamber, we can use the circuit (see Fig. B.1) to close the gate valve, then the pump group, after which the vacuum pressure of the chamber can be maintained only by the ion/getter pump.

The pumps are connected by corrugated hose, the length of which is 1 m, the inner diameter is 50 mm. Since its pressure range is between continuous flow and molecular flow, its conductance is between 8.5 l/s and 15 l/s according to Eq. 3.20 and Eq. 3.21.

According to the data of the turbopump, it reaches the max pumping speed when the pressure is lower than 10^{-2} mbar, which is close to the backing pump's base pressure. Without considering outgassing, after $t = \frac{1250}{4.3} ln \frac{1000}{0.01} = 0.93$h the pressure reaches to 1.5×10^{-2} mbar, while according to Fig. 3.11(b), the pressure in the vacuum chamber reached 1.5×10^{-1} mbar

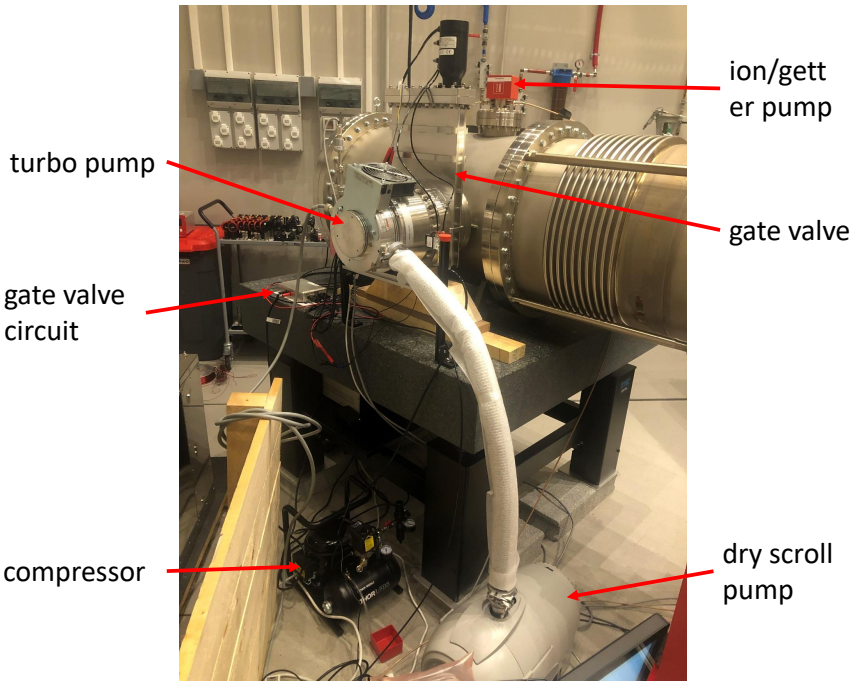

a

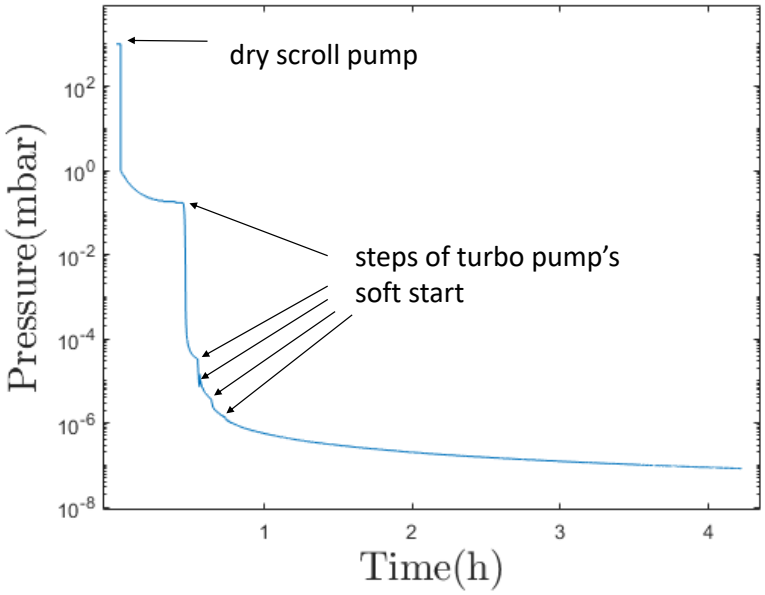

b

Figure 3.11: pump groups and the pressure changes when they start. (a) The pump group is connected to the optical tower at one end through the gate valve (b) The pressure measured during the pump start-up phase; the pumped space is the optical tower that is not connected to the vacuum chamber.

within half an hour, and then we turned on the turbopump. In addition, to further improve the vacuum, we added a NEXTorr D 100-5 and a NEXTorr D2000-10 ion/getter pump. The pump speed of its NEG section to H_2 is 100 l/s and 2000 l/s respectively. The getter pump [81, 82] absorbs gas with the disk-shaped getter alloys supported by a metal rod. A heating element is inserted inside the disks to activate the proper getter. After the getter is exposed to air, it needs to be "re-activated" by heating, which will remove the thin surface layer formed on the getter surface. Generally, we will heat the getter material to $450°$C for 60 minutes. During this process, there is a significant pressure rise due to the molecules released from the getter and the heated air.

The ion pump [83, 84] works by ionizing molecules in the air into ions and adsorbing them.When a cold cathode discharge occurs in a magnetic field, electrons move back and forth in a spiral motion between the cathodes due to the magnetic field. When electrons collide with gas molecules, the gas molecules are ionized. When these ions collide with the cathode, they will be embedded in the cathode. The knocked-out titanium atoms will form a getter film on the surface of the cathode and anode that can absorb the gas molecules. It removes rare gas and methane, which are not pumped by the getter element.

The central vacuum chamber and the two atom heads are connected, So the working space of the turbopump and NEXTorr pumps also include the atom head chamber. Nevertheless, inside the atom head, The diameters of the orifices from the 2D chamber to the 3D chamber from the 2D MOT chamber to the 3D MOT chamber (2 mm) and the 3D MOT chamber to the detection chamber (19 mm) is relatively small, the following applies for the orifice conductivity

$$C_{or} = A \cdot \sqrt{\frac{k_B}{2\pi m_0}} \tag{3.24}$$

where A is the cross-section of orifice. So there will be a pressure difference between these chambers; therefore, both these two vacuum chambers are equipped with a NEXTorr ion/getter pump to improve the vacuum.

When our turbopump starts, its turbine speed will gradually increase from 0 to 650Hz. However, according to the analysis of Fig. 3.12, the vacuum chamber has a resonance at around 200Hz. When the turbine speed reaches this frequency, the entire chamber will make

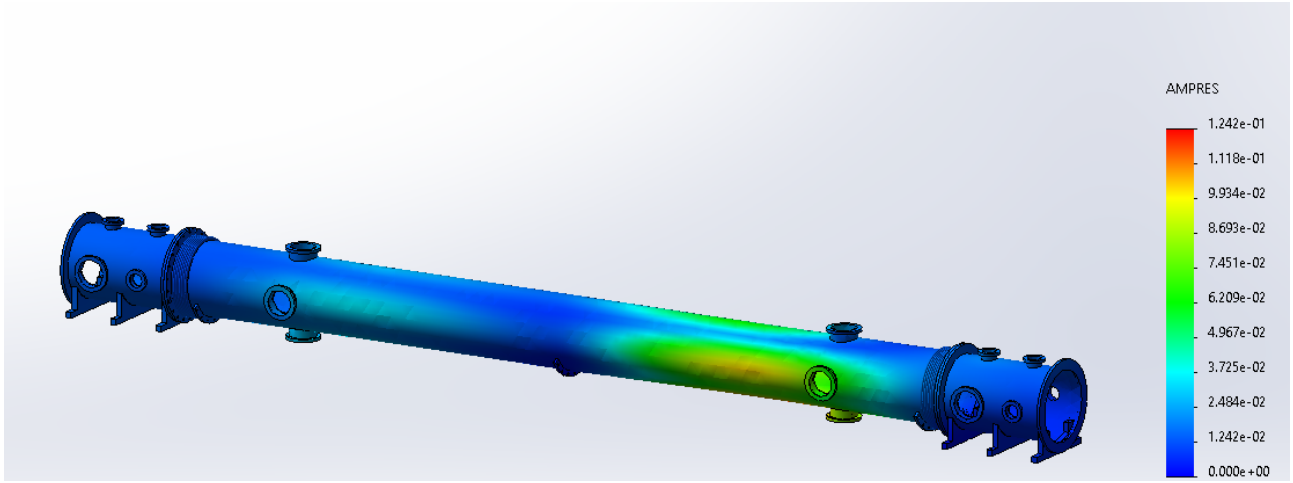

a

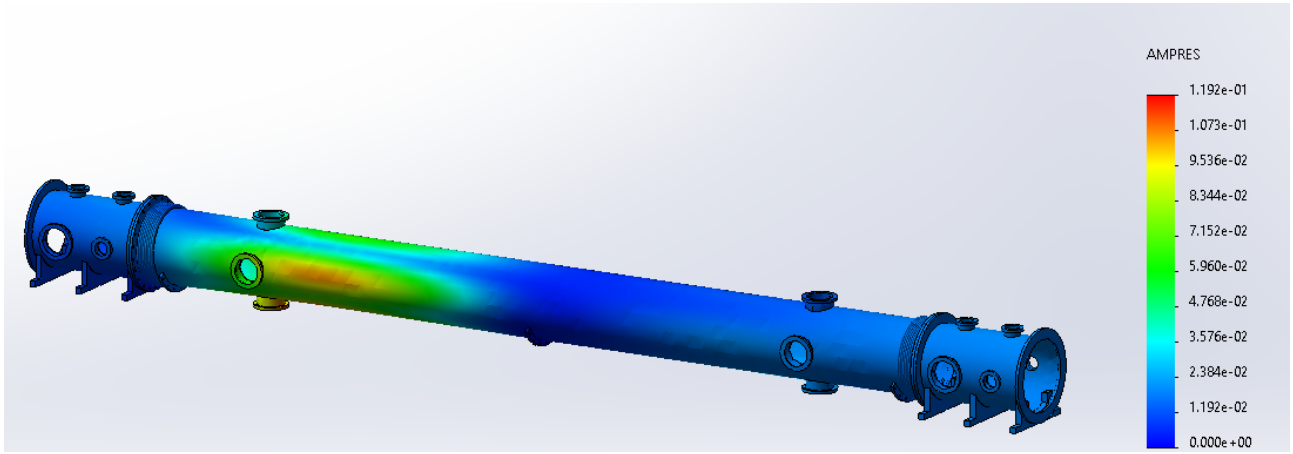

b

Figure 3.12: Resonance frequency analysis in the presence of gravity, (a) Amplitude mode with resonant frequency at 203.84 Hz (b) Amplitude mode with resonant frequency at 205.32 Hz.

a scary sound. This resonance will significantly reduce the service life of components and increase the vacuum pressure. Therefore, the following steps should be followed to prevent the occurrence of the resonance phenomenon.

First, close the gate valve between the turbopump and the cavity, which is equivalent to blocking the direct connection between the vibration source and the chamber, then start the turbopump, wait until its operating frequency reaches 650Hz and remains stable, then open the gate valve.

3.3.2.3 Baking

Baking can increase the desorption and diffusion rate, shortening the pump time and reducing the base pressure. According to the SAES test report, our vacuum chamber has been heated to 250°C and kept for 24 hours during previous processing and testing. Its base pressure can reach 1.5×10^{-11} mbar.

However, the absorption of gas during transportation and installation is unavoidable. Therefore, to obtain the required vacuum, we need to re-bake it to evaporate the water and some other substances attached to the inner wall of the cavity.

The method of baking such a large vacuum chamber in a MIGA project is more complicated than baking a small device. Therefore, it is necessary to test it in this atomic gradiometer experiment to calculate the requirements for the MIGA project.

The equipment required for baking is insulation material, heating device, and temperature monitoring device. Our baking process generally does not exceed 300°C and requires no accurate temperature measurement, so we use k type thermocouples for temperature monitoring; Considering the area and the power required, we choose a silicone rubber heating tape (BRISKHEAT DHCS25) as the heating tool. There are two points to note: 1. For most heating tapes, the temperature that they can reach are higher than their maximum exposure temperature, so do not use them without temperature monitoring feedback. We will introduce the consequences below; 2. The probe part of the thermocouple can generally withstand very high temperatures, 1400°C for K type [85], but the connection part of its insulation layer cannot withstand high temperatures, which should be kept away from the heating area as far as possible.

Typical high-temperature heat insulation materials include asbestos, diatomite, glass fiber, etc. And most of them are harmful to the human body. In the SAES report, a specially tailored heating jacket was used for heating and thermal insulation, which also contained these components. However, for a 150m-long cavity, it is neither safe nor budgetary to use a custom heating jacket containing these materials. We hope to achieve the same effect by wrapping the vacuum chamber with aluminum foil. For this, we conducted three tests.

In the first test, only one optical chamber was connected to the central chamber; we

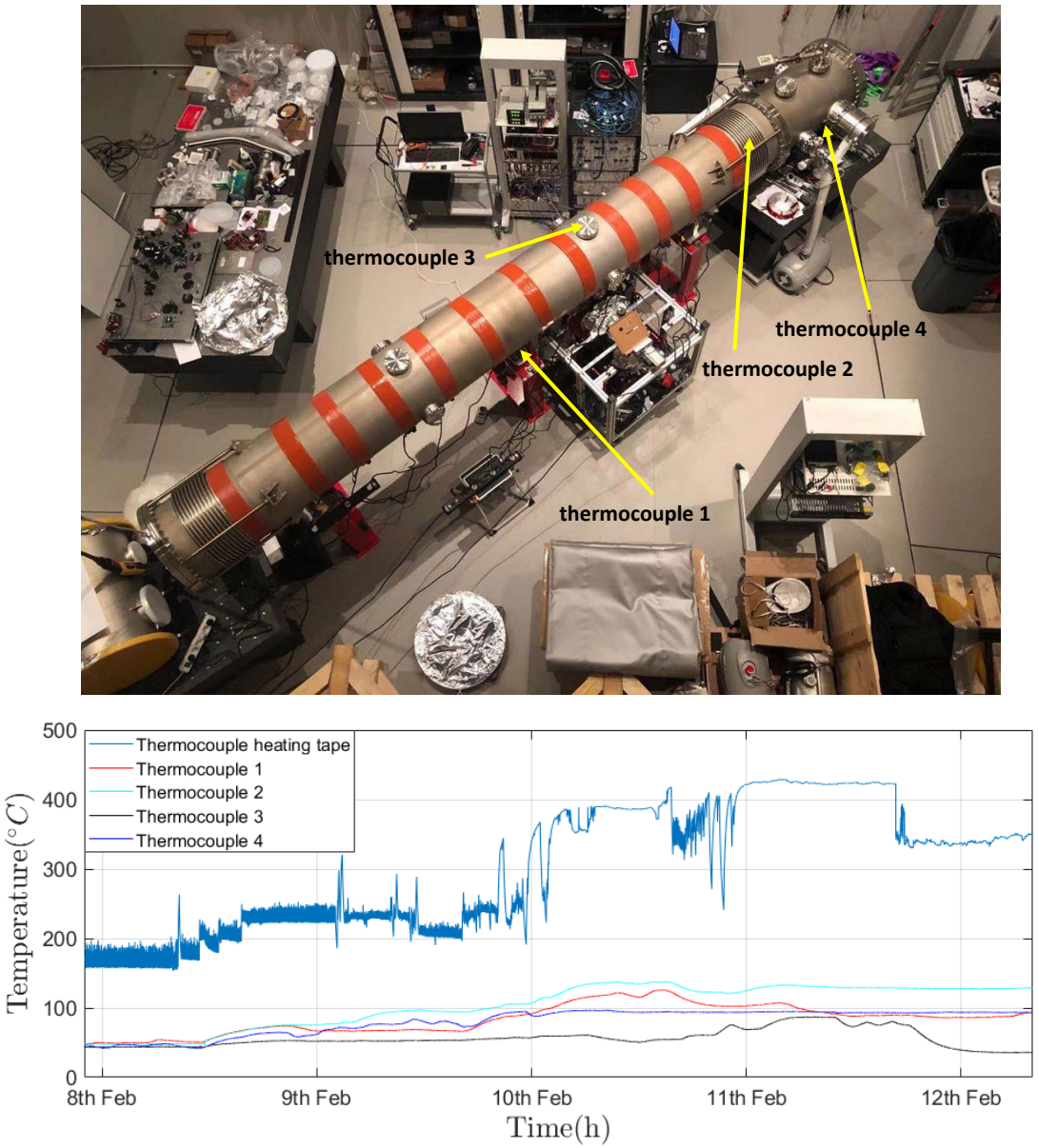

Figure 3.13: The photo taken for the first baking test before wrapping aluminum foil; thermocouple 1 is placed on the surface of optical chamber; thermocouple 2 is placed between the threads of the central chamber bellows; thermocouple 3 is in the center of the blank flange; The thermocouple 4 is placed at the junction of the vacuum chamber and the supporting part (Top). The temperature and pressure changes after the second baking started. The system has been kept at standard pressure and humidity. Pressure measured in mbar and referenced to nitrogen (N2). Sampling time was one sample per second. The temperature of the heating belt started to get out of control on February 10 (Bottom).

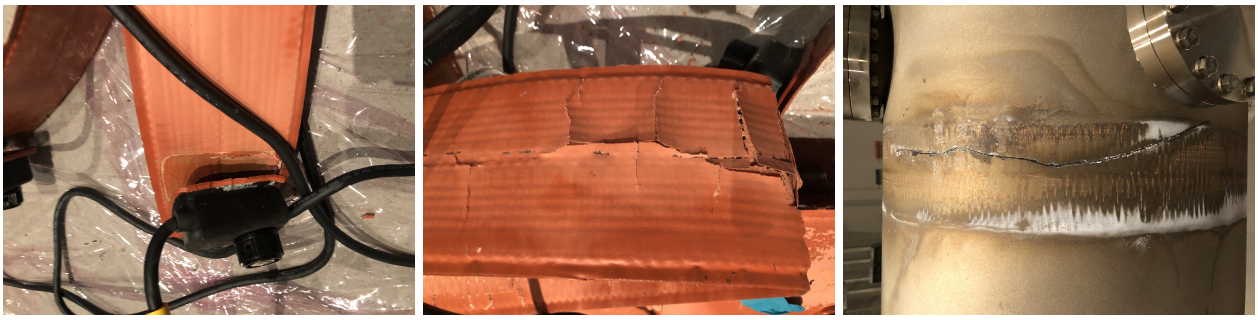

Figure 3.14: Heating tape damaged by overheating and its traces on the surface of the chamber.

wound 12 heating tapes on the central chamber and used two layers of aluminum (Thickness is about 0.1 mm) foil to prevent heat loss. All thermal data were collected by the 34972A LXI data acquisition/data logger switch unit, which is connected to the control computer for real-time observation. When the temperature of the heating belt approached 200°C, its surface began to emit white smoke and had a burning smell, and we had to interrupt the test. We suspected that it was caused by impurities on the surface of the heating belt, so we put all the heating belts on the surface of the aluminum profiles in the open space for heating. After 30 minutes, the white smoke disappeared. Also, it was found that two layers of aluminum foil were not enough. When the part covered by the heating belt reached 200°C, there are also some positions that can only reach only reach 70°C. And according to the design, the number of heating tapes per meter should be less, so we conducted a second baking test. Both optical chambers were connected to the vacuum in the second baking test. We used eight heating tapes, six of which were used to heat the central chamber, and the other two were used to heat the optical chamber. All the chambers were wrapped with three layers of aluminum foil, and all the thermocouples are in the same positions as the first baking.

Usually, heating the temperature to 120°C and keeping it for 48 hours is enough for us to obtain a vacuum of 10^{-10} mbar, but considering that our vacuum structure is large and the heat distribution is uneven. It can be seen from Fig. 3.13 that when the temperature of the heating belts rises to 200°C, the temperature at some locations can only reach 50°C, so we try this to further increase the heating power. Unfortunately, the heating strip exceeded its maximum exposure temperature of 218°C, its power controller was damaged, the temperature was out of control and rose to 400°C, which in turn burned the heating belts and

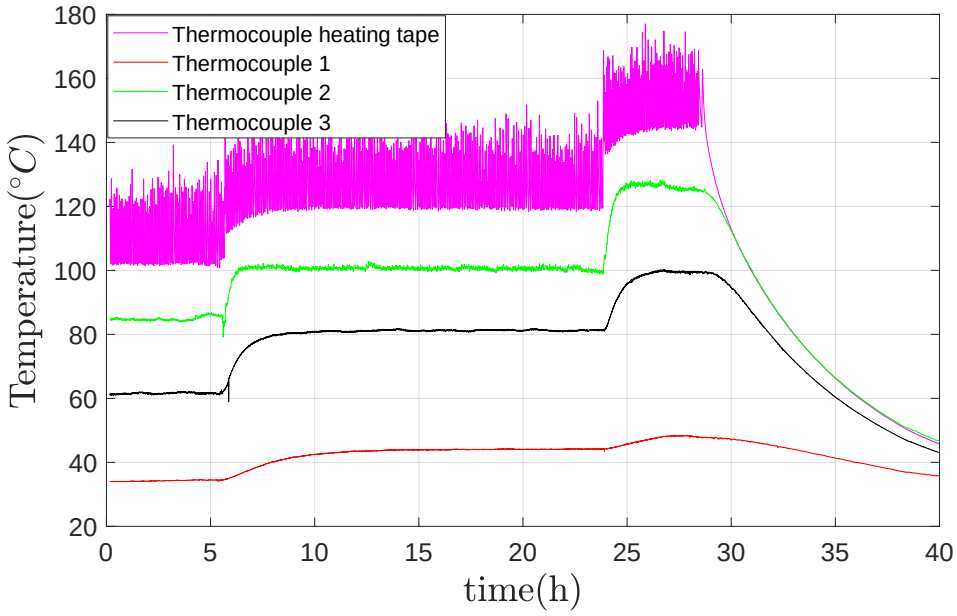

Figure 3.15: For the baking results of optical chambers, after the temperature stabilized to 100°C, we raised the temperature to 130°C.

thermocouples, leaving traces on the vacuum chamber as Fig.(3.14). This test proves that the temperature control method needs to be changed. We need to control the heating based on real-time temperature changes, and a more reliable heating tool is needed.

Since the two optical chambers did not reach 100°C during the second baking, we changed the temperature control method to bake them for the third time. With a temperature control module and a solid state relay (WATLOW PM6C1CJ/SSR-25A-240V-DC), we can more accurately and dynamically control the heating temperature. According to the Fig. 3.15, except for the middle part of the CF500 blank flange, The temperature of most locations of the optical chamber has reached 100°C for 20 hours.

Some other questions we need to answer are, what is the thermal insulation effect of aluminum foil, how should we use it in baking, and how much power is needed to make the cavity reach 100°C under the insulation of three layers of aluminum foil?

To analyze this problem, we need to start with some basic concepts. The three types of heat transfer are conduction, radiation, and convection. As a good conductor of heat, aluminum foil cannot reduce the thermal conductivity, but it effectively isolates convection. As

a result, a layer of hot air is formed on the surface of the vacuum chamber, which effectively reduces conduction and convection. The aluminum foil can also reflect the radiation of the vacuum chamber to reduce heat loss. The reflectivity of bright aluminum foil is 88%, while the dull embossed foil is about 80%. Therefore, we should ensure that the bright side faces inward, and the first layer of aluminum foil should be as close as possible to the chamber surface to help the temperature of different parts rise evenly. The gaps are kept as much as possible between the two outer layers to form an air insulation layer between them. According to our measurement, when the inner surface of the chamber reaches 100 °C, the outermost layer of aluminum foil is only 50 °C

After heating the cavity to 120°C, the heating is stopped. The temperature drop curve is shown in Fig. 3.16, from which the temperature change rate $\frac{dT}{dt}$ of the vacuum chamber around 100 °C can be obtained; combined with the heat capacity of the chamber, we can calculate its heat loss rate at 100 °C.

The heat capacity of our vacuum chamber material (AISI type 304 stainless steel) is c = 500 J·g^{-1}·K^{-1}; its density is ρ = 8000 $\mathrm{kg/m^3}$. The density of the gas inside the vacuum chamber is so small that its heat capacity is negligible compared to stainless steel. the inner diameter of the vacuum chamber is ID = 250 mm, the outer diameter is OD = 255 mm. However, considering each flange interface, the volume per unit length is much larger than the volume of the chamber wall. Here, according to the volume measurement in SOLIDWORKS, the volume of a vacuum cavity with a length of 6 m is 0.0548 m^3, that is, the volume per unit length $V/L = 0.009$ m^2, therefore, its heat capacity is:

$$C = c\,\rho\,V/L = 36533\ J/K \tag{3.25}$$

Combining Fig. 3.16, in the case of three layers of aluminum foil wrapping, the heat loss rate of the vacuum cavity per unit length near 100 °C is

$$q_{100} = C\frac{dT}{dt} = 190\ W \tag{3.26}$$

The three methods of heat transfer are all positively related to temperature, so theoretically, when the temperature is lower than 100 °C, the heat loss rate is less than q_{100}, we only

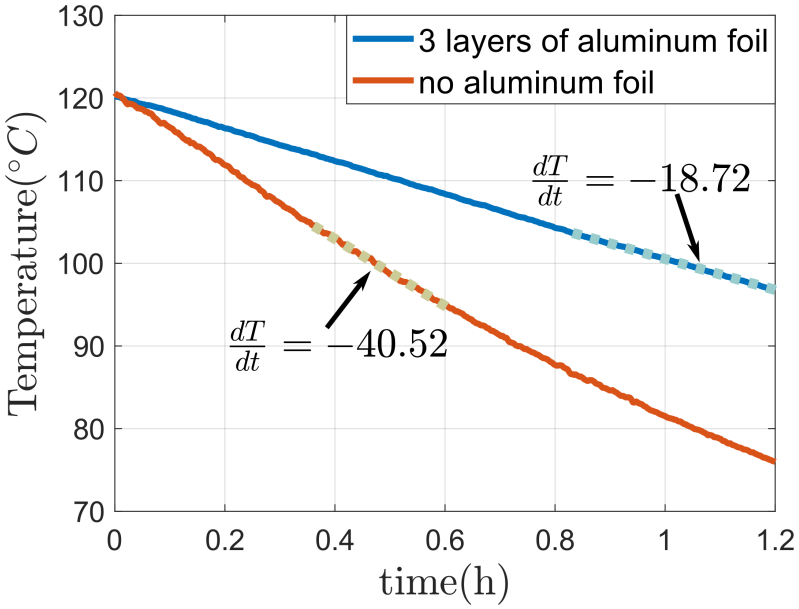

Figure 3.16: Heating the vacuum chamber to 120 °C, stop and measure the temperature change.

need to provide the same heating power for the vacuum chamber to reach 100°C. However, considering that the heating efficiency is less than 100% and the heat dissipation rate of each position is different, the actual required power should be higher.

For this reason, we did another test: we wrapped a small vacuum cavity (AISI 304, m = 13.7 kg, has a similar surface area/mass ratio as the MIGA vacuum chamber, so the power consumption of the MIGA can be estimated based on this) with three layers of aluminum foil and baked it to 100 °C. According to the temperature curve, the dissipation rate is $70W$, and the inner wall of the cavity can reach 100°C when the power of the heating belt is 90 W. According to this efficiency test, the heating power required to heat a unit length of the vacuum chamber is 244 W, and the total baking power of a 150 m long chamber is about 36.6 kW.

In addition, during the baking process, there are still some places where the temperature does not reach 100 °C, including the part connected to the support and most of the blank flanges, so we should bake all the flange parts separately before sealing the vacuum chamber.

3.3.2.4 Result

The pressure changes in the vacuum chamber under different conditions measured by gauges are shown in the figure, and the corresponding base pressures are:

· 2.582×10^{-9} mbar for the central chamber and one optical chamber before baking; pump speed = 920 l/s with turbo pump.

· 1.037×10^{-9} mbar for the central chamber and the two optical chambers after the second baking; pump speed 920 l/s with turbo pump.

· 8.554×10^{-10} mbar for the central chamber and the two optical chambers after the third baking; pump speed $920 + 200 + 100 = 1220$ (l/s) with turbo pump and two ion/getter pumps.

· 1.416×10^{-9} mbar after raising the pressure to vacuum through the filter and venting valve and connecting the two atomic heads to the cavity; pump speed $= 1220$ l/s with turbo pump and two ion/getter pumps.

After both atom heads are connected to the vacuum chamber, we turn on the turbopump and the ion pump, measure the final vacuum data (Fig. 3.17(b)), compared to the first time, with the help of the ion/getter pump, the pump speed is increased, but the base pressure is also increased to 1.416×10^{-9}mbar, this is due to two reasons. First, the chamber space is increased; Second, the vacuum chamber was opened twice during the connection processes, leaking in some gas that can be adsorbed on the inner wall of the chamber. Nevertheless, the result is good enough to meet our needs in any case.

In this pressure range, the limit of base pressure can be described by the following formula:

$$P = \frac{Q}{S} + P_0, \tag{3.27}$$

The total pressure P is determined by the outgassing rate Q of all surfaces and components, the pumping speed S, and the base pressure P_0 of the pumping group. The internal surface area A of the cavity is given at the beginning of this section; considering the various flange interfaces and the optics we put in, we can assume that the internal surface area is 11 m^2, the pump speed of the pump group is 920 l/s, the base pressure is 1×10^{-10} mbar, so the outgassing rates in the four cases are:

· 2.08×10^{-11} mbar $\cdot$ l $\cdot$ $s^{-1}cm^{-2}$ without baking;

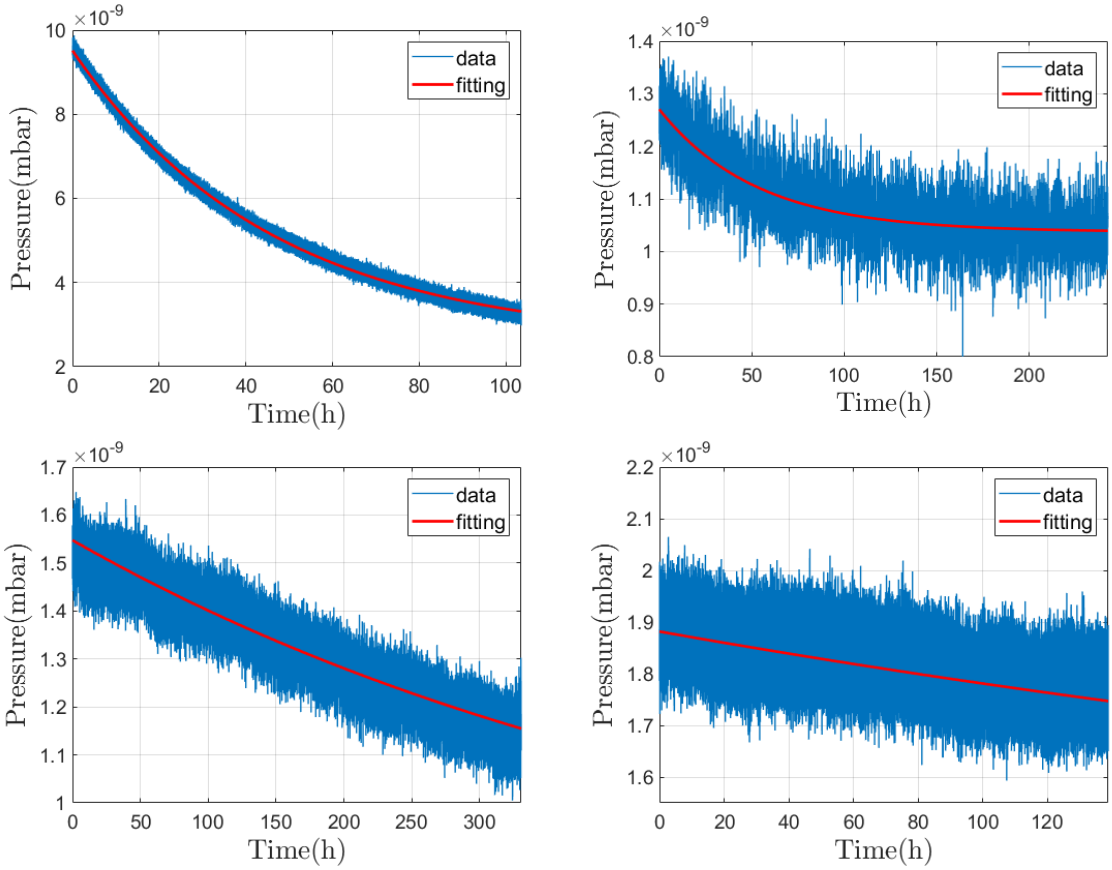

Figure 3.17: (a) pressure for central chamber and one optical chamber before baking; (b) pressure for central chamber and two optical chambers after second baking; (c) central chamber and two optical chambers after third baking chamber pressure; (d) after the third baking, we vent the vacuum to the atmosphere and connect the two atom sources, the pressure measured after the pump.

$\cdot 7.84 \times 10^{-12}$ mbar $\cdot$ l $\cdot$ s^{-1}cm^{-2} baking at 100°C for 48 hours;

$\cdot 6.31 \times 10^{-12}$ mbar $\cdot$ l $\cdot$ s^{-1}cm^{-2} baking at 100°C for additionl 20 hours;

$\cdot 1.45 \times 10^{-11}$ mbar $\cdot$ l $\cdot$ s^{-1}cm^{-2} after connecting the two atom sourecs.

So in the MIGA project, with proper baking, we can assume that the outgassing rate is 6×10^{-12} mbar $\cdot$ l $\cdot$ s^{-1}cm^{-2}, the cavity length is $L_{\text{MIGA}} = 150$ m, the inner surface area is $A_{\text{MIGA}} = 2\pi r\, L_{\text{MIGA}} + 2\pi r^2 \approx 2.4 \times 10^6$ cm^2. Assuming the base pressure of the pump system is 5×10^{-11} mbar, the total pump speed required to make the pressure in the vacuum chamber reach 2×10^{-9} mbar is about 7500 l/s.

3.3.3 Venting

After UHV is reached in the chamber, we may need to restore the vacuum to ambient pressure to add new optics. The easiest way to do this is to unseal a blank flange, but this has several disadvantages; first of all, it will cause a large amount of gas and impurities to enter the vacuum chamber and damage the flange seal suddenly; at the same time, the water vapor in the air enters the vacuum chamber again, which means that we have to perform the complex baking process again.

A more reasonable way is to use a venting valve with a filter. We use a venting valve (Pfeiffer Vacuum, EVR 116) combined with a filter (Pfeiffer Vacuum, Dust Separator SAS 16). The venting valve can control the gas at 5×10^{-6} mbar·l/s - 1.25×10^{3} mbar·l/s speed entry, and the filter can reparator particles above 5 μm and absorb some water.

Unfortunately, although the venting valve provides a control circuit and can communicate between PCs through RS232, it does not provide any visual interface, and its serial port commands often have format problems. So I wrote a LabVIEW program to simplify serial communication and update the opening status of the venting valve.

3.3.4 Leak detection

A leak search aims to localize a leak and/or to determine the total or local leak rate[86]. A relatively quick and straightforward leak detection method is to monitor pressure changes. For example, solvent (Acetone or alcohol) can be used to spray suspected leak points, and

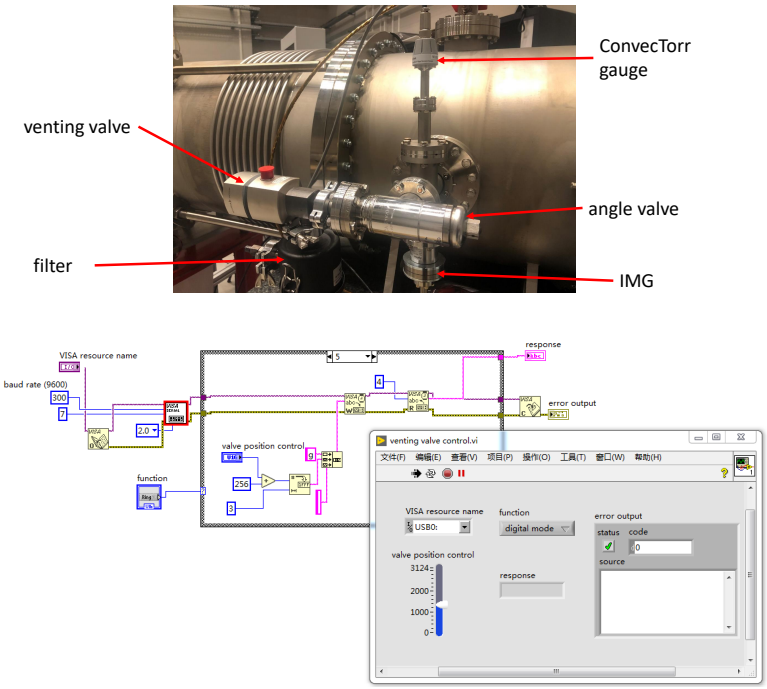

Figure 3.18: The two gauges and the venting valve are connected to the optical chamber left, with an angle valve in the middle (top). LabVIEW front panel for controlling venting valve (bottom)

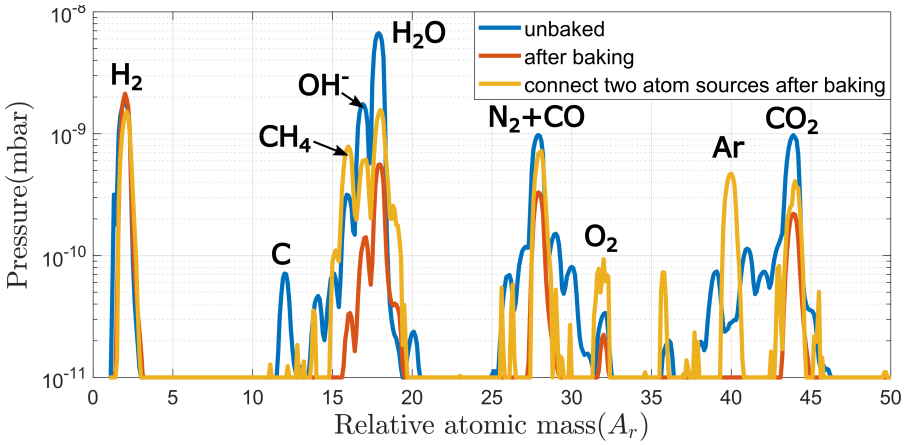

Figure 3.19: The vacuum chamber residual gas spectrum, with the gas molecules corresponding to each peak marked out. The three scans correspond to the case: (blue) the vacuum chamber is not baked, (red) after two bakings, and (yellow) after baking with two atom sources connected.

at the same time, use the vacuum gauges to observe whether there is a significant increase or decrease in pressure when the solvent enters the leak. The disadvantage of this method is that the sensitivity is relatively limited (10^{-4}mbar), and the solvent may corrode the rubber components, but the advantage is that it can quickly and continuously probe multiple locations.

A more accurate method is tracking gas and RGA to analyze leaks. There is a leakage test mode in the RGA software. After the tracking gas is selected, the RGA will continue to monitor the target gas. In the case of UHV, small leaks will show noticeable spikes on the RGA. If the leakage position is far from the RGA, it takes a while for the RGA to respond after releasing the tracer gas (about 30 s in our case). The common choice of tracking gas is helium, which has the following advantages as a tracking gas:

1. the content of helium in the environment is very low;

2. chemically and physically inert, non-explosive, and cheap;

3. The small diameter of the helium atoms allows the detection of tiny leaks; the detection accuracy can reach 10^{-11} mbar/s;

4. removable by pumping and not contaminating the system.

The disadvantage is that the pumping speed of helium is relatively slow; the helium molecules will spread quickly in the environment during the detection process. Therefore, it is necessary to wait for a while between the two detections and wait until the concentration of helium released in the last release is low enough before performing the subsequent detection to avoid errors. We performed leak monitoring both when connecting the optical and central chambers and when connecting the two atom sources to the vacuum chamber. After the first atom source was connected, we saw obvious signs of leakage, the pressure in the vacuum chamber increased slightly from 3.2×10^{-9} mbar to 3.5×10^{-9} mbar, and inside the atom source, the current of the 3D MOT chamber's ion pump[1] was significantly higher than that of the 2D MOT chamber, through the helium detection, We found a leak in the viewport flange window of the detection beams within the atom head. The pressure inside the atomic source dropped significantly after the window was replaced.

[1]The current of the ion pump can reflect the change of vacuum to a certain extent

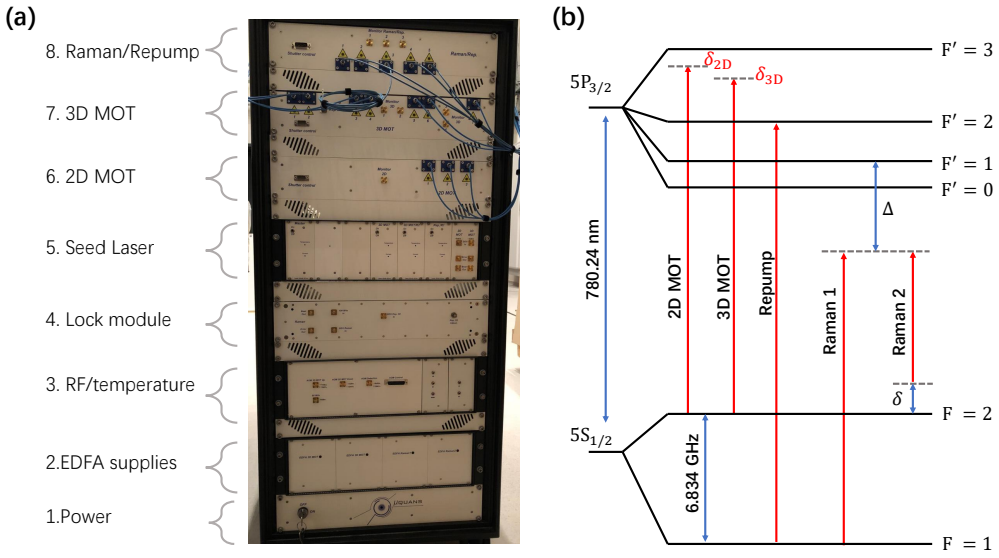

Figure 3.20: (a) Laser system in the rack, 1. power module, which converts 240 VAC into DC required by other modules; 2. high-power EDFA control; 3. RF components required by some frequency-locking modules, temperature servo control, and the main control module embedded with the Linux system; 4. the main frequency lock module; 5. the seed laser and corresponding components; 6. the 2D MOT optical module, including PPLN and shutter; 7. 3D MOT optical module, including PPLN, shutters and AOMs; 8. Raman and repump optical modules, including PPLNs shutters, and AOMs. (B) The D2 transition line of the ^{85}Rb and the lock-in frequency of each seed laser.

3.4 Laser system

3.4.1 Laser rack

The laser system is developed in collaboration with Muquans[67], the laser components and the corresponding locking control module are integrated into a 117 cm × 80 cm × 55cm rack [69]. This rack uses a standard 240 V main power supply. It can be controlled via Ethernet according to the ssh protocol, ensuring the portability of the entire laser system.

There are four seed lasers in the system; one is the master laser, the other three are called 2D MOT seed, 3D/Raman2 seed, and Repump/Raman1 seed, respectively. All seed lasers use 1560 nm external cavity diode lasers (ECDL), providing seed light with a line width of 10 kHz and a power of 10 mW. Then the frequency is doubled to 780 nm for rubidium atoms through the periodically-poled Lithium Niobate (PPLN). In order to obtain enough power

after the frequency doubling, the Erbium-doped fiber amplifiers (EDFA) are used to amplify the laser power.

The Master laser diode is locked on a ^{85}Rb absorption line (crossover 3x4 of ^{85}Rb) and acts as the optical frequency reference for the system. After a splitting/combining stage, the other three slave diodes are phase-locked on the Master diode. The optical layout is shown in Fig. 3.21

The 2D diode is phase-locked on the ^{87}Rb $5^2S_{1/2}\ F = 2 \rightarrow 5^2P_{3/2}\ F' = 3$ line and modulated with EOM, which adds the F frequency sideband for repumping, then it is amplified with an EDFA and frequency-doubled. After splitting, it provides three outputs at 780 nm; Two beams are used respectively for the horizontal and vertical cooling of the 2D MOT; the other one is the 2D MOT push beam.

The 3D/Raman2 laser is initially locked on ^{87}Rb $5^2S_{1/2}\ F = 2 \rightarrow 5^2P_{3/2}\ F' = 3$ transition line. It is divided into two parts. One part is amplified and frequency-doubled and used as a 3D MOT beam. This 3D MOT beam is divided into seven beams of 780 nm. These seven beams are divided into three groups, three of which are 3D Up beams, three 3D Down beams, and the other one is Detect beam. Each group has an AOM for frequency adjustment.

The Repump/Raman1 laser is based on 3D MOT/Raman 2 instead of Master seed as the locking reference and is initially locked on ^{87}Rb $5^2S_{1/2}\ F = 1 \rightarrow 5^2P_{3/2}\ F' = 2$ transition. It is also amplified and frequency-doubled. After that, It is divided into repump light and Raman 1; the repump light is divided into three beams, one is injected into the 3D MOT, and the other two beams are used for push and detection stages. Raman 1 light and Raman 2 light separated from 3D/Raman2 combined and split into Raman Up and Raman down. Unlike 3D MOT beams, the AOMs of Raman2 and repump/raman1 are all in 1560 nm. Most of the optical path transmission of the laser system uses polarization-maintaining fibers to ensure the system's stability, but in the splitting part, miniaturized free-space optical elements are used to adjust the splitting ratio. In addition, each light is equipped with a photodiode for power detection, which can be monitored by PC through ssh connection (Sec. 3.4.3).

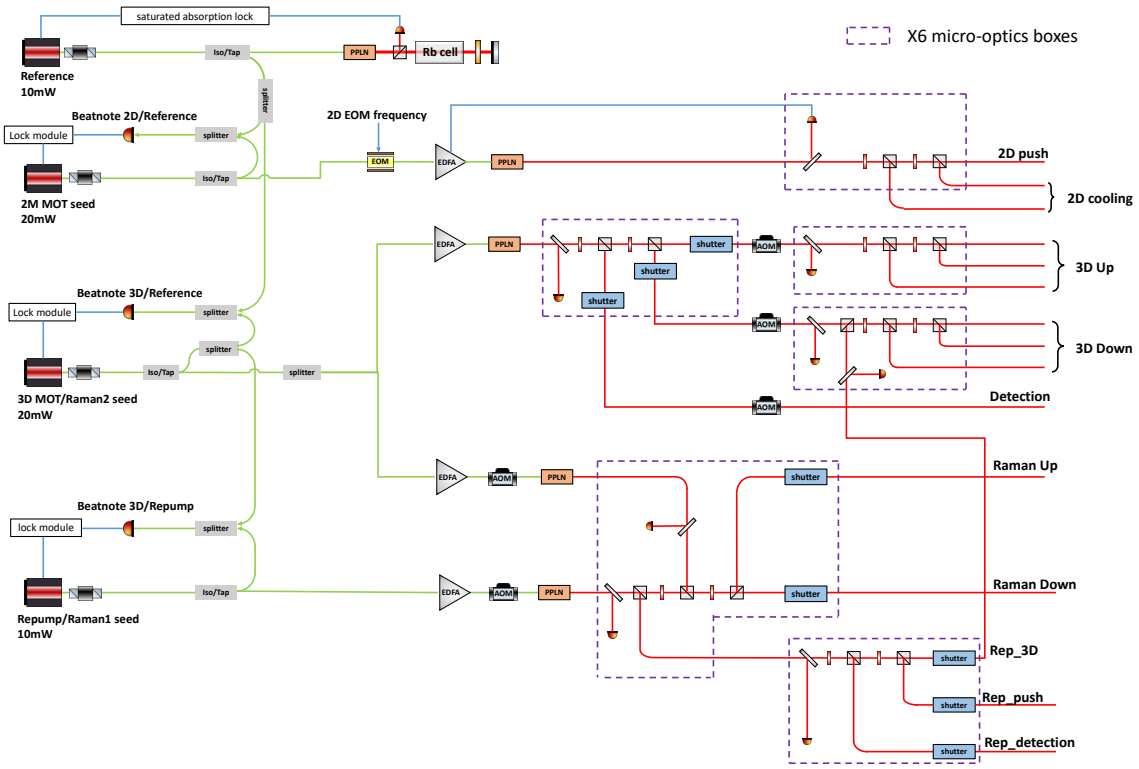

Figure 3.21: Light path structure of the laser box

3.4.2 Laser Frequency Chain

The frequency control part contains internal signals and external signals (Fig. 3.22). The phase-locked dielectric resonant oscillator (PLDRO) in the lock module generates a 3.5GHz reference signal, the 6.834GHz frequency required for 2D MOT EOM and repump seed is obtained by mixing this signal with DDS input and frequency doubling. For reference, Fig.3.24 shows the laser beat linewidth of one of the systems we tested.

The external signal includes a 100 MHz clock signal, which is used to synchronize the DDS signal; the external input DDS signal:2D MOT In, 3D MOT/Raman 2 In, Repump/Raman 1 In, these signals are mixed with the divided beat note signal and then act as the input signal of phase-locked PID. Different dividers are used here to ensure that the required DDS signal is in the range of 50-200 MHz, which is also a typical output of general commercial DDS modules.

In addition to adjusting the locking frequency of the seed laser through the DDS input, there is also AOM in the optical path. By changing the externally input AOM frequency signal,

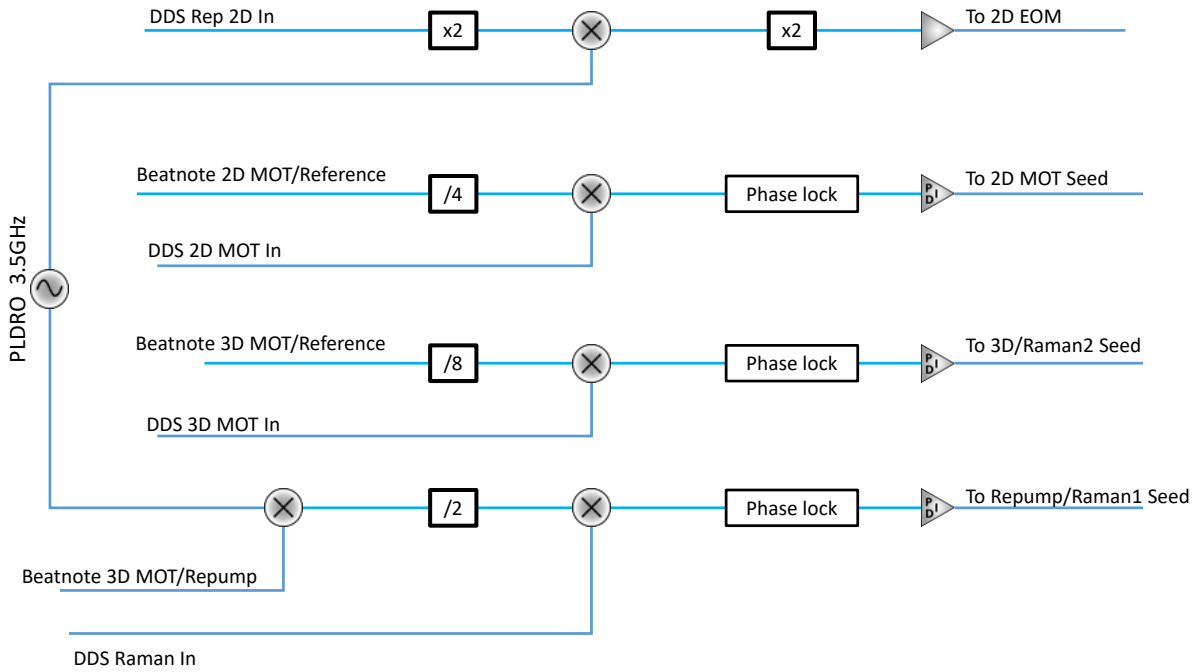

Figure 3.22: Schematic diagram of laser frequency locking module

the optical frequency of the laser beam can be easily shifted, and the the laser power can be controlled by adjusting the amplitude of the AOM input signal.

Combining Fig. A.1 and Fig. 3.22, the resonant DDS input signal frequencies can be calculated. The D2 baselines of ^{87}Rb and ^{85}Rb are respectively:

$$\begin{aligned} f_{Rb85} &= 384230406.373 \text{ MHz}, \\ f_{Rb87} &= 384230484.468 \text{ MHz}. \end{aligned} \tag{3.28}$$

The frequencies of D2 ^{85}Rb $5^2S_{1/2}$ F $=$ 3 $\rightarrow$ $5^2P_{3/2}$ F$^{'}$ $=$ 4 transition and ^{87}Rb $5^2S_{1/2}$ $F = 2 \rightarrow 5^2P_{3/2}$ F$^{'}$ $= 3$ transition are respectively

$$\begin{aligned} f_{3-4} &= f_{Rb85} - 1264.889 \text{ MHz} + 100.205 \text{ MHz}, \\ f_{2-3} &= f_{Rb87} - 2563.005 \text{ MHz} + 193.741 \text{ MHz}, \end{aligned} \tag{3.29}$$

The frequency between ^{85}Rb $5^2S_{1/2}$ F $=$ 3 $\rightarrow$ $5^2P_{3/2}$ F$^{'}$ $= 3/4$ crossover peak to the ^{87}Rb $5^2S_{1/2}$ $F = 2 \rightarrow 5^2P_{3/2}$ F$^{'}$ $= 3$ cooling line is

$$f_{base} = f_{3-4} - 120.640/2 - f_{2-3} = 1066.17 \text{ (MHz)}, \tag{3.30}$$

considering the AOM with 110 MHz shift at 1560 nm, the DDS frequency of 3D MOT

$$f_{3D} = (f_{base} + 110)/16 = 73.5103 \text{ (MHz)}, \tag{3.31}$$

and the DDS frequency of 2D MOT seed is

$$f_{2D} = f_{base}/8 = 133.271 \text{ (MHz)}. \tag{3.32}$$

Note that the Repump/Raman 1 seed is 3D MOT/Raman 2 seed before 3D MOT AOM, so the DDS frequency of repump beam with 80 MHz shift AOM at 780 nm is,

$$f_{repump} = (3500 - (6834.683 - 266.650 + 110)/2 + 80)/2 = 120.492 \text{ (MHz)} \tag{3.33}$$

Raman Up and Raman Down beams are the combinations of 3D MOT/Raman 2 and Repump/Raman 1 seeds. The frequency difference between the virtual energy levels excited by the Raman transition and $5^2\mathrm{P}_{3/2}$ $\mathrm{F}^{'} = 1$ is Δ. The detuning of Raman 2 beam relative to the energy difference between the virtual energy level and $5^2\mathrm{S}_{1/2}$ $F = 2$ is δ. Different momentum can be selected by changing δ. Reference transition for Raman 2 beam is $5^2\mathrm{S}_{1/2}$ $F = 1 \rightarrow 5^2\mathrm{P}_{3/2}$ $\mathrm{F}^{'} = 1$, the corresponding DDS frequency is

$$f_{raman2} = (f_{base} + 160 + 266.65 + 156.95)/16 = 103.11 \text{ (MHz)}, \tag{3.34}$$

The frequency for Repump/Raman 1 $5^2\mathrm{S}_{1/2}$ $F = 2 \rightarrow 5^2\mathrm{P}_{3/2}$ $\mathrm{F}^{'} = 1$ DDS is

$$f_{raman1} = (3500 - (6834.683 + 160)/2 + 80)/2 = 41.3293 \text{ (MHz)}. \tag{3.35}$$

We also need to use the probe light and the repump push beam (from Raman 1) to clear the remaining atoms after the velocity selection. The repump-push is used to push the atoms from $5^2\mathrm{S}_{1/2}$ $F = 1$ excites to $5^2\mathrm{P}_{3/2}$ $\mathrm{F}^{'} = 0$,

$$f_{repump-push} = (3500 - (6834.683 - 266.650 - 229.85 + 110)/2 + 80)/2 = 177.80 \text{ (MHz)}. \tag{3.36}$$

It should be noted here that the repump light does not have to be locked at ^{87}Rb $5^2\mathrm{S}_{1/2}$ $F = 1 \rightarrow 5^2\mathrm{P}_{3/2}$ $\mathrm{F}^{'} = 2$, When we locked the Rep/R1 laser during the experiment, a mode hopping point may appear near the locking slope, due to which the laser will lose lock when the frequency ramp is performed. Therefore we can also lock the laser at ^{87}Rb $5^2\mathrm{S}_{1/2}$ $F = 1 \rightarrow 5^2\mathrm{P}_{3/2}$ $\mathrm{F}^{'} = 1$ line and the corresponding DDS input frequency is:

$$f_{repump2} = (3500 - (6834.683 - 266.650 - 156.947 + 110)/2 + 80)/2 = 159.728 \text{ (MHz)}$$

Meanwhile, for the three slave lasers, the DDS input frequency changes required to gen-

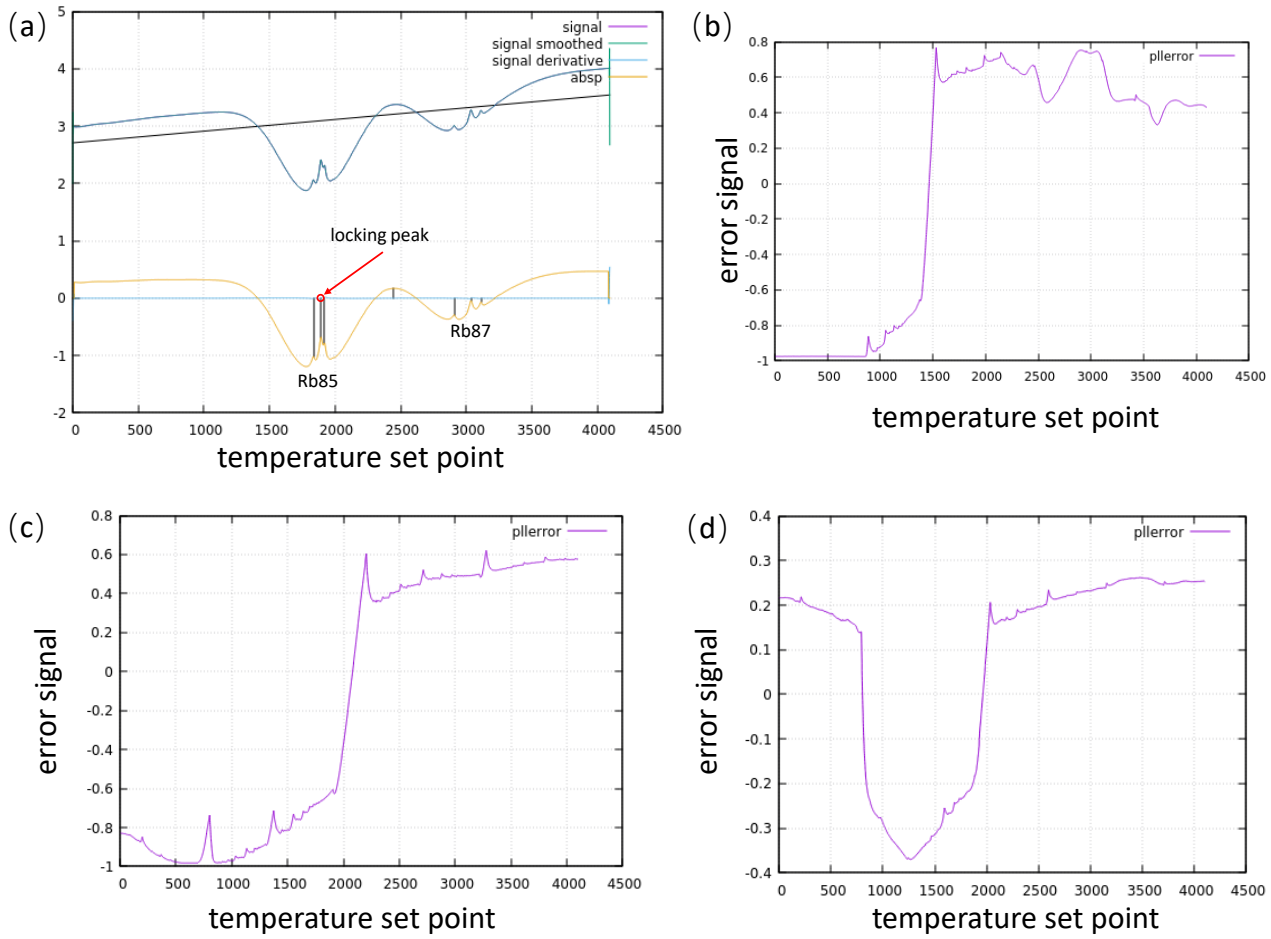

Figure 3.23: Seed laser locking curves obtained by ssh connection. The laser is locked through the slope near the zero point of the error signal. (a) Master laser locking curve. (b) 2D MOT laser locking curve. (c) 3D MOT laser locking curve. (d) Repump/Raman1 laser locked at ^{87}Rb $5^2S_{1/2}$ $F = 1 \rightarrow 5^2P_{3/2}$ $F^{'} = 2$ transition, with an obvious mode jump next to the locking slope. (e)The Repump/Raman1 laser locked on ^{87}Rb $5^2S_{1/2}$ $F = 1 \rightarrow 5^2P_{3/2}$ $F^{'} = 1$.

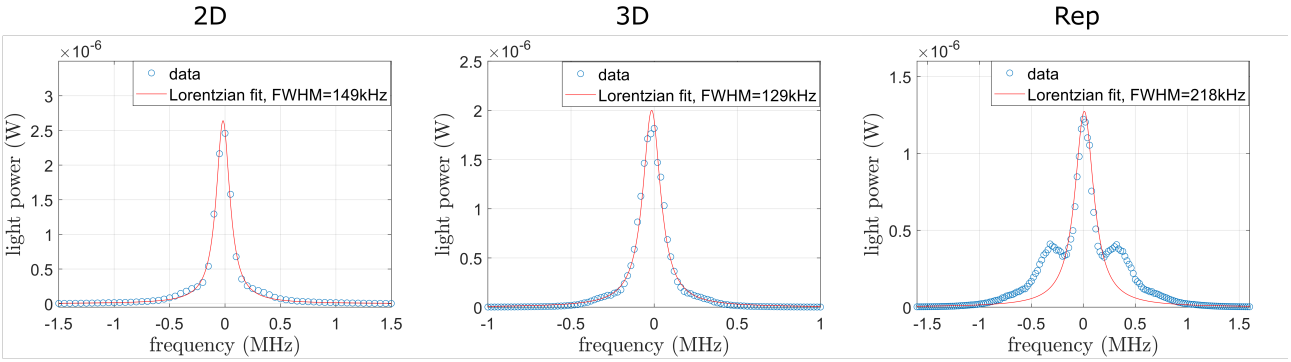

Figure 3.24: Linewidth of beatnote for laser system MIGA32

erate $1\Gamma = 6.0659$ MHz are also different, respectively: $\gamma_{3D} = \Gamma/16 = 0.379119$ MHz, $\gamma_{2D} = \Gamma/8 = 0.758238$ MHz, $\gamma_{repump} = \Gamma/4 = 1.51648$ MHz.

3.4.3 Remote control

We can connect the laser system to the computer through Ethernet and control it with the ssh protocol. The module (3) in Fig. 3.21 is used as a gateway. The computer used for control and the embedded control system of other modules is under the same subnet. Each module has a different static IP address (netmask 255.255.255.0).

For example, the gateway address is 192.168.1.1, the control computer's IP address can be set to 192.168.1.2, and the ip addresses of other modules are also under the same subnet. Through ssh, we can connect to these modules and monitor the temperature and current of all seed lasers, start, end, or change the parameters of the frequency lock loop. Other features include

1. Lock each seed laser and draw locking curves (Fig. 3.23),
2. monitoring the parameters of EDFA,
3. changing EDFAs' feedback method and setpoint,
4. monitoring the optical power detected by all photodiodes,
5. enabling/disabling the function of shutters.

3.5 Cavity Optics

In addition to the laser system for the atomic head, there are also lasers for manipulating atoms; because the interaction between this light and the atoms causes Bragg scattering, we generally call this light " Bragg beam."

As an intermediary for sensing gravitational waves and interacting with atoms, the Bragg beam has a critical impact on the sensitivity of atomic interferometers. In this section, we discuss how to construct a Bragg beam and improve the quality of the Bragg beam through a stable cavity.

3.5.1 Bragg Beam Preparation

The Bragg beam is generally far detuned. Since it directly determines the atom momentum transition and the lattice pulse's effect, it requires frequency locking and power stabilization. We achieved the Bragg beam with a free-space optical path. The diagram of which is shown in Fig. 3.25.

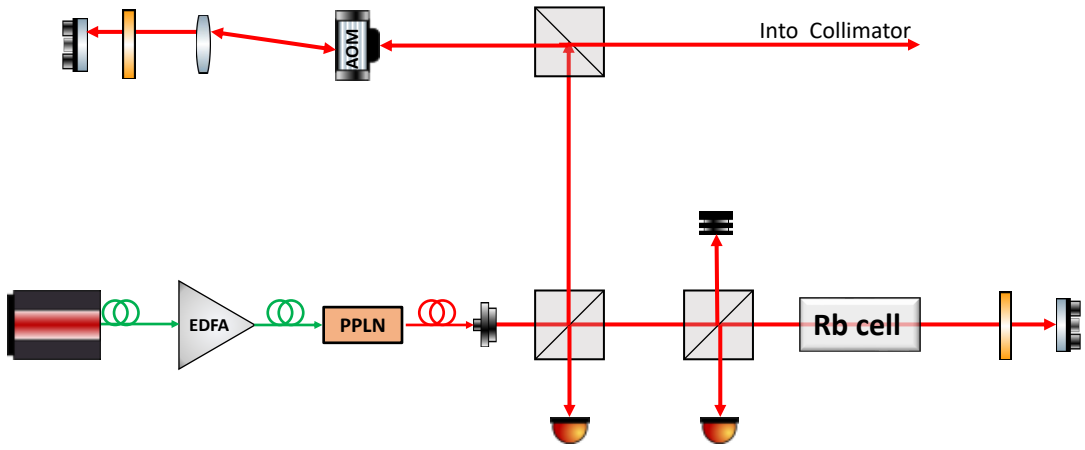

Figure 3.25: The optical path of the Bragg light, in which the AOM double pass is used to adjust the light intensity

3.5.2 Stable cavity

In Sec. 2.2 we discussed that in order to achieve the Bragg regime, we need a sufficient interaction time t_{int}, which is limited by the pulse time and beam width. In addition, the beam's intensity has a Gaussian distribution along the radial direction. This radial gradient of intensity affects the efficiency of the Bragg pulse, and the wider the beam, the smaller the intensity gradient. Therefore, a larger beam waist is needed based on these two points.

In experiments using optical resonators to enhance AI sensitivity, to ensure the optical resonator's stability, the most simply wa use a confocal optical resonator. The beam waist of such a resonator is relatively small. To obtain a larger beam waist, we propose [87] a marginally stable optical resonator, in which the beamwidth is effectively increased by adding

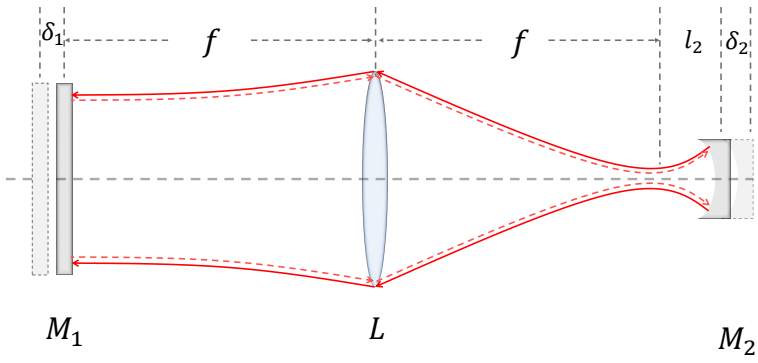

Figure 3.26: Diagram of the resonant cavity.M_1, M_2 represent a flat mirror and a concave mirror, respectively, L represents a convex lens with a focal length f, δ_1 and δ_2 represent the shaking of the two mirrors, respectively. A larger beam waist is obtained on the M_1 side.

a convex lens. After that, we further consider replacing one of the flat mirror with a concave mirror to make it stable.

The geometry of a stable resonator is shown in Fig. 3.26. A flat mirror M_1 stuck on a PZT is placed at the focal point of lens L, the concave mirror is placed $l_2 + f$ away on the other side. The beam is injected into the cavity from the curved mirror. The transmission matrix is used here to analyze the propagation of the optical path and the beam width

The ABCD transfer matrices of a beam passing through in free space, passing through a lens, and being reflected by a curved mirror are respectively:

$$\begin{bmatrix} 1 & l \\ 0 & 1 \end{bmatrix}, \begin{bmatrix} 1 & 0 \\ -\frac{1}{f} & 1 \end{bmatrix}, \begin{bmatrix} 1 & 0 \\ \frac{2}{R} & 1 \end{bmatrix}, \tag{3.37}$$

where l is the length of the free space, f is the focal length of the lens and R represents the curvature of the mirror. The total round-trip transfer matrix is therefore

$$\begin{aligned} T = &\begin{bmatrix} 1 & f+\delta_1 \\ 0 & 1 \end{bmatrix} \begin{bmatrix} 1 & 0 \\ -\frac{1}{f} & 1 \end{bmatrix} \begin{bmatrix} 1 & f+l_2+\delta_2 \\ 0 & 1 \end{bmatrix} \begin{bmatrix} 1 & 0 \\ -\frac{2}{R} & 1 \end{bmatrix} \\ &\times \begin{bmatrix} 1 & f+l_2+\delta_2 \\ 0 & 1 \end{bmatrix} \begin{bmatrix} 1 & 0 \\ -\frac{1}{f} & 1 \end{bmatrix} \begin{bmatrix} 1 & f+\delta_1 \\ 0 & 1 \end{bmatrix}, \end{aligned} \tag{3.38}$$

here δ_1, δ_2 represent the position noise of two mirrors, and l_2 is the offset of the curved mirror

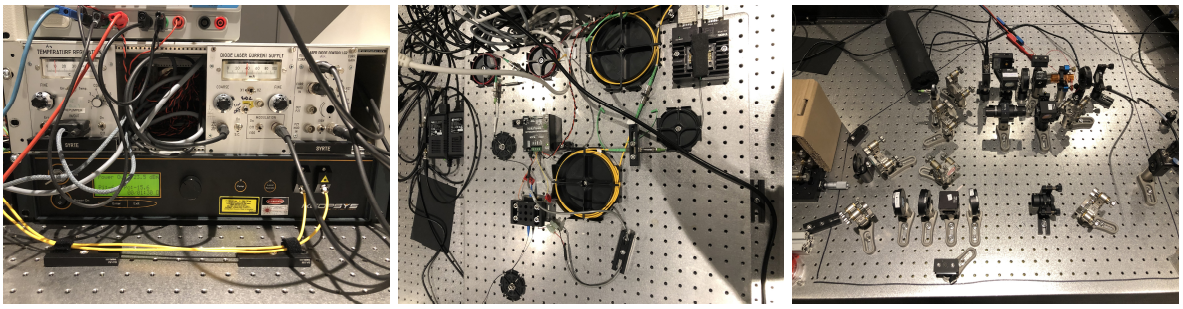

a b c

Figure 3.27: Laser source optics for stable cavity. (a) The laser diode's temperature/current control module, the PID module, and the laser amplifier; (b) The 1560 nm laser diode and PPLN; (c) The optics before the light injected into the stable cavity.

form the lens focus. With $\Delta_2 = l_2 + \delta_2$, the final transfer matrix is

$$T = \begin{bmatrix} A & B \\ C & D \end{bmatrix} = \begin{bmatrix} \frac{2\delta_1\Delta_2}{f^2} + \frac{2\Delta_2}{R} - \frac{2\delta_1\Delta_2^2}{f^2R} - 1 & \frac{-2\delta_1}{f}(f - \frac{\delta_1\Delta_2}{f}) - \frac{2}{R}(f - \frac{\delta_1\Delta_2}{f})^2 \\ \frac{2\Delta_2}{f^2}\left(1 - \frac{2\Delta_2}{R}\right) & \frac{2\delta_1\Delta_2}{f^2} + \frac{2\Delta_2}{R} - \frac{2\delta_1\Delta_2^2}{f^2R} - 1 \end{bmatrix}. \tag{3.39}$$

According to the stability condition [88], the optical resonator is stable if $|A + D| < 2$, so the condition to keep cavity stable is $0 < \frac{\delta_1\Delta_2}{f^2} + \frac{\Delta_2}{R} - \frac{\delta_1\Delta_2^2}{f^2R} < 1$ which equals to

$$0 < \frac{\delta_1\Delta_2 R + \delta_1\Delta_2^2 - \Delta_2 f^2}{f^2 R} < 1. \tag{3.40}$$

Considering the experimental conditions $f \gg l_2 \gg \delta_2$, obviously $\Delta_2 > 0$, so $\frac{\delta_1\Delta_2}{f^2} + \frac{\Delta_2}{R} - \frac{\delta_1\Delta_2^2}{f^2R} < 1$ is satisfied, we have

$$\begin{aligned} &\frac{\delta_1\Delta_2}{f^2} + \frac{\Delta_2}{R} - \frac{\delta_1\Delta_2^2}{f^2R} > 0 \\ \Rightarrow &R + \Delta_2 > \frac{f^2}{\delta_1}. \end{aligned} \tag{3.41}$$

In conclusion, we need a concave mirror with $R > \frac{f^2}{\delta_1} - \Delta_2$ to make the cavity stable.

The TEM_{00} mode beam is Gaussian-distributed,

$$R(z) = z\left(1 + \left(\frac{\pi\omega_0^2}{\lambda z}\right)^2\right) \tag{3.42}$$

$$\omega(z) = \omega_0\sqrt{1 + \left(\frac{\lambda z}{\pi\omega_0^2}\right)^2}, \tag{3.43}$$

to get a beam waist of 10 mm on one side of the $f = 400$ mm lens, the beam waist on the other side should be 9.93 μm and the curved mirror should be placed at $l_2 = 0.05$ m with curvature $R = 0.05$ m.

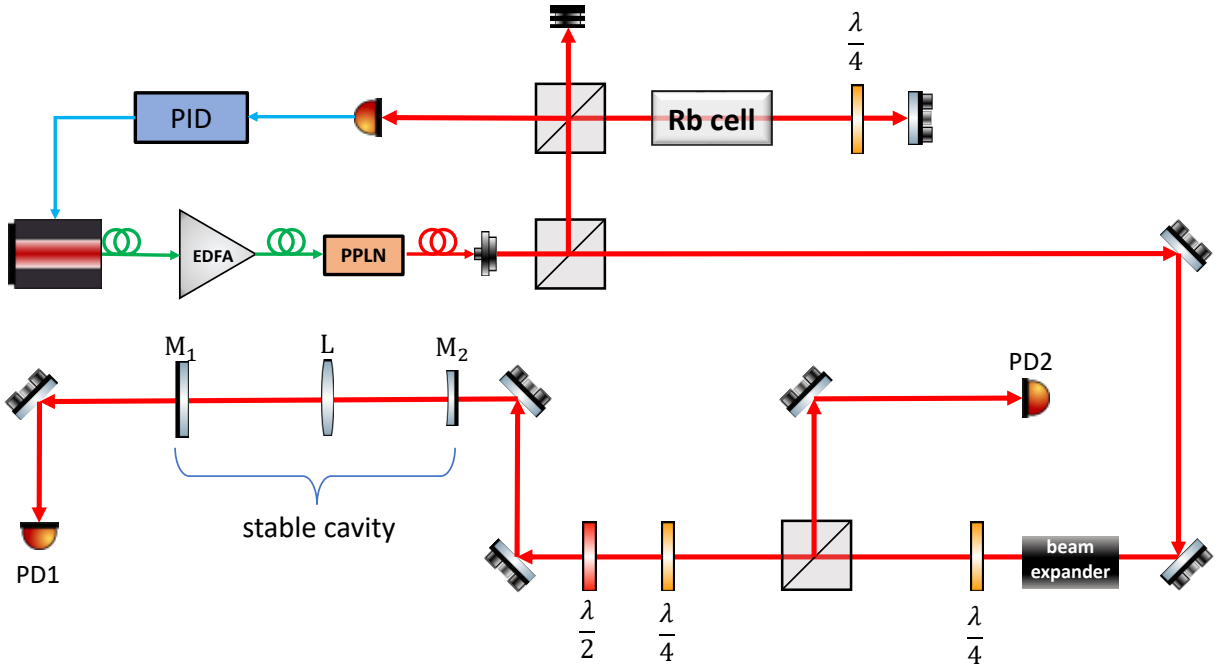

Figure 3.28: Schematic diagram of the optical path.

To test the feasibility of a stable cavity, we built a simple stable cavity to verify its beam expansion effect. We used an RIO laser diode (PLANEX 1550 nm Laser Diode), the output power of which is -6.2 dBm from the diode and 23.5 dBm after the amplifier. A Periodically Poled Lithium Niobate (PPLN) is used to double the frequency, and after the PPLN, part of the light ($< 100\mu$W) is seperated to the wavelength meter for monitoring the wavelength. By properly adjusting the temperature and current of the PPLN, we obtained about 40 mW at 780.2409 nm, the parameters we used are $T_c = 4,\ T_F = 0,\ I = 80$ mA.

The optical path is shown in Fig. 3.28. The 780 nm light is divided into two beams by PBS, one of which is used for saturated absorption spectroscopy (1 mW), and the other light is expanded by a beam expander to get the proper waist for cavity. After the beam expander, there is a third PBS for reflected signal before the beam is injected into the cavity. (Fig. 3.29).

Since the melting point of rubidium is $38°$C, most atoms are adsorbed on the glass wall in a solid state at room temperature. In order to increase the gaseous atoms in the cell, we use a film resistance heater to heat the cell, and the current of the resistance heater is kept at 0.8 A

By heating the cell and trimming the current, we get a clear saturation absorption spectrum(Fig. 3.29). In theory, we need to input the first-order or third-order differential of the spectrum into the frequency stabilization module as an error signal to lock the diode on a peak we need, but since we do not have a differential circuit here, and this test has no special requirements for the laser frequency, we have AC coupled the line and added a DC offset. And then send it to the PID module, which locks the diode on a slope of the saturable absorption line instead of a peak.

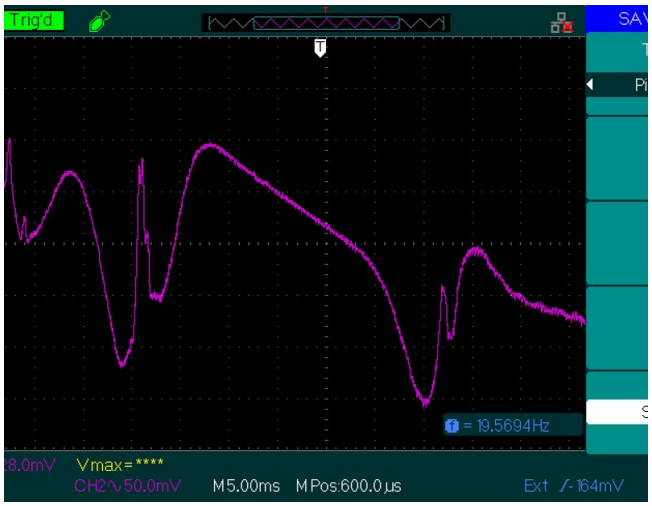

Figure 3.29: Saturated absorption spectroscopy

The following steps are performed to align the cavity and observe the signals:

1.Use a photodetector PD1 to detect the intensity of the beam $P1$ without put M_1,M_2 and L.

2. Place the convex lens L in the middle, the focal length of it is $f = 0.4$ m. Adjust the lens to make the light intensity at the PD1 reach the maximum $P2$ ($P2$ may be slightly larger than $P1$ due to the focus of the lens)

3. Place M_1 and adjust it so the PD2 for reflection spectrum can obtain the maximum intensity $P3$. 4. Place M_2 and adjust it to get the light intensity at the PD2 reaches $P3$.

5. Apply a modulation on laser current or on the M_1's PZT, the reflected signal can be seen on PD2. However, since we were adjusting M_1,M_2 according to the reflected signal, the transmitted light might be dis-aligned. we need to re-align the mirror before PD1 to obtain the transmitted signal.

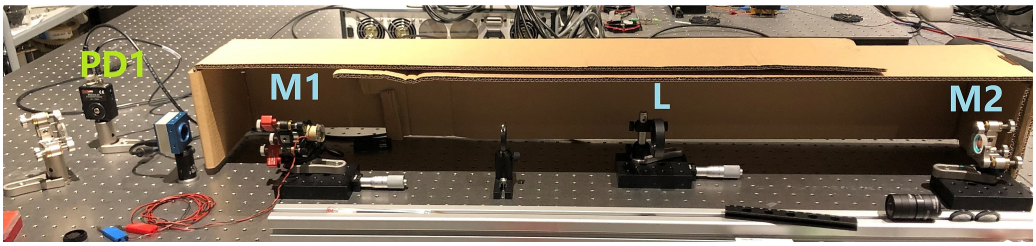

Figure 3.30: Picture of the stable cavity. PD1,M_1,L,M_2 are labeled, the aperture between M_1 and L is used for alignment and mode filtering; during the experiment, we place carboard cutouts around the optics to obstruct airflow and dampen acoustics.

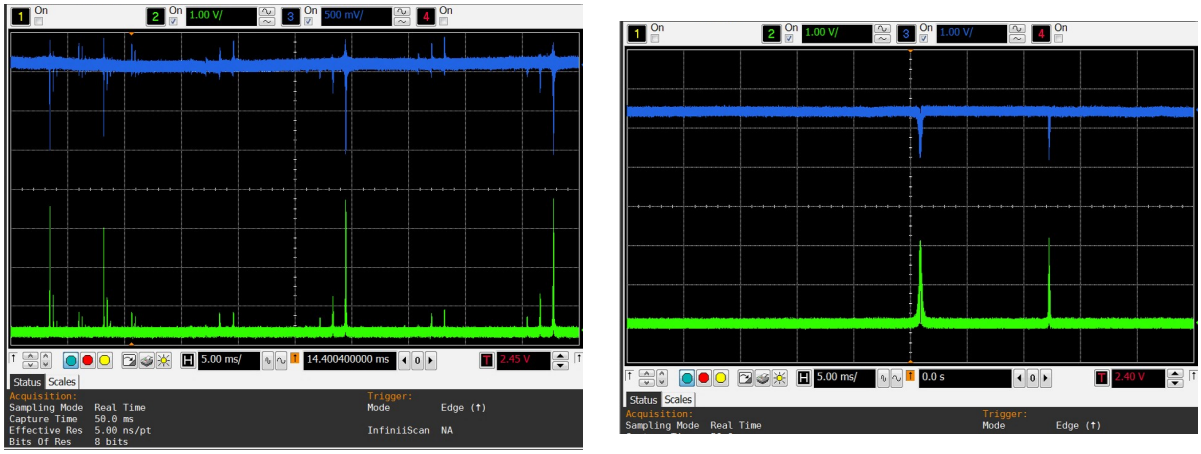

Figure 3.31: Transmitted signal (PD1) and reflected signal (PD2) of the resonator where the blue line represents the reflected signal, and the green line is the transmitted signal. Signal measured without aperture and carton (left); signal with aperture and carton added (right).

6. Fine-tune the angle and position of M_1,M_2 and L to maximize the reflected and transmitted signal. Then a cavity mode will be observed on the camera.

There are two ways of roughly determining whether a beam is in the fundamental mode

1. Observe its shape beam as Fig. 3.32 by CCD. Usually, it is a sum of multiple modes, so this is only for preliminary adjustment.

2. In the previous calculation, we said that the Gaussian distribution can be used to analyze the beam. In fact, only the fundamental mode laser is Gaussian-distributed, so we can judge the beam distribution according to the size of the beam at different positions and determine if it is in the fundamental mode, In addition, we can suppress high-order modes

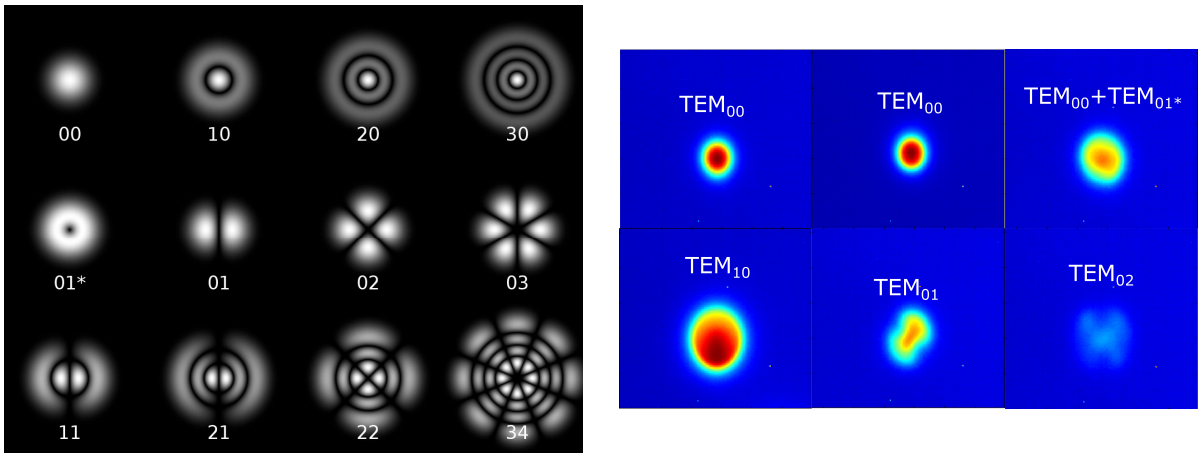

Figure 3.32: Cylindrical transverse mode patterns. (left) Diagram of the theoretical calculation. (right) Patterns observed in experiments.

by placing an aperture in the cavity (Fig. 3.31).

Since the beam diameter inside the cavity cannot be directly measured, we can only take pictures of the output light by placing CCD at different positions outside the cavity (left side of M_1), derive the beam radius inside cavity from the radius of the output light. The top three figures in Fig. 3.33 are pictures taken in three different position(125 mm,600 mm,1075 mm after M_1), the red line in the bottom images are their Gaussian fitting:

$$\begin{aligned} I_x &= a_1 e^{-((x-b_1)/c_1)^2} + d_1, \\ I_y &= a_2 e^{-((y-b_1)/c_2)^2} + d_2. \end{aligned} \tag{3.44}$$

From the fitting curve, we get two radius on x and y direction $R_x = \frac{c_1}{\sqrt{2}}, R_y = \frac{c_2}{\sqrt{2}}$, then the beam radius is:

$$R = \sqrt{\frac{r_x^2 + r_y^2}{2}}. \tag{3.45}$$

In our case they are 730 μm,1500 μm,1637 μm at these three positions. Combined with Eq. 3.43, we can calculate the fundamental mode size at 45cm after the lens is 673 μm. This is much smaller than the beam size required for the gradiometer, but bigger than 230 μm without lens.

We use this experiment to demonstrate the feasibility of a stable cavity. Compared with the stable cavity without lens, we effectively enlarge the diameter of the beam near the center point; and compared with the marginly stable cavity, It is more stable and easier to lock. However, this structure is designed for a single interferometer, and further improvements are

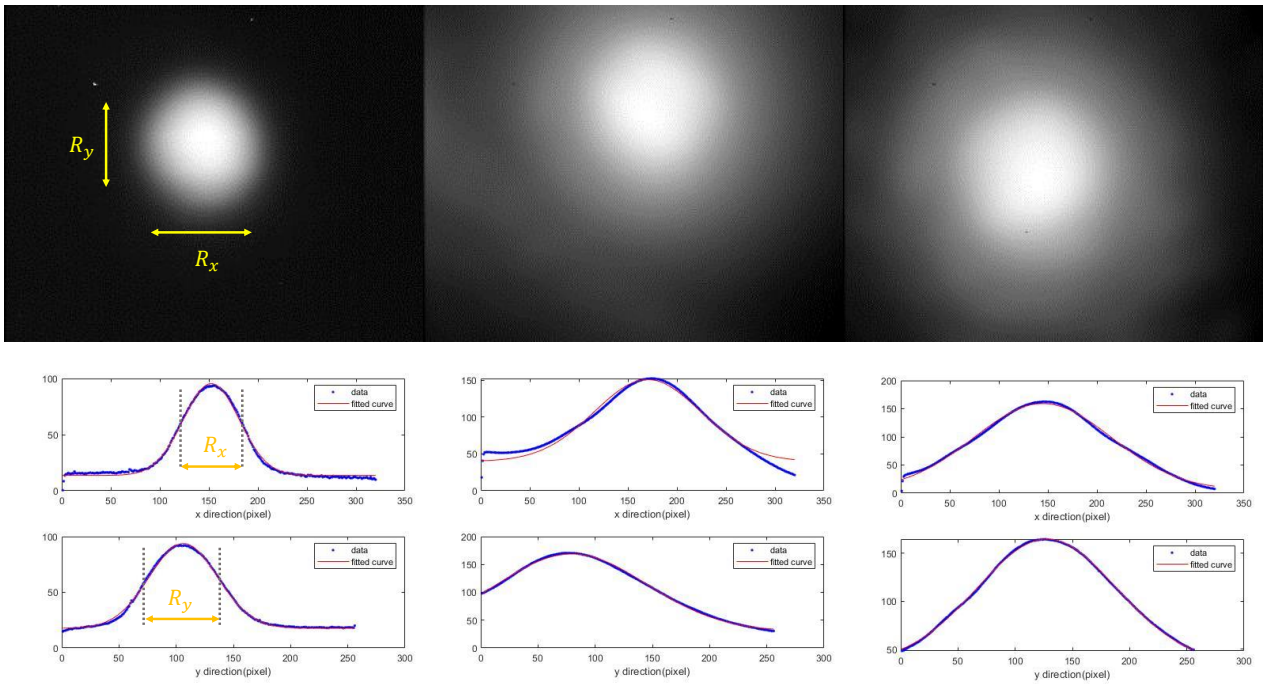

Figure 3.33: Analysis of the beam size. The top three images are the taken by the CCD at 125 mm, 600 mm, 1075 mm after M_1, and the bottom three are the beam radius obtained by Gaussian fitting in the x and y directions.

needed for the gradiometer.

Chapter 4

Preliminary results of atom gradiometer

This chapter will introduce the atom source and how we can optimize the 3D MOT, the 2D MOT, the launching and cooling process, as well as the Raman spectroscopy.

Contents

4.1 Atom source

The spatial extent of the entire atomic source is 110×89.5×81, which is included in a frame rack of 45×45 aluminum profiles. In addition, there is a 25mm thick rigid plastic plate at the bottom to install 2D MOT and 3D MOT support components. The atom source chamber is mainly composed of three parts [89, 90]: 2D MOT chamber, 3D MOT chamber, and chamber for velocity selection and detection (Fig. 4.1).

We used rubidium 87 atoms as the atomic source because the 780 nm and 1560 nm optical devices are more mature and cheaper. Rubidium atoms are released from a dispenser [91, 92] connected to the 2D MOT chamber. Due to the small apertures between the three chambers,

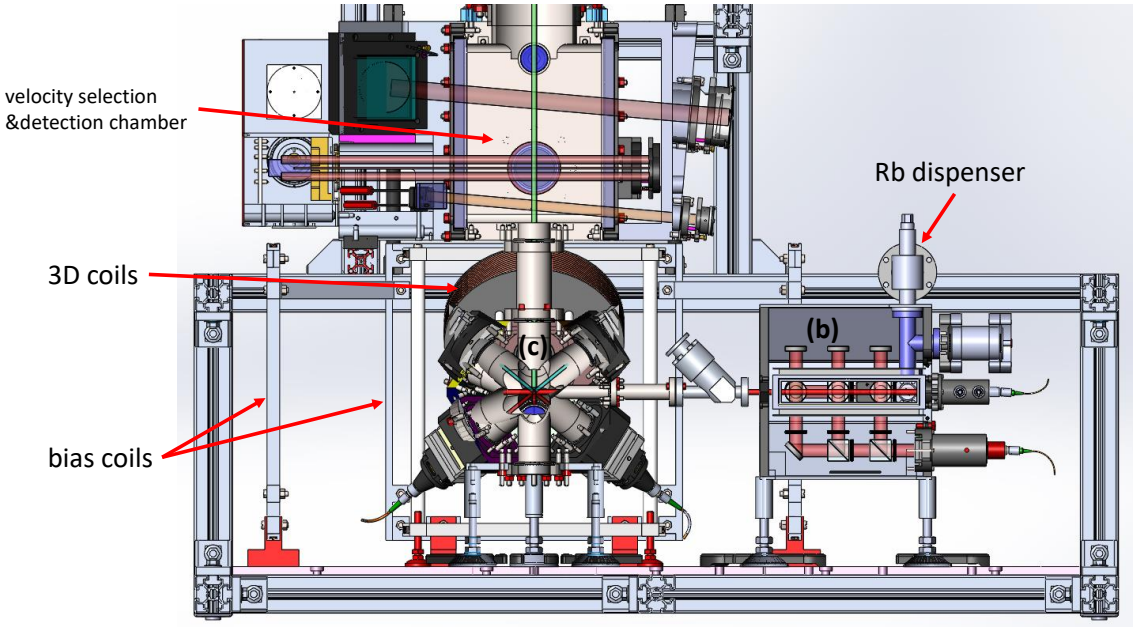

a

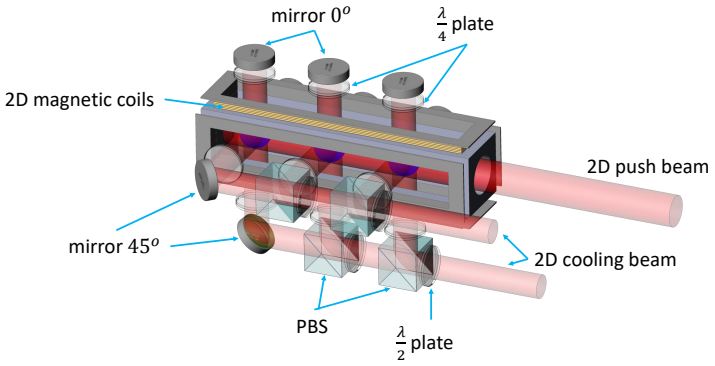

b

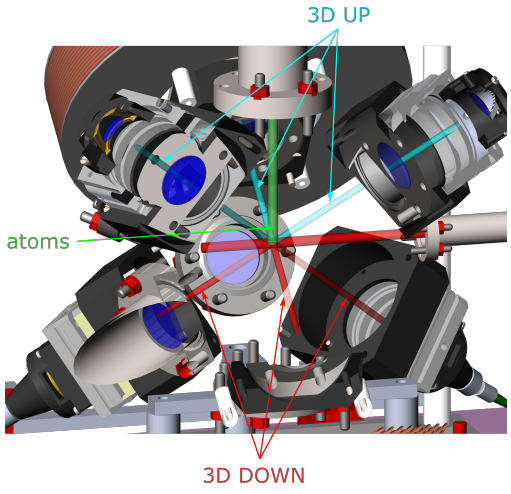

c

Figure 4.1: (a) Schematic of the atom head. (b) Details of the 2D MOT. The two cooling beams form three 2D MOTs through splitting and reflection. (c) Details of the 3D MOT. The dark red lines are 3D Down beams, blue are 3D Up beams, bright red represents 2D push beam, and the green represents atomic trajectories.

the pump group connected to the central vacuum chamber has very low pumping speed for the 3D MOT chamber and 2D MOT chamber, so these two chambers are both equipped with an ion/getter pump to ensure the UHV.

The experimental sequence can be summarized as:

- 2D MOT,

- 3D MOT,

- atom launching and cooling,

- velocity selection with Raman down beam,

- interaction with the interrogation light for pushing on F=2 or detection,

- state labeling with Raman up beam,

- pushing on F=1,

- detection.

In the rest of this chapter, I will follow this sequence to introduce our diagnosis and tuning of atomic sources.

4.2 Atom Loading

4.2.1 2D MOT

In the laser system, the 2D MOT module has three outputs– two cooling beams and one push beam. The 2D push beam pushes the atoms into the 3D MOT cavity to faster the loading of 3D MOT.

Each path of 2D cooling light is divided into three beams by two PBSs and half-wave plates (Fig. 4.1(b)), respectively forming three standing waves along the y-direction and z-direction. With the magnetic field provided by the surrounding coils, three two-dimensional magneto-optical traps are formed along the propagation direction of the push light.

Although the atomic source system has been well adjusted in the lab of SYRTE in Paris, the loading rate is significantly reduced after it is shipped to LP2N at Bordeaux and re-installed. Therefore, it requires re-adjustment of the optical path. For 2D MOT, due to the effect of free atomic diffusion, atoms can be captured at the 3D MOT in the absence of the 2D push atom,

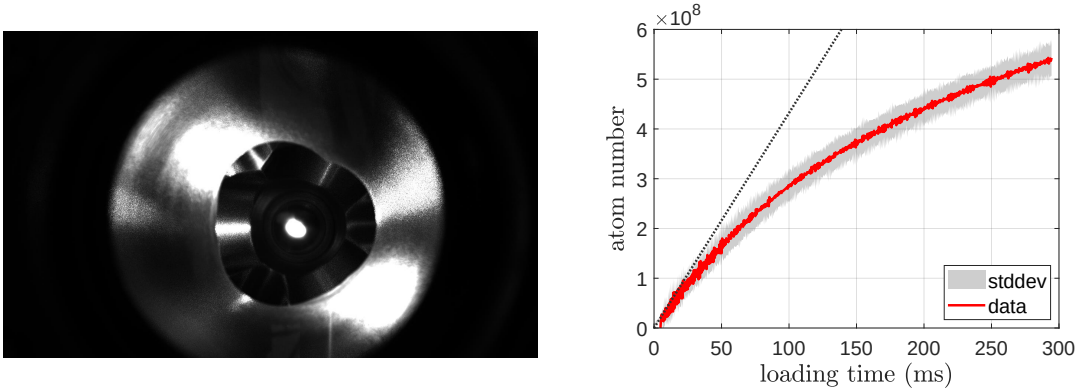

Figure 4.2: A photo of the 3D MOT taken by CCD camera (left). 3D MOT loading curve average of 500 measurements (right), the initial loading rate is 1.32×10^9/S atoms

so first, we can block the 2D push beam and adjust the 2D cooling beams according to the loading signal amplitude of the 3D MOT.

After that, the optimal loading rate is obtained by further collimating the 2D push beam. When the push beam points to the center of the 3D MOT, the signal is not enhanced but weakened because the push beam pushes away the atoms. We need to adjust the angle and light intensity of the push beam to ensure that more atoms are trapped in rather than pushed out of the 3D MOT.

4.2.2 3D MOT

3D MOT consists of six counter-propagating beams and a set of magnetic field coils, among which the three beams propagating from top to bottom are called 3D Up, and the three beams propagating from bottom to top are 3D down (Fig. 4.1(c)). In the atom trapping stage, 3D Up and 3D Down beams are at the same frequency while the 3D magnetic field remains on, forming a magnetic-optical trap to capture atoms pushed from the 2D MOT . To facilitate adjustment, we used both a CCD to observe the atoms and laser beams in the 3D MOT in real time, and a photodetector (S1337-1010BR) which detected the fluorescence emitted by spontaneous emission of atoms, and the number of photons emitted by each atom

per second is:

$$n_{3D} = \frac{\Gamma}{2}\frac{s}{1+s+(2\delta/\Gamma)^2} \tag{4.1}$$

where $\Gamma = 2\pi \times 6.065(9)$ MHz is the decay rate/ natural line width (FWHM) of the $^{87}Rb\, D_2$ line, $s = \frac{I}{I_{sat}}$ with I_{sat} being the saturation light intensity, and δ is the light detuning. The fluorescence signal per atom can be written as [93]:

$$V_{3D} = R\eta\rho\left(\frac{hc}{\lambda}\right)n_{3D} \tag{4.2}$$

where R=100 kΩ is the gain resistor in the photodetector that converts the current into the output voltage, η = 0.5 A/W is the sensitivity of the photodetector, $\rho = 1.1\%$ is the photon collection efficiency of the detection system. The photo and loading curve of the 3D MOT we get after alignment are shown in Fig. 4.2, we measure 5.3$\times 10^8$ atoms in 300 ms.

4.3 Cooling and Launching

After 300 ms, there are enough atoms in 3D MOT to begin the launching sequence, which starts by switching off the 3D magnetic field gradient. Then the 3D Up beams are blue detuned, and the 3D Down are red detuned, leading to an overall upward radiation force to push the atoms. Nevertheless, the temperature of these atoms is still relatively high at this point–near the Doppler temperature (140 μK); without further cooling, the temperature of atoms can significantly reduce the signal we detect. Therefore, we apply Sisyphus cooling [94, 95] while launching the atom.

In the analysis of the interaction between atoms and light of Sec. 2.2, we simplify the atoms to a two-level system, but the actual situation is far more complicated [94, 96, 97]. There are hyperfine energy levels in each energy level, and each hyperfine energy level also includes the Zeeman energy level. The magnetic field and optical frequency shift will cause a split between the hyperfine structure and the Zeeman energy level. For two counter-propagating linearly polarized or circularly polarized lights, the polarization direction of their superimposed field changes with the position, which forms a polarization gradient. When the light field is negatively detuned, the interaction energy between the atom's electric dipole moment and the light field is the smallest when parallel. In addition, different polarization will

cause different frequency shifts of atomic Zeeman energy levels. In the case of negative detuning, the $m_F = 0$ is the lowest level for linearly polarized light, and the lowest energy level corresponding to σ^+ is $m_F = +n$, and σ^- is $m_F = -n$, where $F = n$.

Therefore, a polarization gradient light field will form a potential energy gradient. When the atom moves slowly, its electric dipole moment will change with the polarization. If the atom moves fast that the change of electric dipole moment cannot keep up with the change of polarization, then the atom will move from the low point of potential energy to the high point of potential energy. In this process, the atoms lose kinetic energy to make up for potential energy and are thus cooled. This process is called polarization gradient cooling or Sisyphus cooling[1].

The cooling and launching process in our experiment is: First, 3D MOT magnetic field is turned off; The 3D down beams are red-detuned and the 3D up beams are blue-detuned to the resonant frequency, producing upward force on the atoms. Then, two cooling stages are performed before the atoms leave the MOT light coverage. The first stage is to change the DDS frequency to linearly increase the detuning of the 3D MOT light from -2.6 Γ to -28 Γ in 1 ms; the second stage is to linearly reduce the 3D MOT light intensity by changing the amplitude of the 3D MOT AOM's control signal. This two-stage ramp is because the potential field's height influences the minimum cooling temperature of polarization gradient cooling; by increasing the detuning and decreasing the light intensity, we are gradually decreasing the potential height to optimize the cooling effect.

4.3.1 Optimization

In addition to polarization gradient cooling, there are other sub-Doppler cooling methods, such as magnetically induced cooling and Raman cooling [98, 99], which all requires an applied magnetic field. However, in polarization gradient cooling, the presence of a magnetic field will change the displacement of the Zeeman level, thereby weakening the cooling effect. So there are three sets of coils around the 3D MOT to compensate the magnetic field in the 3D MOT chamber, the compensation coil in the x, y direction is 50 turns $\times$ 350 mm $\times$ 350

[1]The two are not exactly the same, the cooling effect in the positive detuned strong laser field is also called Sisyphus cooling

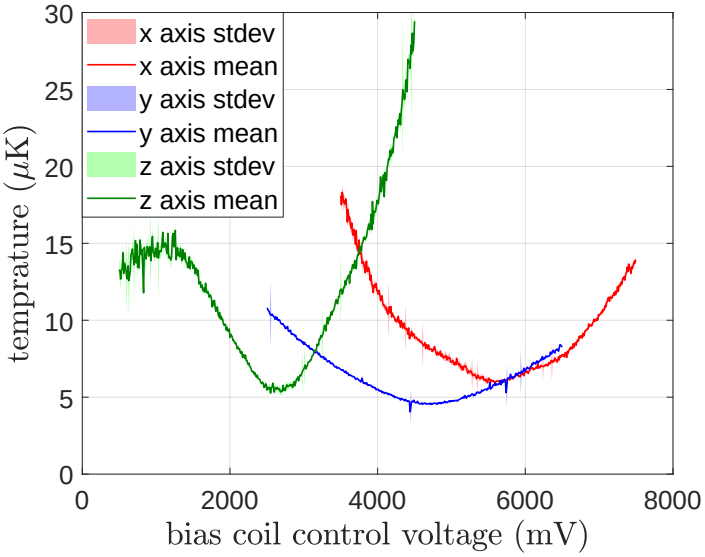

Figure 4.3: Signal optimization by changing the bias field control; The control voltage here refers to the voltage output by our DAC board, the control current corresponding to the 0 - 8V control voltage is -0.39 - 0.51 A. The compensation magnetic field generated by the coils in the x/y direction at the center is 0.97 G/A, and 1.35 G/A for z-direction coil. All data in this section, unless specified, are the average of 5 shots.

mm, 215mm from the center, and the compensation coil in the z-direction is 50 turns $\times$ 300 mm $\times$ 300 mm, 165mm from the center. By controlling the magnetic field with a circuit shown in Sec. B.4, the optimized atomic temperature can be obtained, as shown in Fig. 4.3.

When we turn off the power supply for the 3D MOT coils, the magnetic field does not shut down immediately. The current in the magnetic field coil will drop in the form of damped oscillation due to the induced voltage, and we cannot launch during this process. The longer this process takes, the higher the atomic temperature (see Fig. 4.4(a)), so we modified the magnetic field switch circuit (Appendix B) to reduce the switching time from 42.1 ms to 3 ms. After the 3D MOT magnetic field is turned off, atom launching and cooling are performed. The height of atomic launching can be adjusted by changing the relative detuning between 3D up beams and 3D down beams (6300 kHz for launching 912 mm high in our case). After that, the two-stage cooling was performed during the acceleration of atoms before leaving the 3D cooling beam. In addition to the ramp speed, the start time is also critical. If the ramp is carried out too early, the ability of the 3D beam to accelerate the atoms will

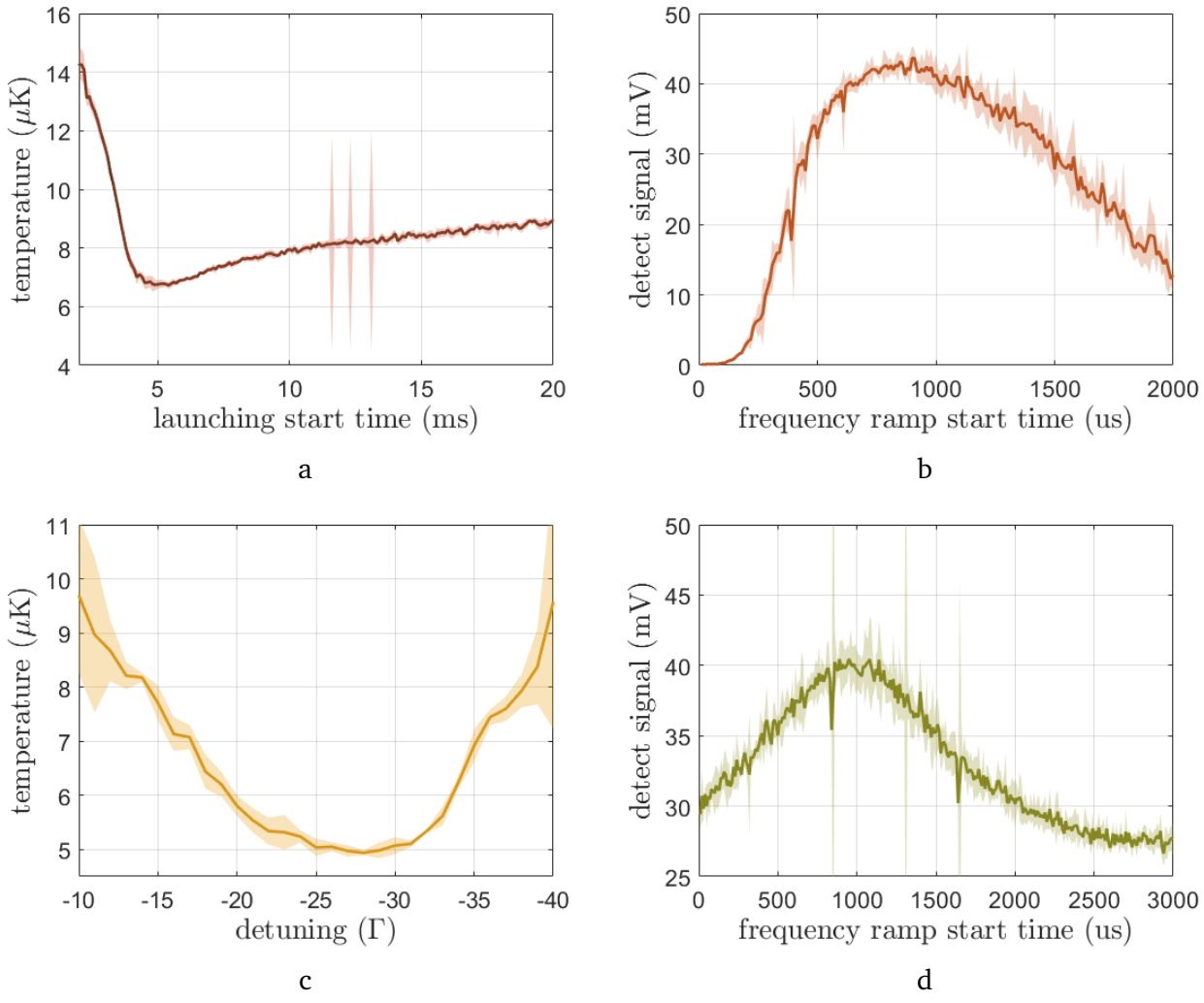

Figure 4.4: Parameter sweep optimization. (a) Scan of the launching start time after switching off the 3D magnetic field gradient; (b) Scan of the frequency ramp start time after the launching; (c) Frequency ramp state scan, ramp from -2Γ in 1 ms; (d) Scan of the amplitude ramp start time after starting the frequency ramp.

be compressed, and some atoms cannot be effectively accelerated. On the other hand, if the ramp is carried out too late, the diffusion of atoms will exceed the range of the 3D beam. Therefore, the parameter optimization (shown in Fig. 4.4) was carried out. Through optimization, we obtained atoms with 1×10^9 at/s, temperature about 5 μK before the velocity select stage.

4.3.2 Temperature calculation

We aim to reduce the atomic temperature in all the parameter optimizations of the launching and cooling processes. Lowering the temperature is reducing the average velocity of the atoms, that is, reducing the expansion rate of the atoms, in this way, when we probe, we can detect more atoms per unit time.

There are two ways to calculate the temperature, one is to calculate the atom expansion rate velocity through the width of the launching signal, and the other is to analyze the atomic velocity distribution through Raman spectroscopy. On the trajectory of the rise and fall of the atom, it will pass the position of the probe light twice. If the mirror of the probe light is not blocked, the probe light can be turned on at different times, and the signals of the atoms launching up and launching down can be obtained, respectively. The atom temperatures obtained by combining these two signals are more accurate than those obtained from a single launching down signal. The distance between center of 3D MOT and the bragg beam is 892.9 mm, according to the equation $s = \frac{1}{2}gt^2$ that the time difference between launching up and launching down (detection beam position) is around 716 ms. During the rising and falling of atoms, the detected signal peak at t_{detR} and t_{detF}; the FWHMs are t_{wR} and t_{wF}. The elapsed time in between is $\Delta t = t_{detF} - t_{detR}$, so the average velocity of the atoms when they pass the probe light is $v_{det} = \frac{1}{2}\Delta t\, g = 3.56$ m/s, which is the same for rising and falling. According to the time width of the signal t_{wR} and t_{wF} (Fig. 4.5), the distance d_{sig} traveled by the atom within the beam range can be calculated, which is the sum of the atom cloud's diameter

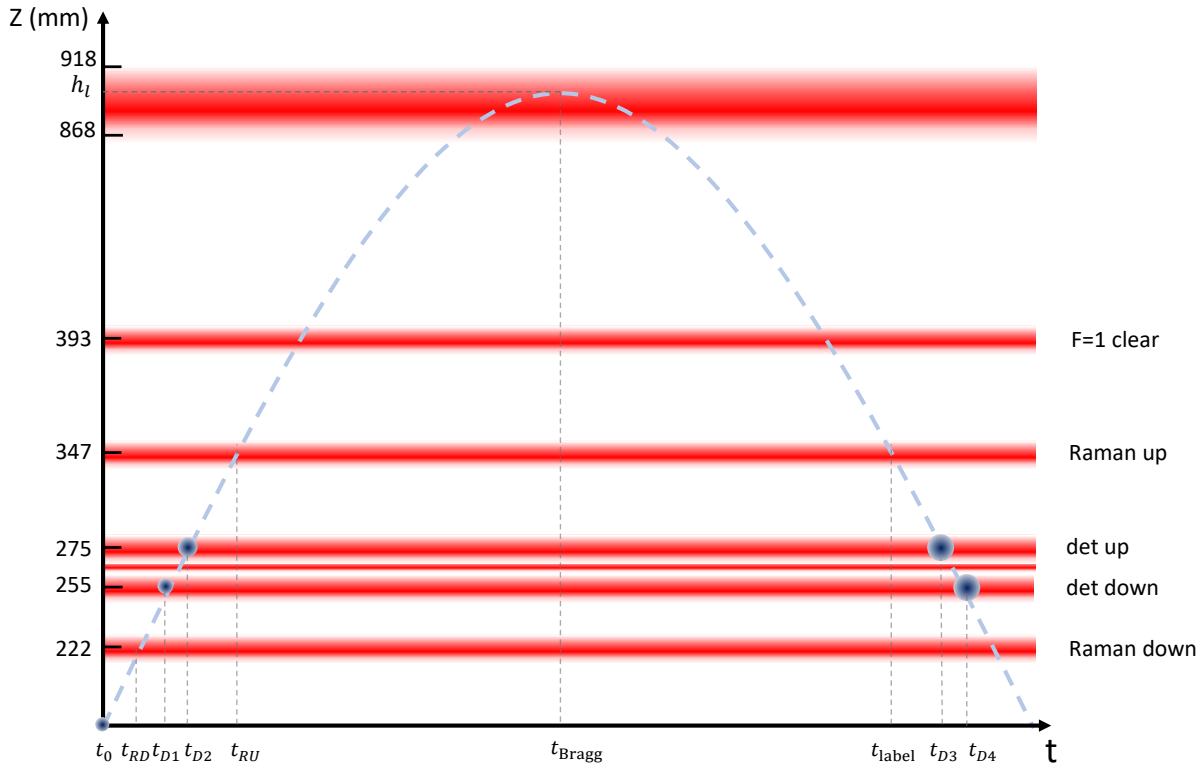

Figure 4.5: The trajectories of atoms rising and falling. We take the 3D MOT position as z=0, and moment when the atom starts to be accelerated as t=0. h_l can be adjusted by changing the detuning of the 3D MOT beam in the launching phase, and the time in this graph will also change.

$d_{atom}(t)$ and the diameter of the probe light $d_{det} = 1$ cm,

$$\begin{aligned} d_{sig} &= \sqrt{d_{atom}(t)^2 + d_{det}^2} \\ &= \sqrt{v_{dif}^2 (t_{det} - t_0)^2 + d_{det}^2} \\ &= v_{det} \cdot t_w \end{aligned} \tag{4.3}$$

where v_{dif} is the atomic expansion rate. From the two detection signals of atom rise and fall, we can obtain two sets of v_{det}, t_{det}, t_w, and solve the equation to get its expansion rate $v = 24$ cm/s, the cosspronding temperature is 5 μK.

In addition to fitting with the width of the detection signal, we can also calculate the velocity distribution of the atom according to the Raman spectroscopy, and then deduce the temperature of the atom, which we will discuss in the Sec. 4.5. the temperature obtained by both methods is close to 5 μK.

4.4 Detection

After the collimator, the detection light is divided into two beams called det-up and det-down according to their spatial positions. A photodiode detects the fluorescence intensity in the direction perpendicular to the detection beams. In the process of falling, the atoms in F=2 state are first detected and pushed away by the det-up beam, then the atoms in the F=1 state are pumped back to F=2 by the repump-det light and detected by the det-down beam.

4.4.1 Imaging system

The imaging system design is shown in Fig. 4.6, its entrance pupil aperture is 27mm, NA is 0.168.

The photodiode we use here is Hamamatsu s5870 [100]. This photodiode has upper and lower segments that can generate photocurrents separately, which correspond to the fluorescence signals of our two detection beams. where R=10 MΩ, η = 0.58 A/W $\rho = \mathrm{NA}^2 \approx 2.8\%$, also according to Sec. 4.2, the average value of the detection signal after velocity selection is $U_{det} = 1$ mV, then the flux of atoms is

$$\frac{dN}{dt} = \frac{U_{det} v_{det}}{e V_{det}} = 1 \times 10^7 (at/s). \tag{4.4}$$

4.4.2 Crosstalk

The det-up beam should only detect the atoms in the F=2 state after state labeling, and the det-down only detects the atoms in the F=1 state. The influence of other factors on the detection signal is crosstalk [101].

4.4.2.1 Fluorescence crosstalk

According to the design of the imaging system, the two segments of the photodiode should just receive the light from the corresponding detection beam, but since the distance between the two segments is only 0.03 mm, there may be some fluorescence from the other probe beam. This crosstalk is quite obvious in the atom launching up signal shown in Fig. 4.7.

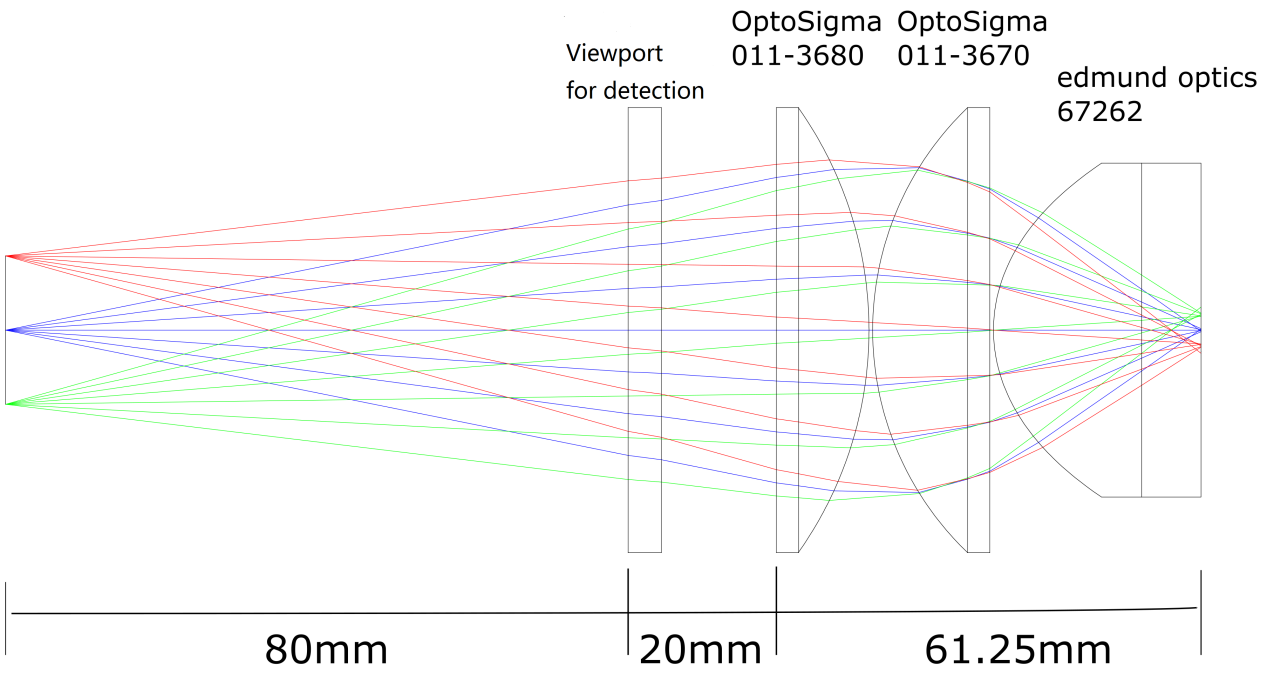

a

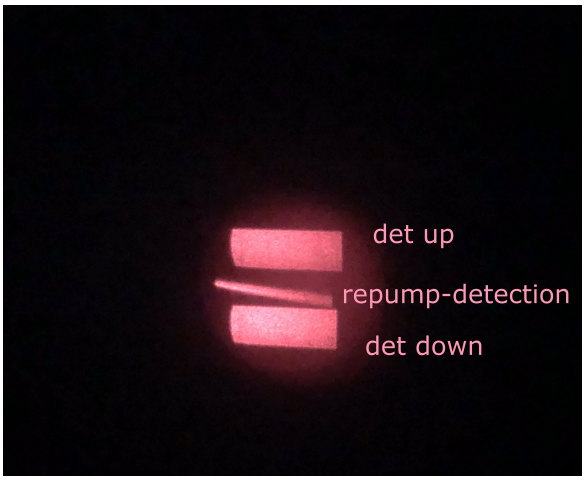

b

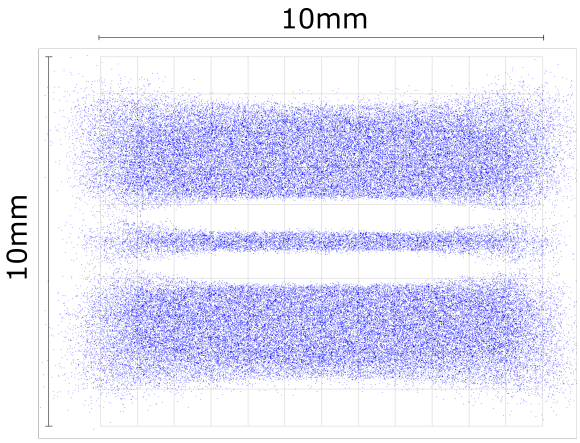

c

Figure 4.6: (a) The ray-tracing design of the detection imaging system; (b) The shapes of the detection beam and the repump-detection beam; It can be seen that the direction of the repump beam and the detection beam have a certain angle. At present, this problem does not affect our detection, but it will be fixed later; (c) The simulated projection (by ZEMAX in the range of 10 mm $\times$ 10 mm) of the detection fluorescence and the repump fluorescence on the photodiode, the blue dots in the figure represent the projection of the luminous point from the light source on the image plane; the size of a small grid is 0.83 mm $\times$ 0.83 mm.

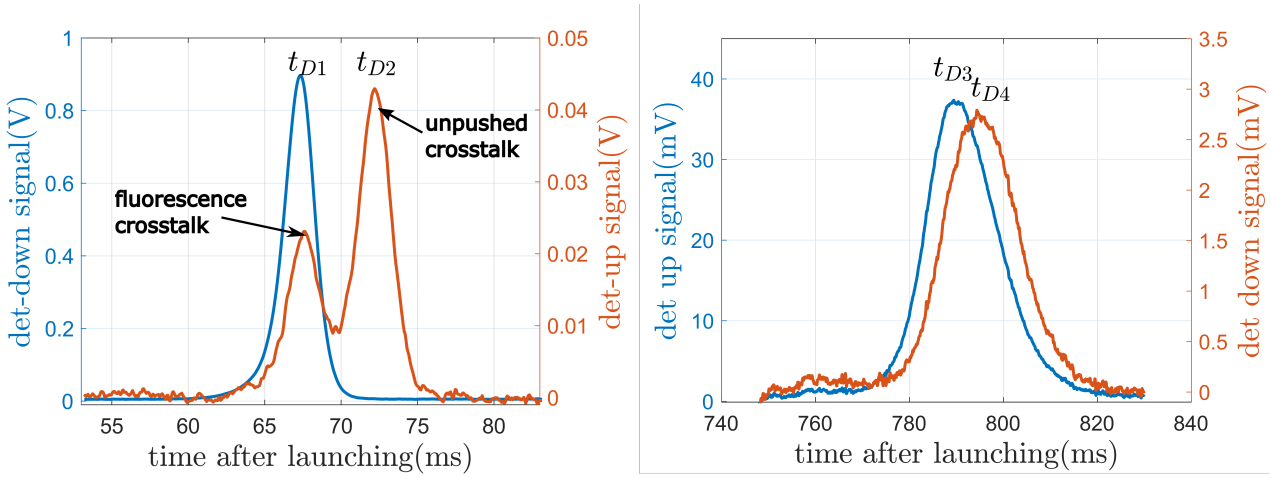

Figure 4.7: Detection signals for atoms rising (right) and falling (left) without velocity selection.

4.4.2.2 Repumping crosstalk

Another part of the crosstalk comes from the repump-detection beam between the two probe beams. The atoms at $F = 1$ are repumped to $F' = 2$ by the repump-detection light and then spontaneously radiate to $F = 2$, Fluorescence is also produced during this process, and the imaging system is not designed to avoid this crosstalk (Fig. 4.6(c)). This crosstalk is mainly affected by the intensity of the repump-detection light. Fig. 4.8(a) shows the det-up and det-down signal intensities when we transfer all the atoms to the $F = 1$ state. Theoretically, det-up should only measures atoms in the $F = 2$ state, so the det-up signal in this figure represents repumping crosstalk. One will also notice that the det-down signal drops when the control voltage is higher than 200, that is because we also block the mirror for the repump-detection beam, making it a traveling wave, which will push atoms away as the light intensity increase.

4.4.2.3 Unpushed crosstalk

According to the design, we partially block the reflection mirror of the detection beams, let its lower half become a traveling wave, and push the atoms away with proper detuning. But during the test, we found that this is not enough to push away all the atom. For this reason, we blocked the whole reflect mirror, making the whole beam a push beam. However,

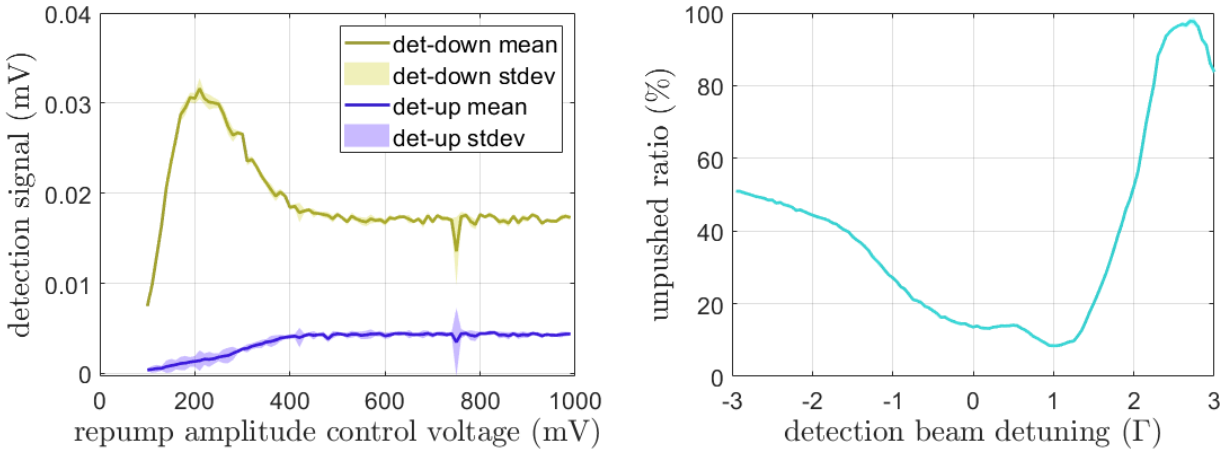

Figure 4.8: (a)Variation of detected signal with repump light intensity, all the atoms are prepared in F = 1 before the detection; (b)The change of the unpushed ratio with the detuning of the probe light in the absence of repump-det light. The unpushed ratio is the ratio of the det-down signal amplitude to the det-up amplitude when the atoms are falling.

doing so will lower our probe signal amplitude, and as shown in Fig. 4.8 there are still 8% atoms ($\Delta = 1\ \Gamma$) that were not pushed away and detected by det-down. This part is the main crosstalk in our experiment.

All three crosstalks coefficiency can be determined from multiple measurements and corrected during data processing.

4.5 Velocity selection

According to Sec. 2.3, the horizontal velocity of atoms should satisfy $v_x = n\hbar k$. Deviations from this velocity increase the distribution of atoms in momentum states which is not $\pm n\hbar k$, therefore affecting the resolution of atom interference, so an essential part of our atom source system is to select the atomic velocity through the Raman transition [59, 103, 104].

Once cooled and launched, the cloud has a Gaussian distribution and atoms are in a mixture of all Zeeman sublevels $m_F = 0, 1, 2$ of the hyperfine level F = 2 of the ground state. The goal is to select the atoms in the level $m_F = 0$ and having the horizontal speed resonant with the beam of Bragg.

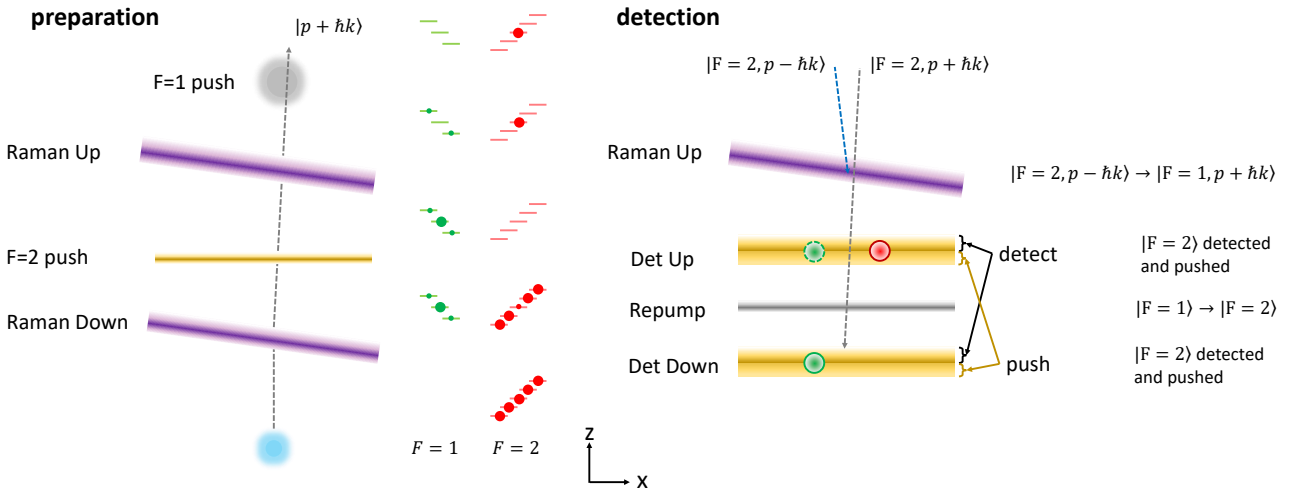

Figure 4.9: Principle of atom selection and detection [102].The left picture shows the preparation process of the atoms before rising to the Bragg beam's height and the population changes of atoms in different energy states; the right picture shows the falling detection process after Bragg scattering.

For this, we use a system composed of two Raman beams, near each of which is placed a push beam (Fig. 4.1(d)). Degeneration of Zeeman levels is generated by a homogeneous magnetic field, oriented in the direction of the Raman beams, an electric current flowing in 4 bias bars located around the experiment (Fig. 3.1). During their trajectory, the atoms arrive at the level of the Raman down beam where a Raman pulse drives a transition between the states $5^2S_{1/2}; F = 2; m_F = 0$ and $5^2S_{1/2}; F = 1; m_F = 0$. Atoms remaining in the $F = 2$ state are then pushed by a pusher beam resonating with the transition $5^2S_{1/2}; F = 2 \rightarrow 5^2P_{3/2}; F' = 3$. This beam is created by occluding the part of the detection beam in front of the retroreflection mirror, so the detection beams are split into two parts. The lower parts act as the push beams, the upper part still do the detection work.

4.5.1 Raman down

Raman down Beam and Raman up beam contain two different frequencies of light, Raman 1 and Raman 2(Fig. 3.21), the detuning of their virtual energy to $5^2P_{3/2}, F' = 1$ is Δ(Fig. 3.23) which determines the spontaneous emission rate. By changing the detuning δ of the Raman 2 frequency to $5^2S_{1/2}, F = 2$, we can choose the horizontal velocity corresponding to different Doppler frequency shifts.

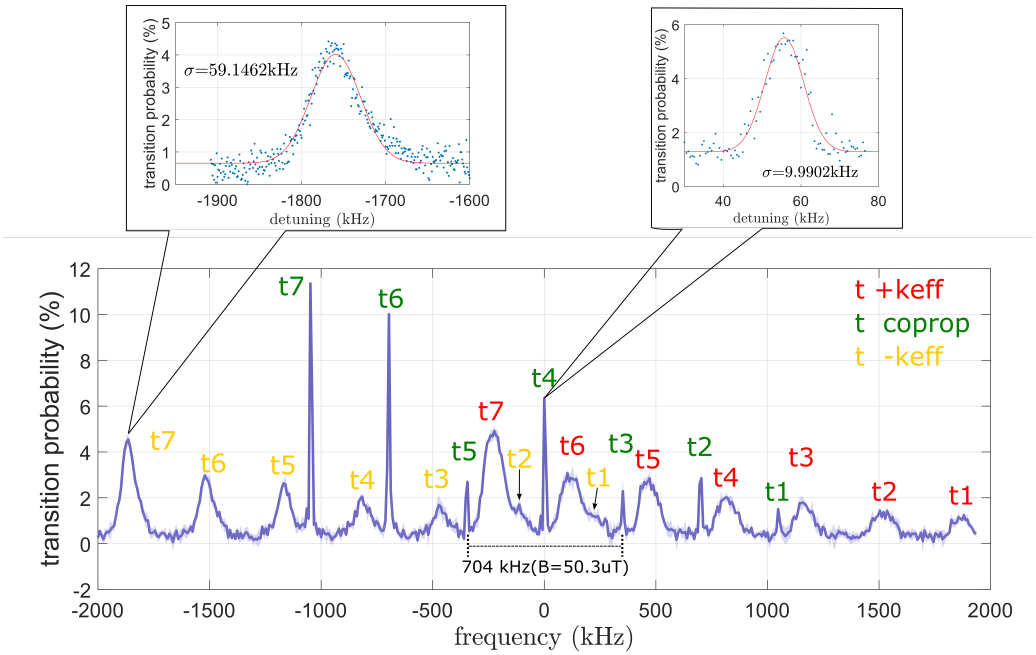

Figure 4.10: Raman spectroscopy with π-pulse time $t = 80$ μs; co-propagating transition and $\pm k_{eff}$ Doppler-sensitive transition is labeled in green, red, and yellow, with seven peaks per group, corresponding to different transition energies represented in Fig. 4.11. According to the co-propagating transition line, the equivalent magnetic field is 50.3 μT.

During the process of launching up the atoms, by applying the Raman down pulse, keeping $\Delta = 1$ GHz and making δ vary between ± 2 MHz, we obtain the spectrum of Fig. 4.10.

The incident Raman light is $\omega_{1\perp}$ and $\omega_{2\perp}$. After passing through the quarter-wave plate and the mirror, the reflected light is $\omega_{1\parallel}$ and $\omega_{2\parallel}$. If the direction of the magnetic field is consistent with the Raman light, We will only see t2, t4, and t6 transitions represented by solid lines in Fig. 4.11, but the spectrum we obtained shows all transition lines, indicating that apart from the magnetic field provided along the bias bar, the atoms are also polarized by magnetic fields in other directions. Since our atomic source is currently not magnetically shielded, a very likely source is the geomagnetic field. According to [105], the geomagnetic field where our laboratory is located is about 49 μT, inclination 60°, its projected intensity in the direction of Raman light is about 15 μT, plus the magnetic field of about 35 μT applied by the bias bar, the result is consistent with the 50 μT obtained in Fig. 4.10.

In Fig. 4.10, the width of the Doppler-sensitive transition peaks are σ=59.14 kHz and the

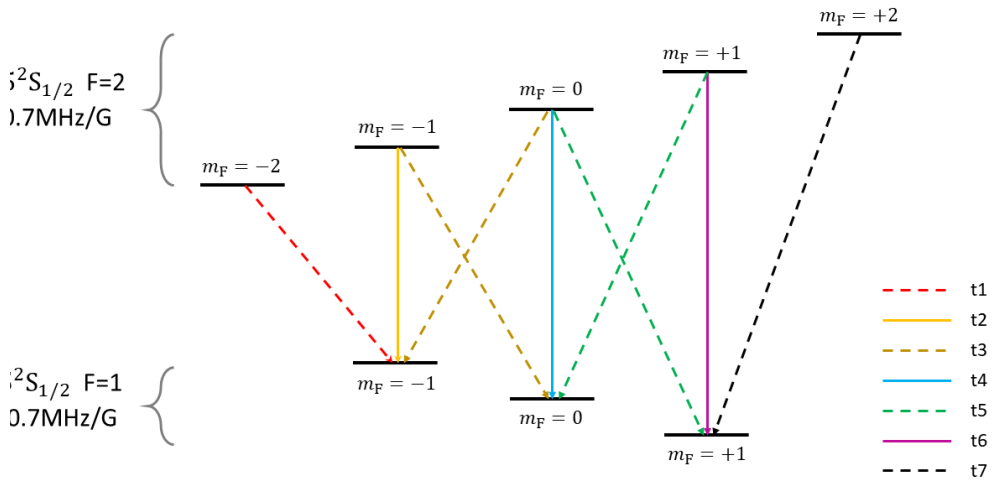

Figure 4.11: Schematic diagram of the Raman transition, where different colored lines represent different transition energies, solid lines represent transitions corresponding to linear polarization, and dashed lines represent transitions excited by circular polarization.

widths of co-propagating peaks are σ=9.90 kHz, the equivalent temperature should be [106]

$$T = \frac{m\sigma_v^2}{k_B} = \frac{m\sigma_\nu^2\lambda^2}{4k_B} \approx 4.97\ \mu K, \tag{4.5}$$

so we know that the atomic temperature before velocity selection is about 5 μK, and the temperature of the atom in the horizontal direction after velocity selection is 149 nK. By changing the light intensity, the time of the Raman π pulse can be changed. The pulse time is 80 μs and the corresponding pulse frequency width is 12.5 kHz in our case.

4.5.2 Raman up

After the velocity selection with Raman down beam, Raman up beam transfers the atoms from $F = 1$ back to $F = 2$ when atoms are rising. In order to obtain a higher transition probability, a shorter Raman up π-pulse time $t = 40$ μs is used. Similarly, in the falling phase of the atom, the Raman up beam is applied to pump the atom in the state of $|F = 2, -\hbar k\rangle$ back to $|F = 1, +\hbar k\rangle$ for detection.

Different velocity components can be selected by changing the detuning of Raman down, and the corresponding resonance frequency and maximum transition of Raman up will also

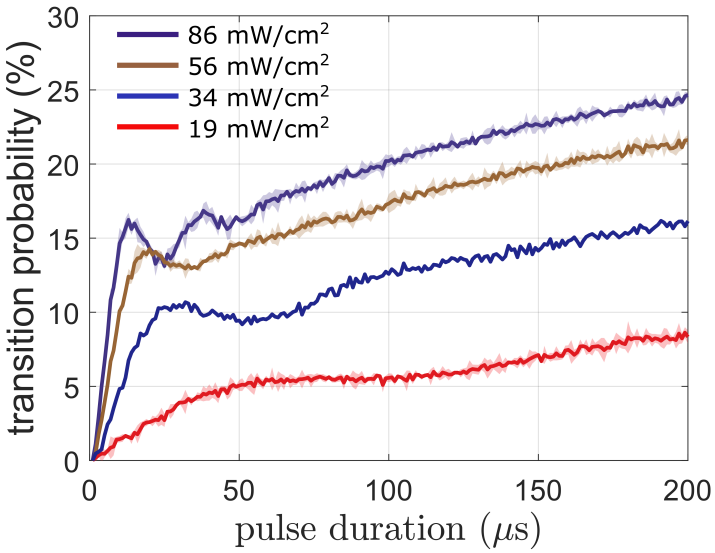

Figure 4.12: The transition probability varies with pulse duration under different Raman down power, with $\Delta = 1$ MHz, δ=851 kHz.

change. For example, Fig. 4.13 shows the change of the Raman down spectrum after select the velocity distribution near the $F = 2, m_F = 0 \rightarrow F = 1, m_F = 0$ transition with Raman down.

Fig. 4.14 shows the difference in pulse duration and transition ratio of the Raman up beam transition during atom rising versus falling. Compared with the atom rising process, the size of the atom cloud is wider during the falling; the Gaussian radial distribution of the beam power makes the atoms in different positions experience different light intensities when applying π-pulse, so the larger the size of atomic cloud, the lower the effectiveness of π-pulse

4.6 Summary

After all these tests, we are confident that we can get a particle flow of 1×10^7 at/s after the velocity selection, and are ready for the Bragg scattering test, some other possible attempts include adding magnetic shielding to increases the efficiency of the Raman transitions.

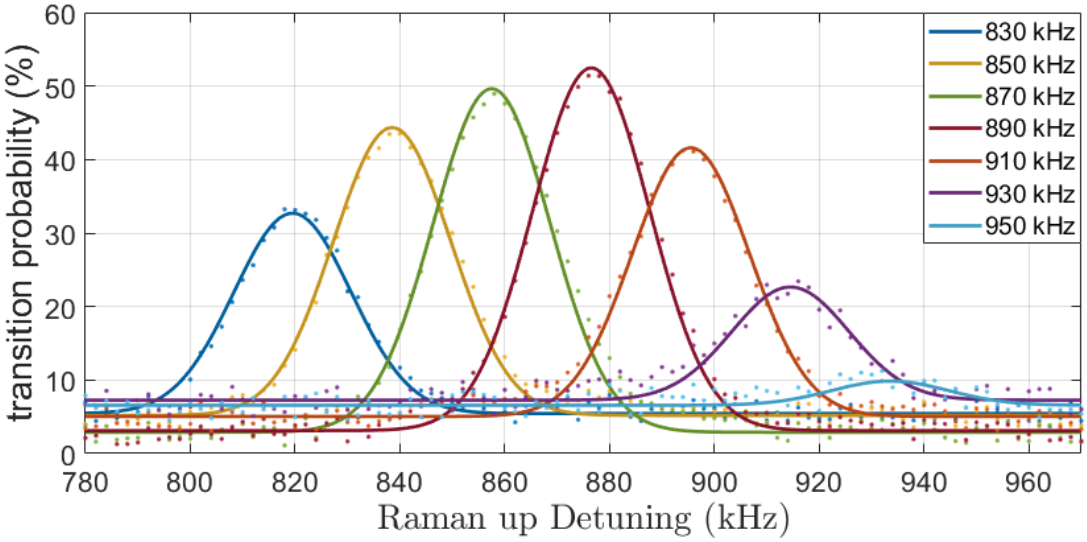

Figure 4.13: Raman Up spectroscopy of different resonance frequencies obtained by changing the Raman down detuning (830 kHz- 950 kHz) to select different atomic velocities; A Gaussian fit for each peak is also given for ease of analysis.

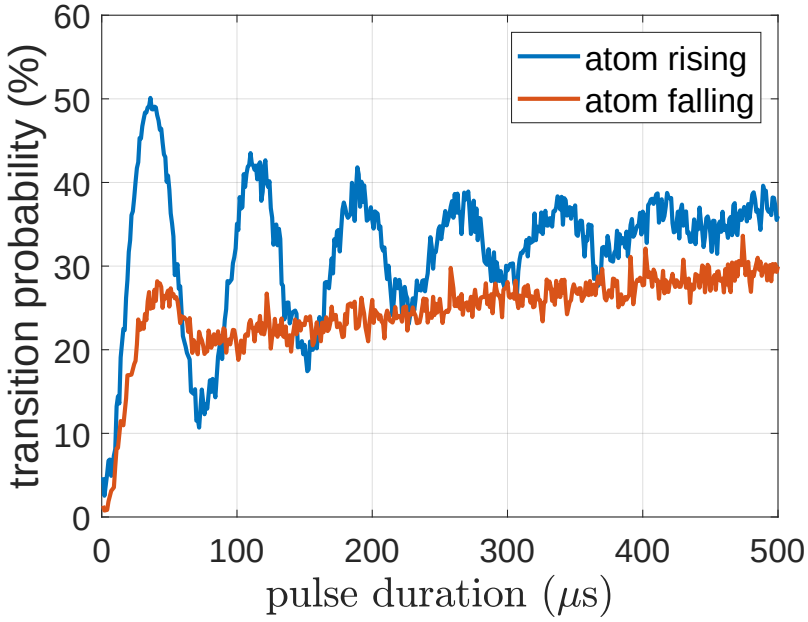

Figure 4.14: The transition probability of Raman up beam with P=21 mW/cm^2 as a function of pulse time after velocity selection. The two lines represent the application of Raman up pulse during the rising and falling phases, respectively.

Chapter 5

Conclusion

5.1 Summary of the work in this thesis

This thesis first discusses the theoretical principles of gravitational wave measurement. On this basis, we calculated the correspondence of the optical field phase at each position of the optical resonator to the GW, compared the difference between the measurement using atom interferometry and optical interferometry, and then led to our goal: to fill the gravitational wave measurement gap in the 0.1Hz to 1Hz range by building gravitational wave antennas. In addition, we present a possible method to improve the accuracy of gravitational wave measurements utilizing optical resonators. The structure we proposed utilizes the optical resonator to amplify the phase signal by $\frac{F}{\pi}$ and uses two resonators to form a "three-cavity" system whose characteristics are closer to the optical interferometer but not limited by the quantum standard limit. Therefore, it can achieve higher sensitivity in the low-frequency range.

In terms of experiments, we completed the assemble of a Rb atom gradiometer. We completed the hardware assembly and software debugging of the control system, optimized the code loaded in the DDS board state table and the control code of the 8-channel DAC output board, For the vacuum of the system, through pump group and three baking experiments, the vacuum level of the vacuum chamber with a length of 6.35m and a diameter of 0.5m reached 1.4 $\times 10^{-9}$ mbar, and closed the gate valve and the pump group, the vacuum is kept stable only by the ion/getter pump. At the same time, we have completed the test of two sets of laser systems, one of which has been tested with the first atom source system and produced a Raman spectrum with a 1×10^{7} at/s atom flux, and the other needs to be tested with the second atom source system.

In addition, we also conducted a stable cavity simulation experiment, built a 1m long stable optical cavity, and used PZT to lock the cavity to verify its amplification effect on the beamwidth.

In the current state, our experimental setup is nearing completion. The remaining work

consists of testing the second atomic head and adjusting the Bragg beam.

Unfortunately, we have not been able to obtain the gradiometer signal using two atomic sources due to the late arrival of the second atomic source.

We have also overcome many difficulties that were not expected (the biggest one is COVID) and built a prototype of the atomic gradiometer from scratch. However, there is still some work to be done before obtaining the gradient signal, and with the sensitivity of our current gradiometer design, achieving the goal of gravitational wave measurements is still a long way off. Nevertheless, we have better understood atomic interferometers, gradiometers, and the related physics in this process.

5.2 Prospects

After testing the second atom source, we will be able to get some exciting signals about the atom gradiometer and try to use the existing boom in the lab to move some massive objects to verify the gradiometer sensitivity.

In future MIGA projects, we can try techniques such as continuous atomic beam, large momentum state transfer, and squeezed state to further improve the measurement's sensitivity. As a result, we will be able to study different technologies to develop in the future GW detector based on matter-wave interferometry. In the community of MIGA project, through the cooperation of multiple projects in Europe, a research network (ELGAR [27]) for gravity, gravitational waves, and atom-interferometers will be formed.

This thesis focuses primarily on the measurement of gravitational waves. However, there are many other applications of atom gradiometers and related techniques, including gravity gradient measurements and atomic experiments for dark matter and gravity exploration in space (AEDGE)[23].

Appendix

Appendix A

D2 line

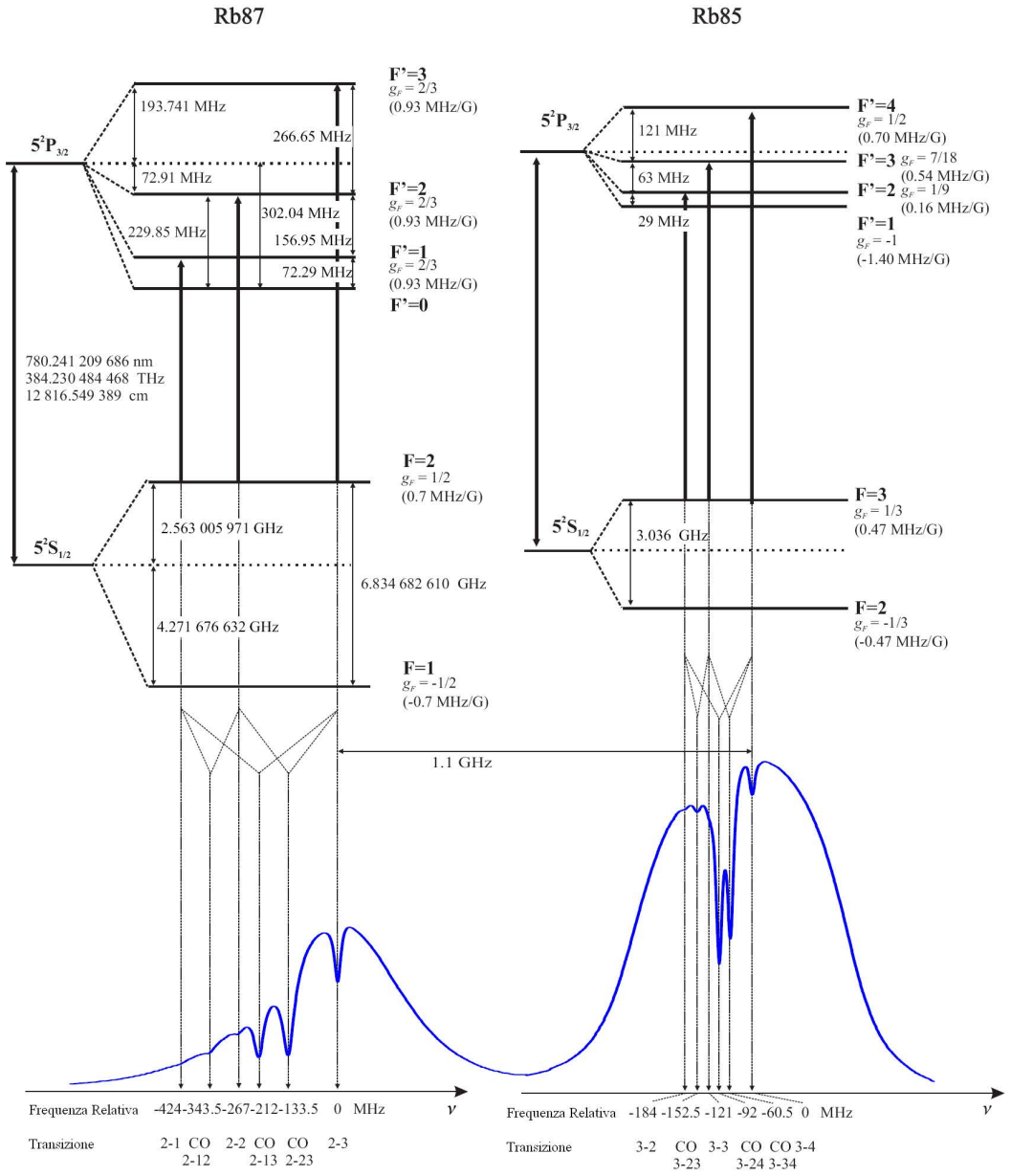

Figure A.1: Rubidium D2 transitions[107] from the upper hyperfine-level of the ground state. Indicated are transition frequencies, information about the levels and below the corresponding saturated absorption spectroscopy signal. The indications for the Zeeman shift need to be multiplied by the m_F quantum number.

Appendix B

Circuit

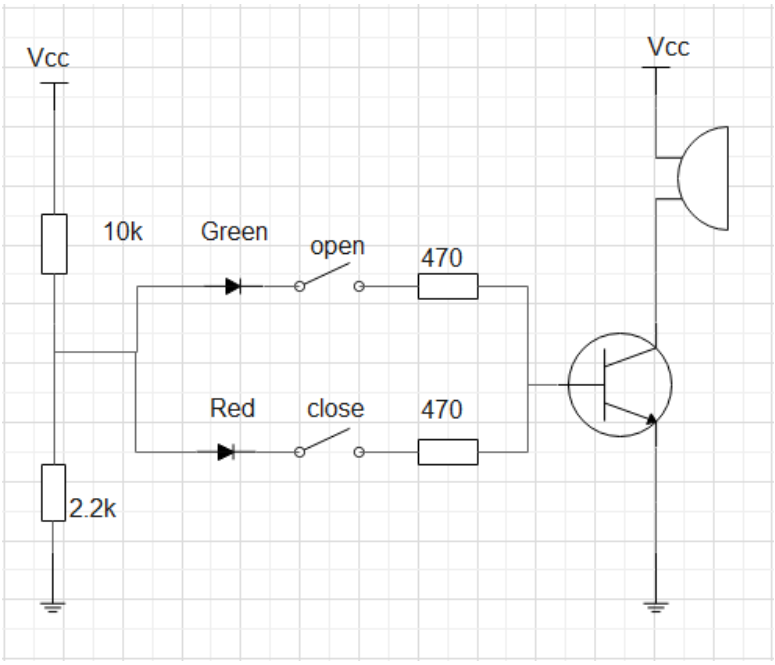

Figure B.1: CF200 gate valve control circuit.The two state switches "open" and "close" are the outputs of the gata valve.

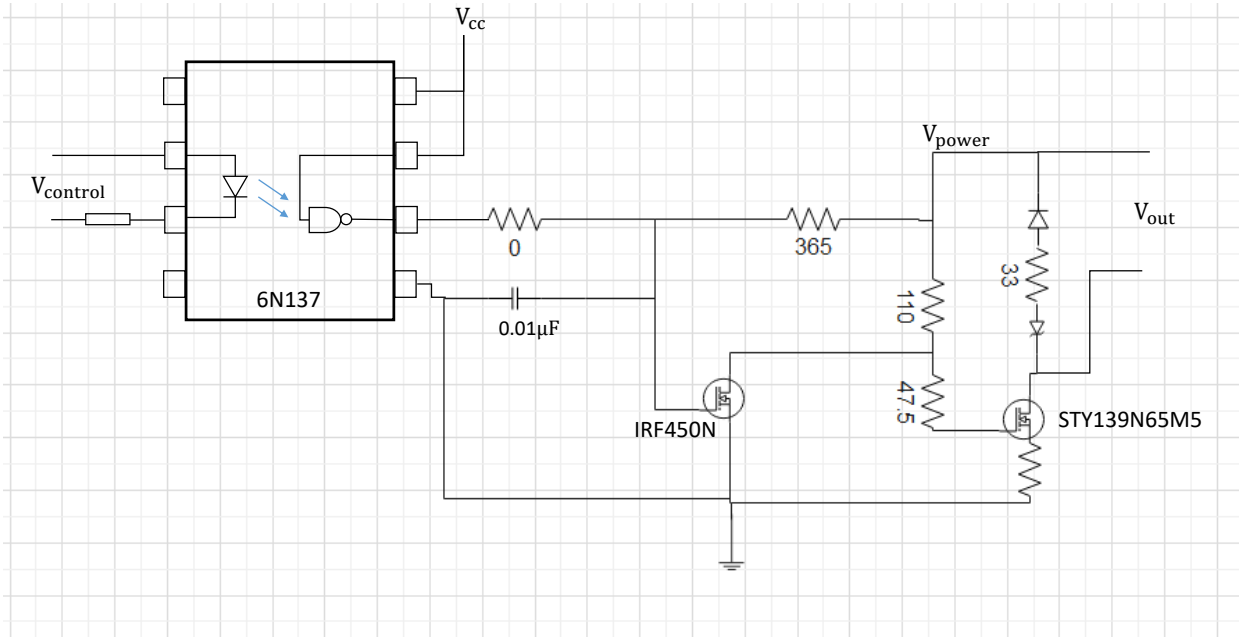

Figure B.2: MOT coil switch circuit; The resistance between the two diodes at the output determines the off time.

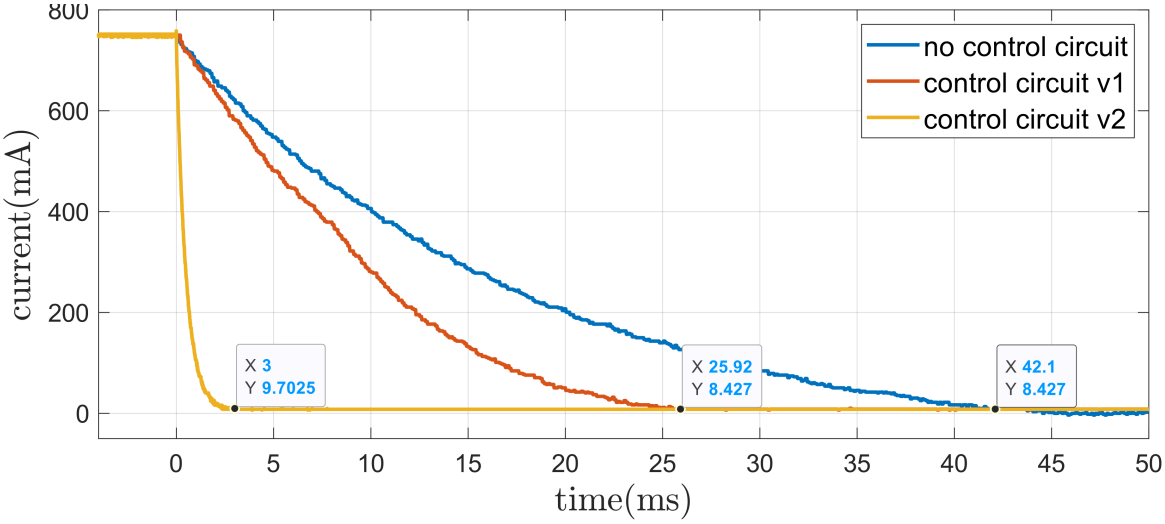

Figure B.3: After the power is turned off, the current in the 3D MOT magnetic field coil changes. The three curves correspond to the circuit without turn-off (red), no resistance (yellow) between the two diodes at the output end in the turn-off circuit, and a 33 Ω resistor in series between the diodes (blue) case.

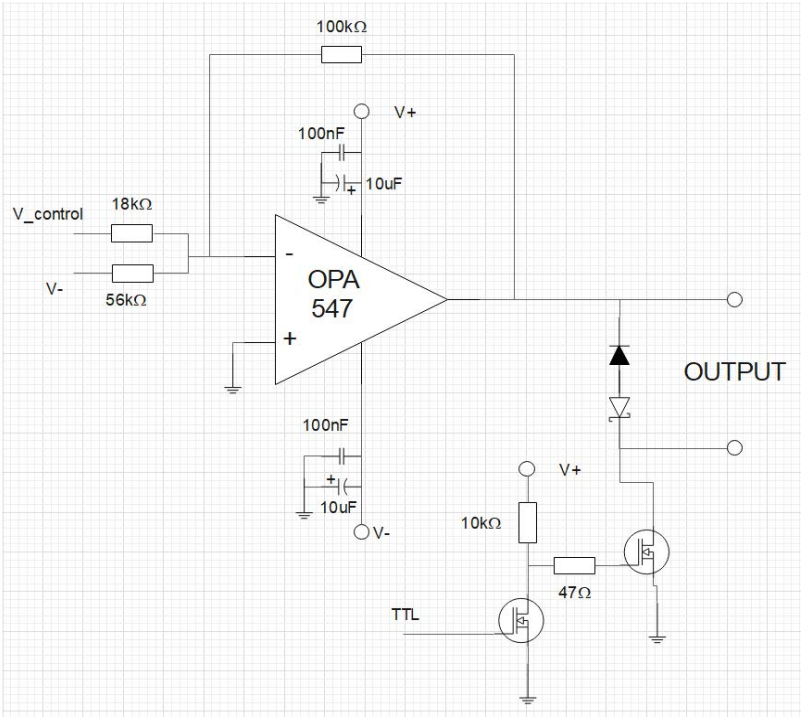

Figure B.4: The sketch of control circuit of the bias magnetic field coils. Compared with 3D MOT coils, the magnetic field current required by bias coils is much smaller, and there is no requirement for its turn-off time, but the current in each direction needs to be controlled by analog signals for precise adjustment of 3D The center of the MOT, so we designed the bias coils control.

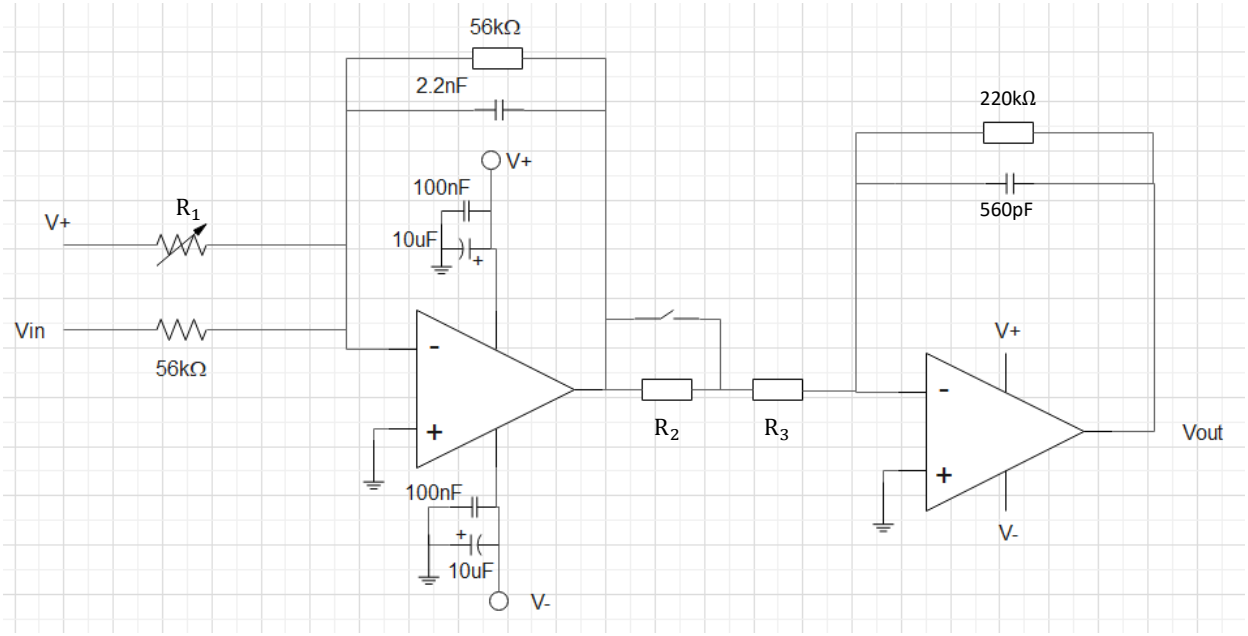

Figure B.5: Signal amplifier circuit for redpitaya designed by Joseph JUNCA. In 3.2.2.4, it is explained that in order to obtain better signal resolution, it is necessary to amplify the signal and increase the bias, so that the peak-to-peak value is as close as possible to ± 1V, and there are two cases during measurement, The atomic upward flight stage and the falling stage, the signal amplitudes of these two stages are very different, so our circuit also designed two amplification gears.

Appendix C

Design

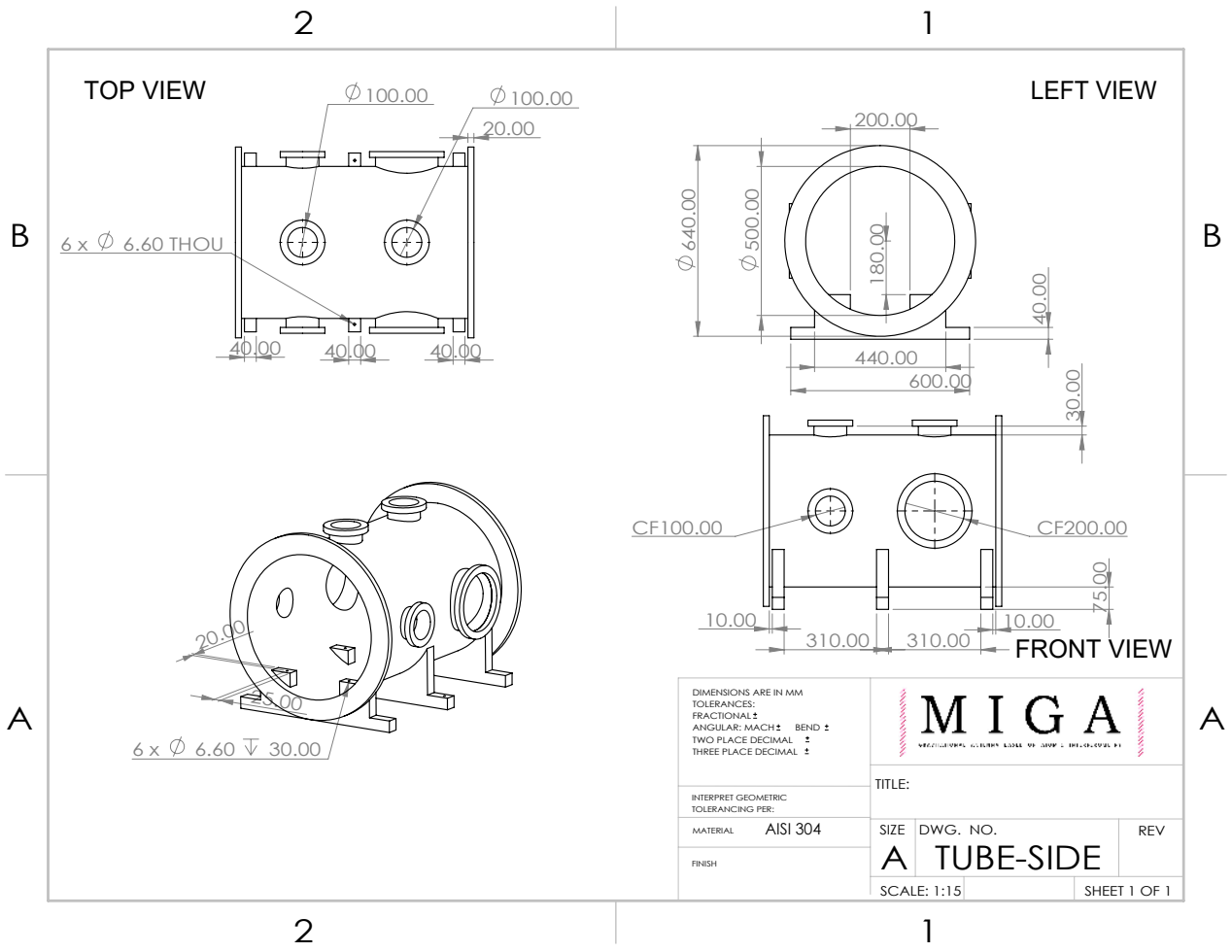

Figure C.1: Design of optical chamber

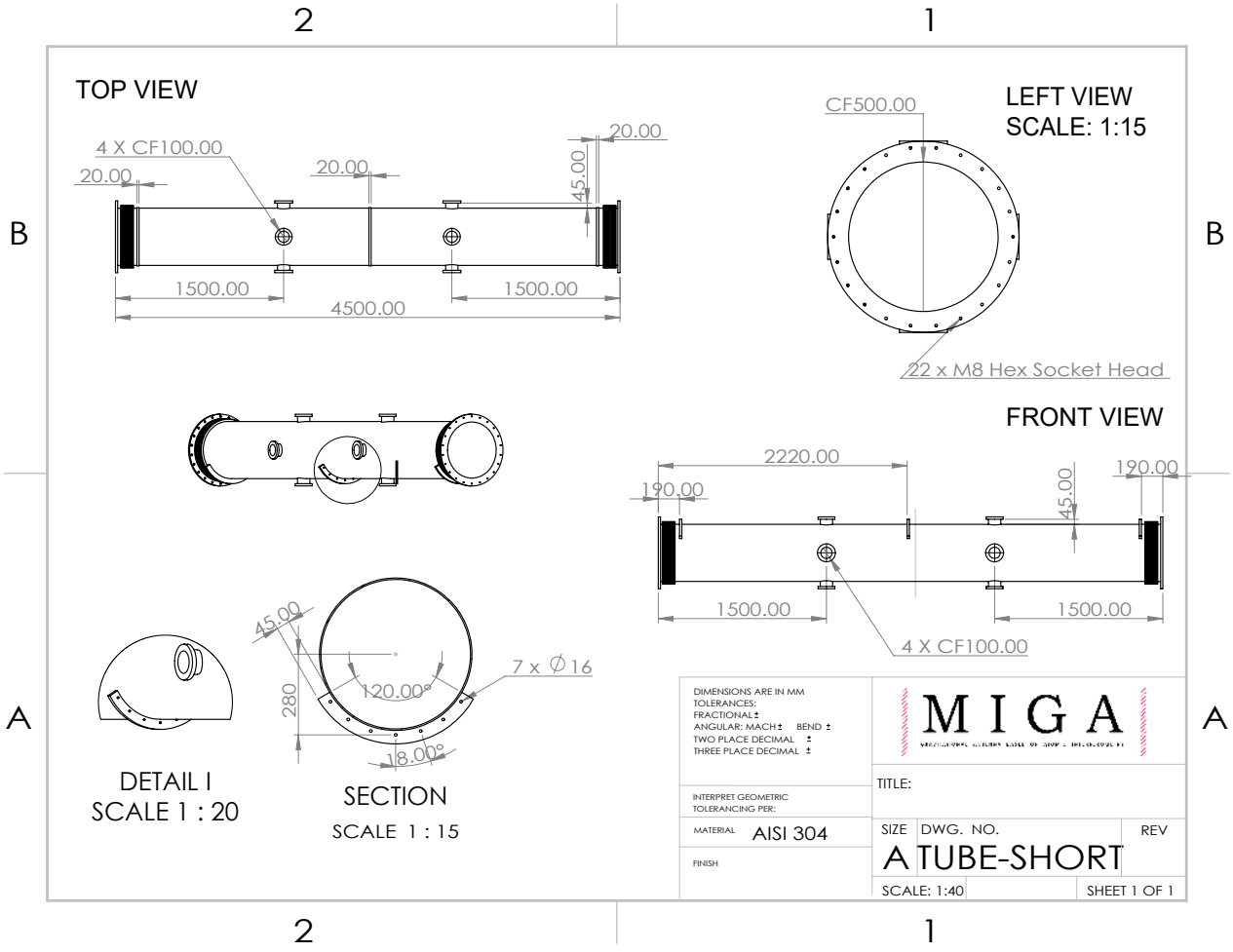

Figure C.2: Design of central chamber

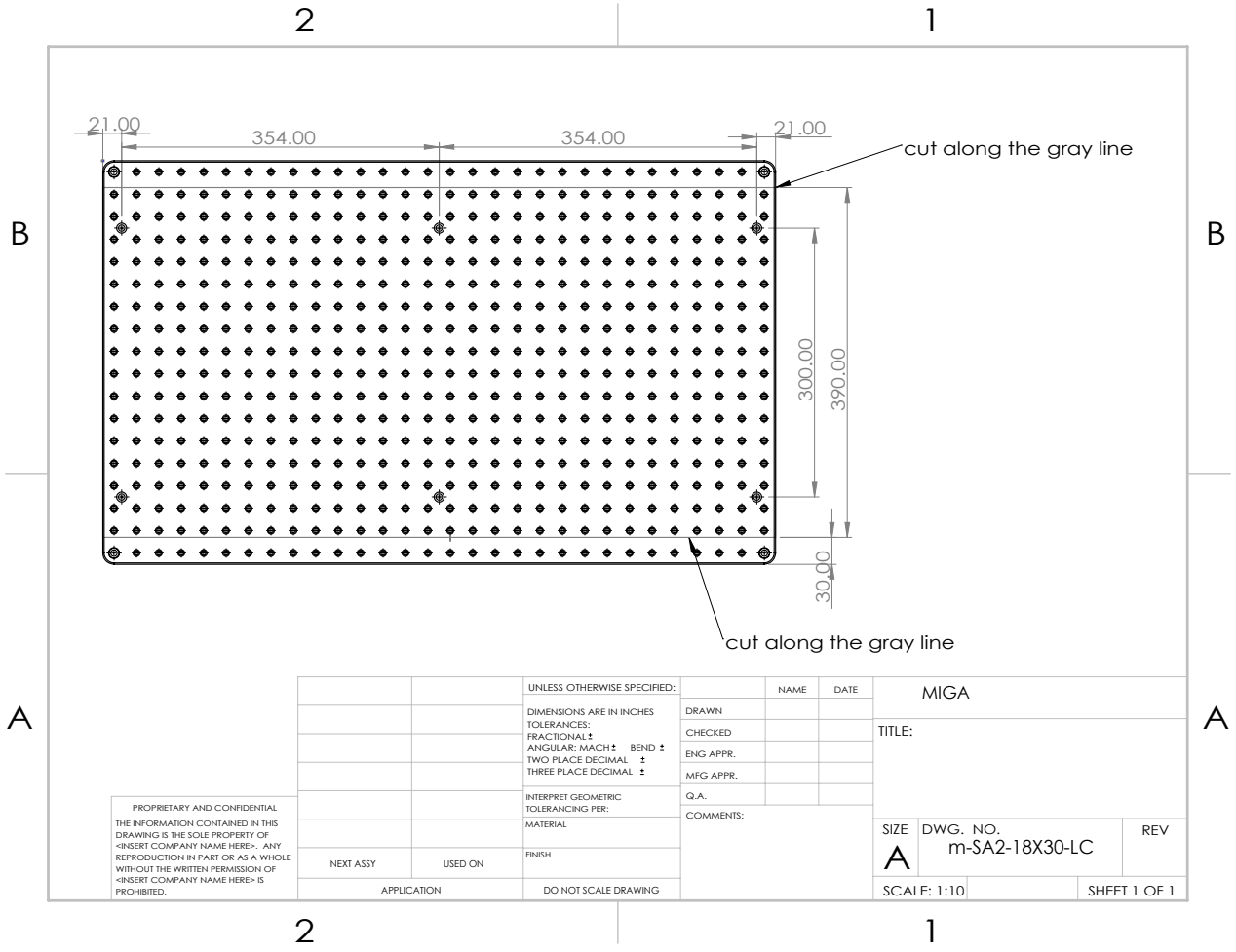

Figure C.3: Design of breadboard inside the vacuum chamber

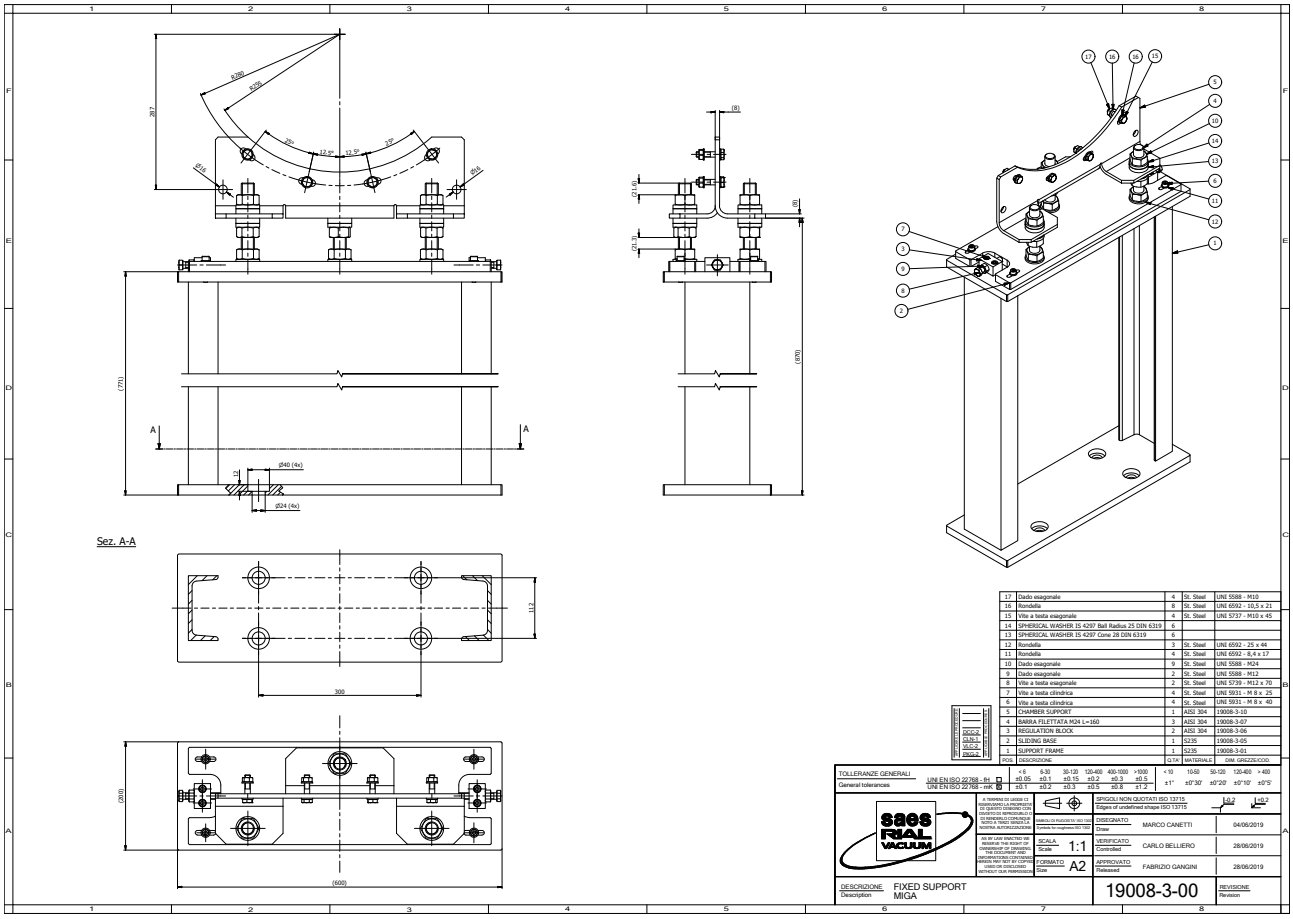

Figure C.4: Design of the fixed support for central chamber

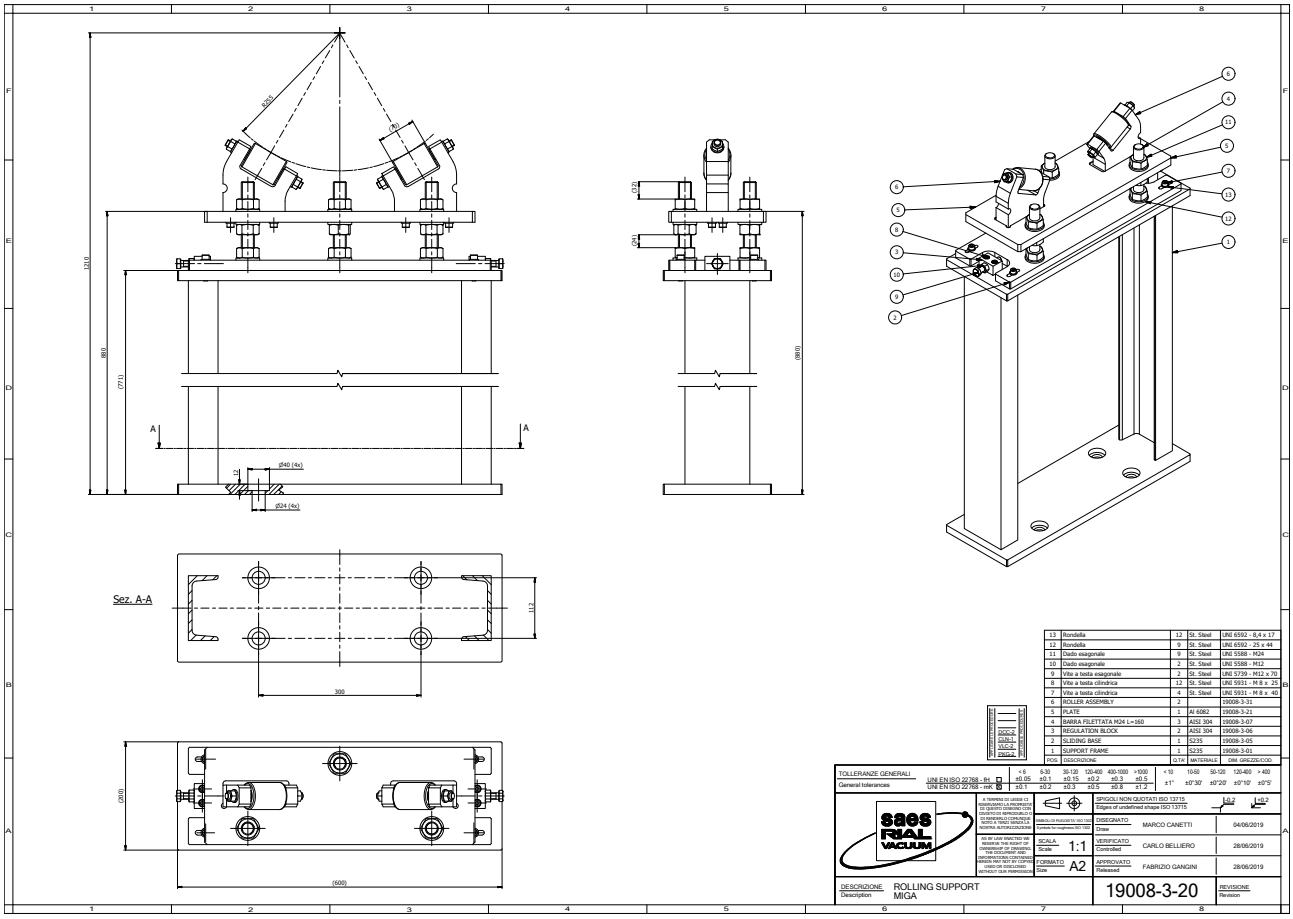

Figure C.5: Design of the support with pulley for central chamber

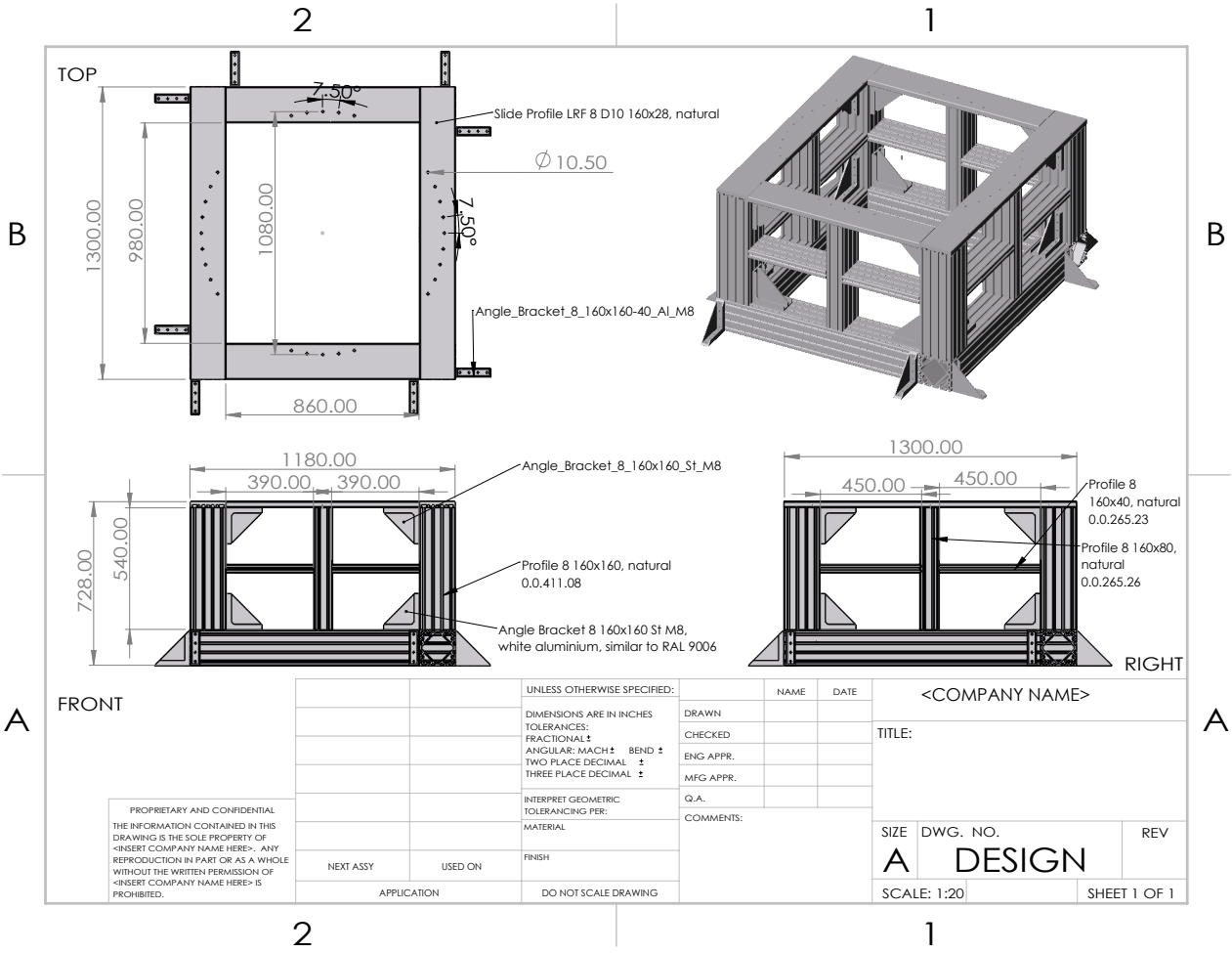

Figure C.6: Holder for optical chamber of MIGA project

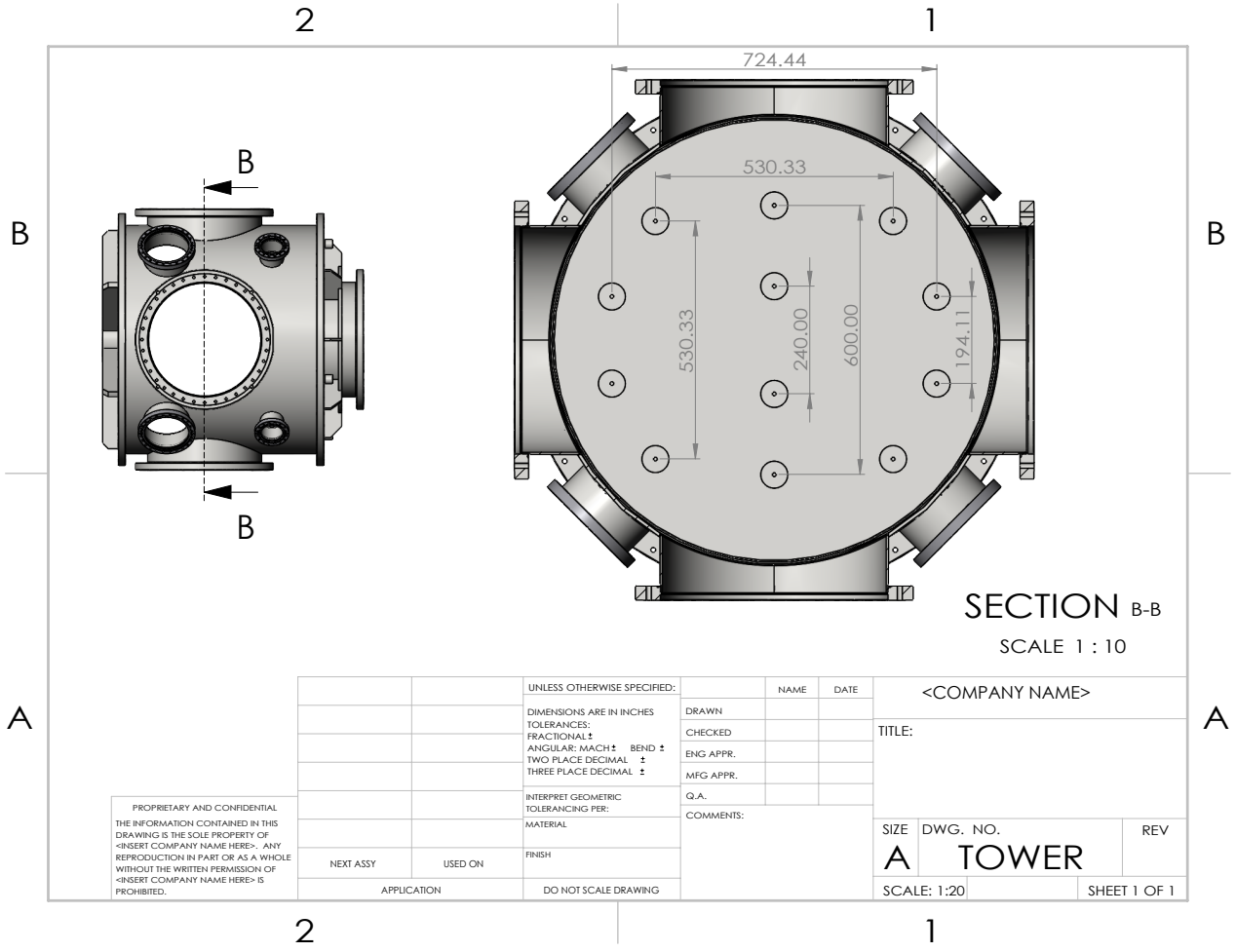

Figure C.7: Optical chamber of MIGA project

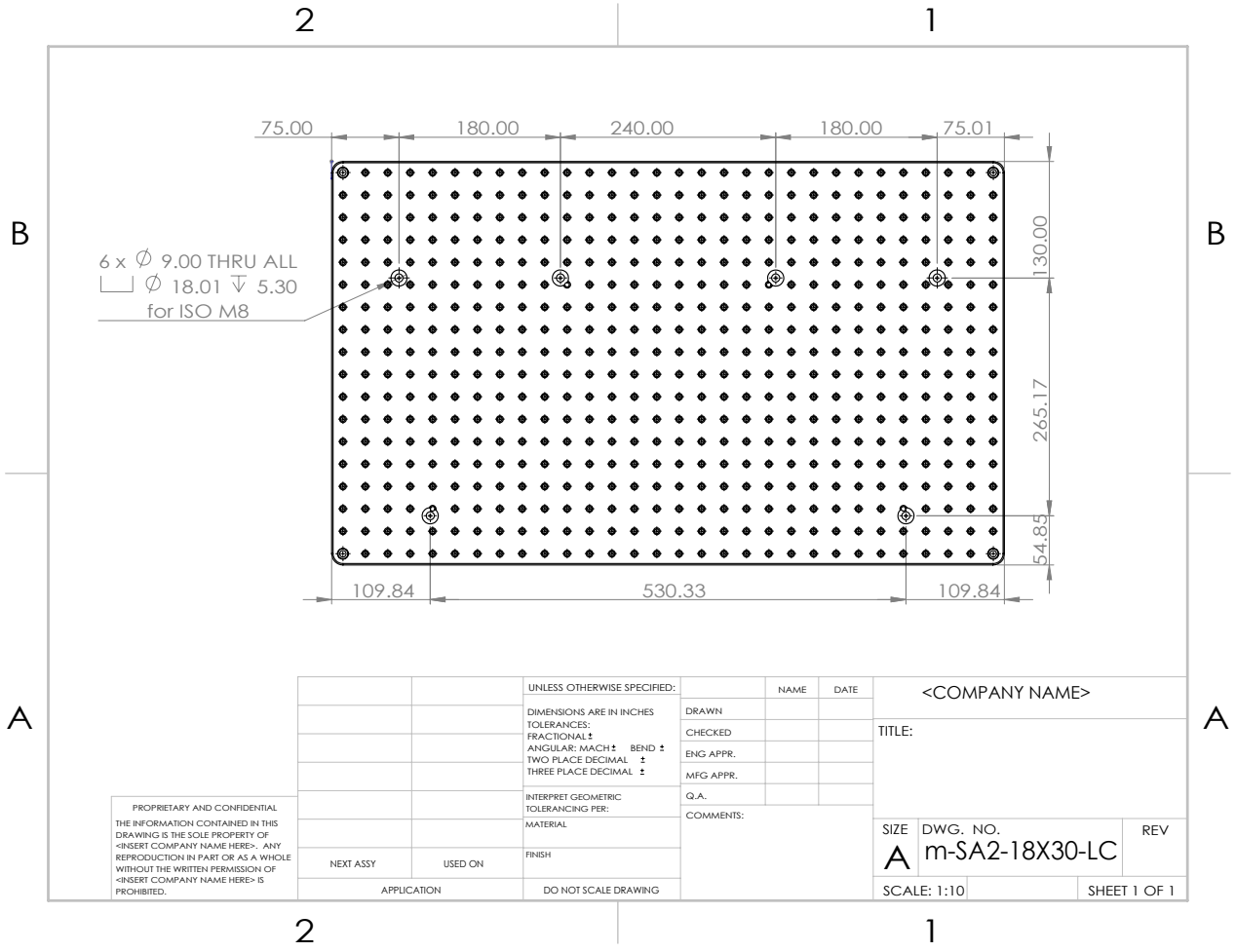

Figure C.8: Breadboard chamber of MIGA project

Appendix D

Scientific production

Peer reviewed articles

1. Benjamin Canuel, Sven Abend, Pau Amaro-Seoane, Francesca Badaracco, Quentin Beaufils, Andrea Bertoldi, Kai Bongs, Philippe Bouyer, Claus Braxmaier, Walid Chaibi, Nelson Christensen, Florian fitzek, Giorgos Flouris, Naceur Gaaloul, Stephane Gaffet, Carlos L. Garrido Alzar, Remi Geiger, Saida Guellati-Khelifa, Klemens Hammerer, Jan Harms, Jacques Hinderer, Michael Holynski, Joseph Junca, Stavros Katsanevas, Carsten Klempt, Christos Kozanitis, Markus Krutzik, Arnaud Landragin, Ignacio Làzaro Roche, Bastian Leykauf, Yu-Hung Lien, Sina Loriani, Sebastien Merlet, Mourad Merzougui, Miquel Nofrarias, Panagiotis Papadakos, Franck Pereira dos Santos, Achim Peters, Dimitris Plexousakis, Marco Prevedelli, Ernst M Rasel, Yves Rogister, Severine Rosat, Albert Roura, Dylan Sabulsky, Vladimir Schkolnik, Dennis Schlippert, Christian Schubert, Leonid Sidorenkov, Jan-Niclas Siemss, Carlos Sopuerta, Fiodor Sorrentino, Christian Struckmann, Guglielmo M Tino, Greg Tsagkatakis, Andrea Viceré, Wolf von Klitzing, Lisa Woerner, and Xinhao Zou. Elgar - a european laboratory for gravitation and atom-interferometric research. *Classical and Quantum Gravity*, 2020. URL http://iopscience.iop.org/10.1088/1361-6382/aba80e.

2. DO Sabulsky, J Junca, G Lefèvre, X Zou, A Bertoldi, B Battelier, M Prevedelli, G Stern, J Santoire, Q Beaufils, et al. A fibered laser system for the miga large scale atom inter-

ferometer. *Scientific reports*, 10(1):1–14, 2020.

3. Joseph Junca, Andrea Bertoldi, Dylan O Sabulsky, Grégoire Lefèvre, Xinhao Zou, J-B Decitre, Remi Geiger, Arnaud Landragin, Stéphane Gaffet, Philippe Bouyer, et al. Characterizing earth gravity field fluctuations with the miga antenna for future gravitational wave detectors. *Physical Review D*, 99(10):104026, 2019.

4. Yousef Abou El-Neaj et al. AEDGE: Atomic Experiment for Dark Matter and Gravity Exploration in Space. *EPJ Quantum Technology*, 7:6, 2020. URL https://doi.org/10.1140/epjqt/s40507-020-0080-0.

5. Andrea Bertoldi, C-H Feng, H Eneriz, M Carey, DS Naik, Joseph Junca, Xinhao Zou, Dylan O Sabulsky, Benjamin Canuel, Philippe Bouyer, et al. A control hardware based on a field programmable gate array for experiments in atomic physics. *Review of Scientific Instruments*, 91(3):033203, 2020.

Peer reviewed articles proceedings

1. D. O. Sabulsky, J. Junca, X. Zou, A. Bertoldi, M. Prevedelli, Q. Beaufils, R. Geiger, A. Landragin, P. Bouyer, and B. Canuel. Multi-photon atom interferometry via cavity-enhanced bragg diffraction, 2022. URL https://arxiv.org/abs/2201.11693.

Bibliography

[1] Albert Einstein. Über gravitationswellen. *Sitzungsberichte der Königlich Preußischen Akademie der Wissenschaften (Berlin)*, pages 154–167, 1918.

[2] Benjamin P Abbott, Richard Abbott, TD Abbott, MR Abernathy, Fausto Acernese, Kendall Ackley, Carl Adams, Thomas Adams, Paolo Addesso, RX Adhikari, et al. Observation of gravitational waves from a binary black hole merger. *Physical review letters*, 116(6):061102, 2016.

[3] B Canuel, A Bertoldi, L Amand, E Pozzo Di Borgo, T Chantrait, C Danquigny, M Dovale Álvarez, B Fang, A Freise, R Geiger, et al. Exploring gravity with the miga large scale atom interferometer. *Scientific reports*, 8(1):1–23, 2018.

[4] Isaac Newton. Isaac newton letter to robert hooke, 1675. *Simon Gratz collection. Digital Library. Retrieved from https://digitallibrary. hsp. org/index. php/Detail/objects/9792*, 2019.

[5] Peter R Saulson. *Fundamentals of interferometric gravitational wave detectors*. World Scientific, 1994.

[6] Richard F Gunstone and Richard T White. Understanding of gravity. *Science education*, 65(3):291–299, 1981.

[7] F. Acernese et al. Advanced Virgo: a second-generation interferometric gravitational wave detector. *Class. Quantum Grav.*, 32(2):024001, 2015. doi:10.1088/0264-9381/32/2/024001. URL https://doi.org/10.1088/0264-9381/32/2/024001.

[8] LIGO. Introduction to ligo & gravitational waves. [EB/OL]. https://www.ligo.org/science/GW-Inspiral.php Accessed April 4, 2022.

[9] Junaid Aasi, BP Abbott, Richard Abbott, Thomas Abbott, MR Abernathy, Kendall Ackley, Carl Adams, Thomas Adams, Paolo Addesso, RX Adhikari, et al. Advanced ligo. *Classical and quantum gravity*, 32(7):074001, 2015.

[10] F. Acernese et al. Calibration of Advanced Virgo and Reconstruction of the Gravitational Wave Signal $h(t)$ during the Observing Run O2. *Class. Quantum Grav.*, 35(20): 205004, 2018. doi:10.1088/1361-6382/aadf1a. URL https://doi.org/10.1088/1361-6382/aadf1a.

[11] Peter Lebedew. Untersuchungen über die druckkräfte des lichtes. *Annalen der Physik*, 311(11):433–458, 1901.

[12] Theodore H Maiman et al. Stimulated optical radiation in ruby. 1960.

[13] Steven Chu, Leo Hollberg, John E Bjorkholm, Alex Cable, and Arthur Ashkin. Three-dimensional viscous confinement and cooling of atoms by resonance radiation pressure. *Physical review letters*, 55(1):48, 1985.

[14] Mike H Anderson, Jason R Ensher, Michael R Matthews, Carl E Wieman, and Eric A Cornell. Observation of bose-einstein condensation in a dilute atomic vapor. *science*, 269(5221):198–201, 1995.

[15] Kendall B Davis, M-O Mewes, Michael R Andrews, Nicolaas J van Druten, Dallin S Durfee, DM Kurn, and Wolfgang Ketterle. Bose-einstein condensation in a gas of sodium atoms. *Physical review letters*, 75(22):3969, 1995.

[16] Kentaro Somiya. Detector configuration of kagra–the japanese cryogenic gravitational-wave detector. *Classical and Quantum Gravity*, 29(12):124007, 2012.

[17] CS Unnikrishnan. Indigo and ligo-india: scope and plans for gravitational wave research and precision metrology in india. *International Journal of Modern Physics D*, 22 (01):1341010, 2013.

[18] Michele Punturo, Harald Lück, and Mark Beker. A third generation gravitational wave observatory: the einstein telescope. In *Advanced interferometers and the search for gravitational waves*, pages 333–362. Springer, 2014.

[19] David Reitze, Rana X Adhikari, Stefan Ballmer, Barry Barish, Lisa Barsotti, GariLynn Billingsley, Duncan A Brown, Yanbei Chen, Dennis Coyne, Robert Eisenstein, et al. Cosmic explorer: the us contribution to gravitational-wave astronomy beyond ligo. *arXiv preprint arXiv:1907.04833*, 2019.

[20] Nicola Tamanini, Chiara Caprini, Enrico Barausse, Alberto Sesana, Antoine Klein, and Antoine Petiteau. Science with the space-based interferometer elisa. iii: Probing the expansion of the universe using gravitational wave standard sirens. *Journal of Cosmology and Astroparticle Physics*, 2016(04):002, 2016.

[21] Jun Luo, Li-Sheng Chen, Hui-Zong Duan, Yun-Gui Gong, Shoucun Hu, Jianghui Ji, Qi Liu, Jianwei Mei, Vadim Milyukov, Mikhail Sazhin, et al. Tianqin: a space-borne gravitational wave detector. *Classical and Quantum Gravity*, 33(3):035010, 2016.

[22] Wen-Hong Ruan, Zong-Kuan Guo, Rong-Gen Cai, and Yuan-Zhong Zhang. Taiji program: gravitational-wave sources. *International Journal of Modern Physics A*, 35(17): 2050075, 2020.

[23] Yousef Abou El-Neaj et al. AEDGE: Atomic Experiment for Dark Matter and Gravity Exploration in Space. *EPJ Quantum Technology*, 7:6, 2020. URL https://doi.org/10.1140/epjqt/s40507-020-0080-0.

[24] Seiji Kawamura, Masaki Ando, Naoki Seto, Shuichi Sato, Mitsuru Musha, Isao Kawano, Jun'ichi Yokoyama, Takahiro Tanaka, Kunihito Ioka, Tomotada Akutsu, et al. Current status of space gravitational wave antenna decigo and b-decigo. *Progress of Theoretical and Experimental Physics*, 2021(5):05A105, 2021.

[25] Christopher J Moore, Robert H Cole, and Christopher PL Berry. Gravitational-wave sensitivity curves. *Classical and Quantum Gravity*, 32(1):015014, 2014.

[26] Robert Cole Christopher Moore and Christopher Berry. Gwplotter. [EB/OL]. http://gwplotter.com/ Accessed December 24, 2021.

[27] Benjamin Canuel, Sven Abend, Pau Amaro-Seoane, Francesca Badaracco, Quentin Beaufils, Andrea Bertoldi, Kai Bongs, Philippe Bouyer, Claus Braxmaier, Walid Chaibi, Nelson Christensen, Florian fitzek, Giorgos Flouris, Naceur Gaaloul, Stephane Gaffet, Carlos L. Garrido Alzar, Remi Geiger, Saida Guellati-Khelifa, Klemens Hammerer, Jan Harms, Jacques Hinderer, Michael Holynski, Joseph Junca, Stavros Katsanevas, Carsten Klempt, Christos Kozanitis, Markus Krutzik, Arnaud Landragin, Ignacio Làzaro Roche, Bastian Leykauf, Yu-Hung Lien, Sina Loriani, Sebastien Merlet, Mourad Merzougui, Miquel Nofrarias, Panagiotis Papadakos, Franck Pereira dos Santos, Achim Peters, Dimitris Plexousakis, Marco Prevedelli, Ernst M Rasel, Yves Rogister, Severine Rosat, Albert Roura, Dylan Sabulsky, Vladimir Schkolnik, Dennis Schlippert, Christian Schubert, Leonid Sidorenkov, Jan-Niclas Siemss, Carlos Sopuerta, Fiodor Sorrentino, Christian Struckmann, Guglielmo M Tino, Greg Tsagkatakis, Andrea Viceré, Wolf von Klitzing, Lisa Woerner, and Xinhao Zou. Elgar - a european laboratory for gravitation and atom-interferometric research. *Classical and Quantum Gravity*, 2020. URL http://iopscience.iop.org/10.1088/1361-6382/aba80e.

[28] DO Sabulsky, Joseph Junca, Xinhao Zou, Andrea Bertoldi, Marco Prevedelli, Q Beaufils, R Geiger, A Landragin, P Bouyer, and B Canuel. Multi-photon atom interferometry via cavity-enhanced bragg diffraction. *arXiv preprint arXiv:2201.11693*, 2022.

[29] B Canuel, X Zou, DO Sabulsky, J Junca, A Bertoldi, Q Beaufils, R Geiger, A Landragin, M Prevedelli, S Gaffet, et al. A gravity antenna based on quantum technologies: Miga. *arXiv preprint arXiv:2204.12137*, 2022.

[30] Stéphane Gaffet, Yves Guglielmi, Jean Virieux, Georges Waysand, Andreas Chwala, Ronny Stolz, Christophe Emblanch, Michel Auguste, Daniel Boyer, and Alain Cavaillou. Simultaneous seismic and magnetic measurements in the low-noise underground laboratory (lsbb) of rustrel, france, during the 2001 january 26 indian earthquake. *Geophysical Journal International*, 155(3):981–990, 2003.

[31] Joseph Junca, Andrea Bertoldi, Dylan O Sabulsky, Grégoire Lefèvre, Xinhao Zou, J-B Decitre, Remi Geiger, Arnaud Landragin, Stéphane Gaffet, Philippe Bouyer, et al. Characterizing earth gravity field fluctuations with the miga antenna for future gravitational wave detectors. *Physical Review D*, 99(10):104026, 2019.

[32] G. Sénéchal, H. Zeyen, C. Emblanch, Konstantinos CHALIKAKIS, Simon Damien CARRIERE, and Charles Danquigny. Geophysical investigations at the LSBB. In *E3S Web of Conferences - 5th I-DUST conference*, volume 4, APT, France, 2014. LSBB Laboratoire souterrain à bas bruit. doi:10.1051/e3sconf/20140404001. URL https://hal.archives-ouvertes.fr/hal-01816796. ACT.

[33] Parameswaran Hariharan. *Basics of interferometry*. Elsevier, 2010.

[34] Alex Abramovici, William E Althouse, Ronald WP Drever, Yekta Gürsel, Seiji Kawamura, Frederick J Raab, David Shoemaker, Lisa Sievers, Robert E Spero, Kip S Thorne, et al. Ligo: The laser interferometer gravitational-wave observatory. *science*, 256 (5055):325–333, 1992.

[35] G M Harry et al. *Class. Quantum Grav.*, 27:084006, 2010.

[36] B Caron, A Dominjon, C Drezen, R Flaminio, X Grave, F Marion, L Massonnet, C Mehmel, R Morand, B Mours, et al. The virgo interferometer. *Classical and Quantum Gravity*, 14(6):1461, 1997.

[37] Virgo Collaboration et al. The virgo physics book, vol. ii, optics and related topics, 2005.

[38] Albert Abraham Michelson. The relative motion of the earth and of the luminiferous ether. *American Journal of Science*, s3-22:120 – 129.

[39] Robert S Shankland. Michelson-morley experiment. *American Journal of Physics*, 32 (1):16–35, 1964.

[40] Albert Einstein. Ether and the theory of relativity. In *The genesis of general relativity*, pages 1537–1542. Springer, 2007.

[41] Aashish A Clerk. Quantum noise and quantum measurement. *APS Tutorial on Quantum Measurement),” McGill University website, http://www. physics. mcgill. ca/˜ clerk/PDFfiles/APSQMeasTutorialMar08. pdf*, 2008.

[42] CWJ Beenakker and Christian Schonenberger. Quantum shot noise. *arXiv preprint cond-mat/0605025*, 2006.

[43] Robinjeet Singh. Quantum radiation pressure noise: Exposing the quantum mechanics of optomechanical interactions. 2016.

[44] Katherine L Dooley, Lisa Barsotti, Rana X Adhikari, Matthew Evans, Tobin T Fricke, Peter Fritschel, Valera Frolov, Keita Kawabe, and Nicolás Smith-Lefebvre. Angular control of optical cavities in a radiation-pressure-dominated regime: the enhanced ligo case. *JOSA A*, 30(12):2618–2626, 2013.

[45] L McCuller, C Whittle, D Ganapathy, K Komori, M Tse, A Fernandez-Galiana, L Barsotti, P Fritschel, M MacInnis, F Matichard, et al. Frequency-dependent squeezing for advanced ligo. *Physical review letters*, 124(17):171102, 2020.

[46] Alain Miffre, Marion Jacquey, Matthias Büchner, Gérard Trénec, and Jacques Vigué. Atom interferometry. *Physica Scripta*, 74(2):C15, 2006.

[47] Immanuel Estermann and Otto Stern. Beugung von molekularstrahlen. *Zeitschrift für Physik*, 61(1):95–125, 1930.

[48] Olivier Carnal and Jürgen Mlynek. Young’s double-slit experiment with atoms: A simple atom interferometer. *Physical review letters*, 66(21):2689, 1991.

[49] Alexander D Cronin, Jörg Schmiedmayer, and David E Pritchard. Atom interferometers. *arXiv preprint arXiv:0712.3703*, 2007.

[50] M Kasevich and S Chu. Measurement of the gravitational acceleration of an atom with a light-pulse atom interferometer. *Applied Physics B*, 54(5):321–332, 1992.

[51] S Bernet, R Abfalterer, C Keller, MK Oberthaler, J Schmiedmayer, and A Zeilinger. Matter waves in time-modulated complex light potentials. *Physical Review A*, 62(2): 023606, 2000.

[52] H Müller, S-W Chiow, Q Long, S Herrmann, and S Chu. Atom interferometry with up to 24-photon-momentum-transfer beam splitters. *Phys. Rev. Lett.*, 100(18):180405, 2008. URL https://doi.org/10.1103/PhysRevLett.100.180405.

[53] C Keller, J Schmiedmayer, A Zeilinger, T Nonn, S Dürr, and G Rempe. Adiabatic following in standing-wave diffraction of atoms. *Applied Physics B*, 69(4):303–309, 1999.

[54] Holger Müller, Sheng-wey Chiow, and Steven Chu. Atom-wave diffraction between the raman-nath and the bragg regime: Effective rabi frequency, losses, and phase shifts. *Physical review A*, 77(2):023609, 2008.

[55] Ashley Béguin, Tangui Rodzinka, Jacques Vigué, Baptiste Allard, and Alexandre Gauguet. Characterization of an atom interferometer in the quasi-bragg regime. *Physical Review A*, 105(3):033302, 2022.

[56] Patrick Cheinet, Benjamin Canuel, Franck Pereira Dos Santos, Alexandre Gauguet, Florence Yver-Leduc, and Arnaud Landragin. Measurement of the sensitivity function in a time-domain atomic interferometer. *IEEE Transactions on instrumentation and measurement*, 57(6):1141–1148, 2008.

[57] Peter J Martin, Bruce G Oldaker, Andrew H Miklich, and David E Pritchard. Bragg scattering of atoms from a standing light wave. *Physical review letters*, 60(6):515, 1988.

[58] Benjamin Canuel. *Étude d'un gyromètre à atomes froids*. PhD thesis, Université Paris Sud-Paris XI, 2007.

[59] Kathryn Moler, David S Weiss, Mark Kasevich, and Steven Chu. Theoretical analysis of velocity-selective raman transitions. *Physical Review A*, 45(1):342, 1992.

[60] B. Canuel, A. Bertoldi, L. Amand, E. Pozzo di Borgo, T. Chantrait, C. Danquigny, M. Dovale Álvarez, B. Fang, A. Freise, R. Geiger, J. Gillot, S. Henry, J. Hinderer, D. Holleville, J. Junca, G. Lefèvre, M. Merzougui, N. Mielec, T. Monfret, S. Pelisson, M. Prevedelli, S. Reynaud, I. Riou, Y. Rogister, S. Rosat, E. Cormier, A. Landragin, W. Chaibi, S. Gaffet, and P. Bouyer. Exploring gravity with the MIGA large scale atom interferometer. *Sci. Rep.*, 8(1):14064, sep 2018. doi:10.1038/s41598-018-32165-z. URL https://doi.org/10.1038/s41598-018-32165-z.

[61] CWJ Beenakker and Christian Schönenberger. Quantum shot noise. 2003.

[62] Rolf Landauer. The noise is the signal. *Nature*, 392(6677):658–659, 1998.

[63] G Losurdo, M Bernardini, S Braccini, C Bradaschia, C Casciano, V Dattilo, R De Salvo, A Di Virgilio, F Frasconi, A Gaddi, et al. An inverted pendulum preisolator stage for the virgo suspension system. *Review of scientific instruments*, 70(5):2507–2515, 1999.

[64] Walid Chaibi, Remi Geiger, Benjamin Canuel, Andrea Bertoldi, Arnaud Landragin, and Philippe Bouyer. Low frequency gravitational wave detection with ground-based atom interferometer arrays. *Physical Review D*, 93(2):021101, 2016.

[65] B. Canuel, S. Abend, P. Amaro-Seoane, F. Badaracco, Q. Beaufils, A. Bertoldi, K. Bongs, P. Bouyer, C. Braxmaier, W. Chaibi, N. Christensen, F. Fitzek, G. Flouris, N. Gaaloul, S. Gaffet, C. L. Garrido Alzar, R. Geiger, S. Guellati-Khelifa, K. Hammerer, J. Harms, J. Hinderer, M. Holynski, J. Junca, S. Katsanevas, C. Klempt, C. Kozanitis, M. Krutzik, A. Landragin, I. Làzaro Roche, B. Leykauf, Y. H. Lien, S. Loriani, S. Merlet, M. Merzougui, M. Nofrarias, P. Papadakos, F. Pereira dos Santos, A. Peters, D. Plexousakis, M. Prevedelli, E. M. Rasel, Y. Rogister, S. Rosat, A. Roura, D. O. Sabulsky, V. Schkolnik, D. Schlippert, C. Schubert, L. Sidorenkov, J. N. Siemß, C. F. Sopuerta, F. Sorrentino, C. Struckmann, G. M. Tino, G. Tsagkatakis, A. Viceré, W. von Klitzing, L. Woerner, and X. Zou. Technologies for the ELGAR large scale atom interferometer array, 2020.

[66] Dylan O. Sabulsky Joseph Junca Andrea Bertholdi Quentin Beaufils, Xinhao Zou et al. Cold-atom sources for the matter-wave laser interferometric gravitation antenna (miga). 2022.

[67] Muquans. Muquans- precision quantum sensors, 2011. URL muquans.com.

[68] Andrea Bertoldi, C-H Feng, H Eneriz, M Carey, DS Naik, Joseph Junca, Xinhao Zou, Dylan O Sabulsky, Benjamin Canuel, Philippe Bouyer, et al. A control hardware based on a field programmable gate array for experiments in atomic physics. *Review of Scientific Instruments*, 91(3):033203, 2020.

[69] DO Sabulsky, J Junca, G Lefèvre, X Zou, A Bertoldi, B Battelier, M Prevedelli, G Stern, J Santoire, Q Beaufils, et al. A fibered laser system for the miga large scale atom interferometer. *Scientific reports*, 10(1):1–14, 2020.

[70] John R Levine, John Mason, John R Levine, Tony Mason, Doug Brown, John R Levine, and Paul Levine. *Lex & yacc*. " O'Reilly Media, Inc.", 1992.

[71] Inc. Free Software Foundation. Bison 3.8.1. URL https://www.gnu.org/software/bison/manual/bison.html.

[72] Red Pitaya d.o.o. Redpitaya docs. URL https://redpitaya.readthedocs.io/en/latest/#.

[73] Frederick J Raab. Overview of ligo instrumentation. In *Gravitational Wave and Particle Astrophysics Detectors*, volume 5500, pages 11–24. International Society for Optics and Photonics, 2004.

[74] Michael E Zucker and Stanley E Whitcomb. Measurement of optical path fluctuations due to residual gas in the ligo 40 meter interferometer. In *Proceedings of the Seventh Marcel Grossman Meeting on recent developments in theoretical and experimental general relativity, gravitation, and relativistic field theories*, pages 1434–1436, 1996.

[75] R Dolesi, M Hueller, D Nicolodi, D Tombolato, S Vitale, PJ Wass, WJ Weber, M Evans, P Fritschel, R Weiss, et al. Brownian force noise from molecular collisions and the sensitivity of advanced gravitational wave observatories. *Physical Review D*, 84(6): 063007, 2011.

[76] Pfeiffer Vacuum GmbH. *The vacuum technology book*. Pfeiffer Vacuum GmbH, 2013.

[77] Peter Brimblecombe. *Air composition and chemistry*. Cambridge University Press, 1996.

[78] KARL Jousten. Ultrahigh vacuum gauges. *CERN Accelerator School Vacuum in accelerators*, page 145, 2007.

[79] standford research system. Residual gas analyzer. URL https://www.thinksrs.com/products/rga.html.

[80] Agilent. Turbo-v 1001 navigator pump. URL https://www.agilent.com/en/product/vacuum-technologies/turbo-pumps-controllers/turbo-pumps/turbo-v-1001-navigator-pump.

[81] SAES advanced technologies S.p.A.-Italy. Operating instructions–nextorr d 100-5 pump. 2013.

[82] BT Hogan and OB Malyshev. Evaluation test of nextorr® d 100-5 pump. *Cockcroft Institute Report-Cockcroft-13-47, STFC Daresbury Laboratory, Warrington, UK*, 2013.

[83] Z Siwy and A Fuliński. Fabrication of a synthetic nanopore ion pump. *Physical Review Letters*, 89(19):198103, 2002.

[84] MATSUSADA PRECISION Inc. Ion pumps. URL https://www.matsusada.com/application/ps/ion_pumps/.

[85] Hao Feng, Chenyang Zhao, Yani Xie, Wenlian Wang, Xia Zhang, and Zhijie Zhang. Research on dynamic calibration and dynamic compensation of k-type thermocouple. In *2014 IEEE International Instrumentation and Measurement Technology Conference (I2MTC) Proceedings*, pages 267–271. IEEE, 2014.

[86] Kirsten Zapfe. Leak detection. Technical report, Dt. Elektronen-Synchrotron DESY, 2007.

[87] Isabelle Riou, Nicolas Mielec, Grégoire Lefèvre, Marco Prevedelli, Arnaud Landragin, Philippe Bouyer, Andrea Bertoldi, Remi Geiger, and Benjamin Canuel. A marginally stable optical resonator for enhanced atom interferometry. *Journal of Physics B: Atomic, Molecular and Optical Physics*, 50(15):155002, 2017.

[88] Amnon Yariv. *Quantum electronics*. John Wiley & Sons, 1989.

[89] B Canuel, L Amand, Andrea Bertoldi, W Chaibi, R Geiger, J Gillot, A Landragin, M Merzougui, I Riou, SP Schmid, et al. The matter-wave laser interferometer gravitation antenna (miga): New perspectives for fundamental physics and geosciences. In *E3S Web of Conferences*, volume 4, page 01004. EDP Sciences, 2014.

[90] Isabelle Riou. *Vers la détection d'ondes gravitationnelles par interférométrie atomique en cavité: nouvelles géométries optiques et premier dispositif*. PhD thesis, Bordeaux, 2017.

[91] P Della Porta, C Emil, and SJ Hellier. Alkali metal generation and gas evolution from alkali metal dispensers. In *IEEE Conference on Tube Techniques, New York*, 1968.

[92] SAES Getters S.p.A. Alkali metals dispensers. URL https://www.saesgetters.com/products-functions/products/dispensers/alkali-metals-dispensers.

[93] P Cheinet. *Conception et réalisation d'un gravimètre à atomes froids*. PhD thesis, Universiteé Paris, 2006. URL https://tel.archives-ouvertes.fr/tel-00070861v1.

[94] Jean Dalibard and Claude Cohen-Tannoudji. Laser cooling below the doppler limit by polarization gradients: simple theoretical models. *JOSA B*, 6(11):2023–2045, 1989.

[95] P Jeffery Ungar, David S Weiss, Erling Riis, and Steven Chu. Optical molasses and multilevel atoms: theory. *JOSA B*, 6(11):2058–2071, 1989.

[96] David S Weiss, Erling Riis, Yaakov Shevy, P Jeffrey Ungar, and Steven Chu. Optical molasses and multilevel atoms: experiment. *JOSA B*, 6(11):2072–2083, 1989.

[97] C Salomon, J Dalibard, A Aspect, H Metcalf, and C Cohen-Tannoudji. Channeling atoms in a laser standing wave. *Physical review letters*, 59(15):1659, 1987.

[98] B Sheehy, SQ Shang, P Van Der Straten, S Hatamian, and H Metcalf. Magnetic-field-induced laser cooling below the doppler limit. *Physical review letters*, 64(8):858, 1990.

[99] B Sheehy, Song-Quan Shang, R Watts, S Hatamian, and H Metcalf. Diode-laser deceleration and collimation of a rubidium beam. *JOSA B*, 6(11):2165–2170, 1989.

[100] Hamamatsu Photonics K.K. and its affiliates. Si pin photodiode array, s5870. URL https://www.hamamatsu.com/eu/en/product/optical-sensors/photodiodes/si-photodiode-array/segmented-type-si-photodiode/S5870.html.

[101] Indranil Dutta. *Stability improvement of a Sagnac cold atom interferometer: towards continuous operation*. PhD thesis, Paris 6, 2015.

[102] Remi Geiger. *Atom interferometry: from fundamental physics to precision inertial measurements*. PhD thesis, Sorbonne Université, 2019.

[103] Alexandre Gauguet, TE Mehlstäubler, Thomas Lévèque, J Le Gouët, W Chaibi, B Canuel, Andre Clairon, F Pereira Dos Santos, and Arnaud Landragin. Off-resonant raman transition impact in an atom interferometer. *Physical Review A*, 78(4):043615, 2008.

[104] M Kasevich and S Chu. Atomic interferometry using stimulated raman transitions. *Phys. Rev. Lett.*, 67(2):181, 1991. URL https://doi.org/10.1103/PhysRevLett.67.181.

[105] Magnetic-Declination.com. Magneticdeclination. URL https://www.magnetic-declination.com/.

[106] Malte Schmidt, A Senger, M Hauth, C Freier, V Schkolnik, and Achim Peters. A mobile high-precision absolute gravimeter based on atom interferometry. *Gyroscopy and Navigation*, 2(3):170–177, 2011.

[107] Gabriele Rosi. Precision gravity measurements with atom interferometry. *PhD. University of Pisa*, 2012.

[108] D. O. Sabulsky, J. Junca, X. Zou, A. Bertoldi, M. Prevedelli, Q. Beaufils, R. Geiger, A. Landragin, P. Bouyer, and B. Canuel. Multi-photon atom interferometry via cavity-enhanced bragg diffraction, 2022. URL https://arxiv.org/abs/2201.11693.